

令和6年度 修士論文

Theoretical study of the one-dimensional
extended Hubbard model coupled with an
optical cavity

(光共振器と結合した1次元拡張ハーバード模型に関する理論的研究)

東京大学大学院理学系研究科物理学専攻
中本大河
(指導教員: 辻直人)

Abstract

In recent years, nonequilibrium control of quantum material properties with classical laser pulses has become a major subject of study in condensed matter physics. However, there is another way to control materials by exploiting the vacuum fluctuation of light, known as cavity quantum electrodynamics (cavity QED). If quantum materials are confined in an optical cavity and are strongly coupled with the vacuum fluctuation of light, there emerges a new path to control the quantum material properties through vacuum fluctuations.

In this thesis, we focused on a strongly correlated system, a one-dimensional extended Hubbard model (1DEHM). We theoretically study the 1DEHM coupled with an optical cavity as a prototype of strongly correlated materials in the optical cavity. This thesis mainly examines virtual photons in the ground state and vacuum Rabi splitting in the excited state. In order to numerically investigate the ground state and excited state, we use the density matrix renormalization group (DMRG) method and the time-evolving block decimation (TEBD) method, respectively.

In the ground state, we numerically calculate how the on-site Coulomb interaction U and nearest-neighbor Coulomb interaction V are reflected in virtual photons. We find that the photon number is suppressed when $V = U/2$ is satisfied in the small coupling constant, whereas the photon number is enhanced when $V = U/2$ is satisfied in the large coupling constant. In order to analytically understand the different behaviors, we perform the perturbation and squeezed transformation analyses. These analyses show that the current fluctuation and the absolute value of the kinetic energy are essential factors in determining the photon number.

In the excited state, we numerically simulate the vacuum Rabi splitting by calculating the optical conductivity and the photon spectral function. The Rabi splitting can be seen in both quantities due to the hybrid nature of the cavity polariton. However, the photon spectral function for $V = 0$ does not show the Rabi splitting but rather a spectral broadening. We give an analytical explanation of the Rabi splitting and the spectral broadening.

Acknowledgment

I would like to express my great gratitude to all the people who have helped me through my master's course.

First, I sincerely thank my supervisor, Naoto Tsuji, for his comments, remarks, and suggestions throughout my master's course. These two years in his group have been very fruitful in improving my research skills. I also thank him for his patience to read my manuscript.

I appreciate all the current and former members of the Tsuji group, including Prof. Kazuaki Takasan, Prof. Shohei Imai, Huanyu Zhang, Hiromu Ushihara, Shunsuke Nishimura, Titouan Mouilleron, Raigo Nagashima, Shuta Matsuura, Gerrit Niederhoff. Ordinary discussions with them and their questions and comments on my group seminar presentations have been helpful for me to carry out the study. In particular, I would like to thank Prof. Kazuaki Takasan for guiding me through various stages of my research life.

I am grateful to Jun Mochida and Kanta Masuki of the Ashida group at the University of Tokyo for discussing cavity physics. I am also grateful to Ryota Ueda of the Kuroki group at Osaka University for telling me about the numerical methods.

I also express my gratitude to Prof. Hosho Katsura and Prof. Ryusuke Matsunaga. They have given helpful comments on my manuscript and presentation as members of my master's thesis defense committee.

I acknowledge the financial support and educational programs of World-leading Innovative Graduate Study Program, Materials Education program for the future leaders in Research, Industry, and Technology (WINGS-MERIT), the University Tokyo.

Finally, I would like to thank my parents and my fiancée for their support in both the practical and emotional aspects of my life.

Contents

1	Introduction	1
1.1	Cavity QED	1
1.1.1	Various coupling regime	2
1.1.2	Collective coupling	3
1.2	Cavity polariton	4
1.2.1	Vacuum Rabi splitting	4
1.2.2	Virtual photons	5
1.3	Cavity quantum material	6
1.3.1	One-dimensional extended Hubbard model	7
1.4	Purpose of the thesis	9
1.5	Outline of the thesis	9
2	Model and Numerical Methods	10
2.1	One-dimensional extended Hubbard model coupled with an optical cavity	10
2.1.1	Derivation of the model	11
2.1.2	Non-interacting tight-binding model coupled with an optical cavity	15
2.2	Matrix Product state	17
2.2.1	Mathematical formulation for the MPS	17
2.2.2	Construction of MPS	21
2.2.3	Left and right canonical conditions	23
2.3	Density matrix renormalization group method	24
2.3.1	Matrix Product Operator	25
2.3.2	Variational ground state search	26
2.3.3	DMRG method for the cavity-matter systems	29
2.4	Time Evolving Block Decimation method	30
2.4.1	Suzuki-Trotter decomposition	30
2.4.2	Updating MPS after the action of local operators	31
2.4.3	TEBD method for cavity-matter systems	32
2.4.4	Error sources	34
3	Ground-State Properties	36
3.1	Ground-state calculation	36
3.2	Virtual photons	37
3.2.1	Perturbation analysis	37
3.2.2	Squeezed transformation analysis	40

3.3	Squeezing of photons	44
3.3.1	Wigner function	46
3.3.2	Probability distribution	46
4	Excited-State Properties	49
4.1	Excited-state calculation	49
4.2	Optical conductivity and photon spectral function	51
4.2.1	Vacuum Rabi splitting	51
4.2.2	Spectral broadening	53
5	Conclusion and Outlook	56
5.1	Summary	56
5.2	Future directions	56
5.2.1	Magnetic coupling	56
5.2.2	Exciton polariton condensate	57
5.2.3	Superradiant phase transition	57
A	Numerical Convergence	58

Chapter 1

Introduction

In recent years, the control of material properties with classical laser pulses has been investigated on both the experimental and theoretical sides. However, there is another way to control materials by exploiting quantumness of light, a field known as cavity quantum electrodynamics (cavity QED). In this chapter, we review the background of our study. In the first section, we overview the cavity QED and ultrastrong coupling of light and matter. The second section is devoted to sketching the physics of cavity polaritons, a universal concept in cavity QED. We emphasize that the formation of polaritons may change the ground state and excited states of matter and light. In the third section, we show the application of cavity QED to quantum materials (cavity quantum materials). The aim of our study and the outline of this thesis are presented in the last part of this chapter.

1.1 Cavity QED

Purcell has discovered in 1946 [1] that the strength of the interaction between an emitter and light can be enhanced or suppressed by engineering its electromagnetic environment. The discovery opened the whole field of research, today called cavity quantum electrodynamics (cavity QED).

Cavity QED is a field of quantum physics that studies the interaction between light and matter, typically atoms or quantum emitters, confined within a highly reflective optical or microwave cavity (Fig. 1.1). This setup allows researchers to probe and manipulate quantum electromagnetic phenomena at a fundamental level since one can control the electromagnetic environment inside the cavity by changing the spacing between two mirrors or their reflectivity.

The coupling of light and matter in a cavity has several differences from that in a free space. First, the energy of light confined in an optical cavity is quantized to be integer multiples of the cavity frequency $\Omega = c\pi/L$, where L is the spacing of the cavity. This quantized light is called cavity photons. If the length L is sufficiently small such that the cavity frequency Ω is comparable to the energy scale of the matter of interest, the lowest-frequency mode becomes dominant in low-energy physics. Therefore, the coupling between matter and photons with a single frequency Ω has been considered in the cavity

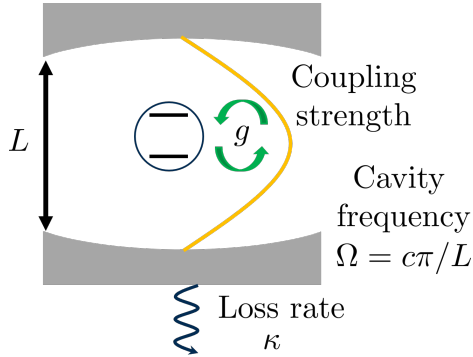


Figure 1.1: A basic setup of a cavity QED (Fabry-Perot type cavity). Cavity photons at frequency Ω couple with the matter at the strength g . Photons dissipate from the cavity at the rate κ .

QED setup. Second, the fundamental system parameters, such as the coupling strength g or the loss rate of the light κ , are determined depending on the cavity's geometry and matter in the cavity. When light is confined in a tiny space, the coupling strength is enhanced as $g \propto \frac{1}{\sqrt{V}}$, where V is the volume of the confined area. The loss rate of light κ is suppressed by increasing the reflectivity of the mirrors. In this way, the cavity frequency Ω , the coupling strength g , and the loss rate κ can be controlled in the cavity QED, and the system is traditionally classified based on the coupling strength.

1.1.1 Various coupling regime

The interaction between photons and emitters in the cavity is characterized by the cavity frequency Ω , the coupling strength g , and the loss rate κ . Their relative magnitudes distinguish the regimes of the interaction strength.

The regime of $g \ll \kappa$, dominated by the loss, is referred to as the weak coupling regime. In this regime, the spontaneous emission rate, which had been once thought to be an intrinsic property of the matter, can be modified by the cavity [2]. In contrast, when the cavity-emitter coupling dominates the loss rate, i.e., $g > \kappa$, the system enters the strong coupling regime. In this regime, photons and emitters remain coupled for a sufficiently long time before photons are lost from the cavity. This long lifetime of photons induces the hybridization of photon and matter states, and leads to the formation of new quantum states known as polaritons. As the coupling strength further increases to $g/\Omega \sim \mathcal{O}(0.1)$ ($\mathcal{O}(1)$), the system enters the ultrastrong coupling (deep ultrastrong coupling) regime [3, 4]. In this regime, many standard approximation methods used in weak and strong coupling regimes break down.

In order to achieve this (deep) ultrastrong coupling regime, various physical systems are utilized as cavities and emitters. For example, there are various types of cavities, such as Fabry-Perot cavities [5], split-ring resonator cavities [6], plasmonic cavities [7], array defect cavities [8], and semiconductor heterostructure cavities [9]. Similarly, various matter excitations are used as emitters, such as superconducting circuits [10], intersubband transitions [11], Landau levels [12], excitons [13] and magnons [14].

1.1.2 Collective coupling

The realization of the ultrastrong and deep ultrastrong coupling in several setups is rooted in the fact that the coupling strength is proportional to the square root of the number of emitters N . This coupling strength is called the collective coupling strength. The collective increase of the coupling strength occurs because multiple emitters are coupled to a common electromagnetic field.

In order to understand the collective coupling strength, the basic models of the cavity QED are reviewed here: One is the Rabi model [15], and another one is the Dicke model [16]. The Rabi model is a simple model that characterizes the interaction between light and matter through the absorption and emission of light. The matter in the Rabi model is regarded as a two-level system. The Dicke model is the N emitters version of the Rabi model. The Hamiltonians (we set $\hbar = 1$) which describes these models are,

$$\hat{H}_{\text{Rabi}} = \Omega_c \hat{a}^\dagger \hat{a} + \frac{\Omega_0}{2} \hat{\sigma}^z + g(\hat{a}^\dagger + \hat{a})(\hat{\sigma}^+ + \hat{\sigma}^-), \quad (1.1)$$

$$\hat{H}_{\text{Dicke}} = \Omega_c \hat{a}^\dagger \hat{a} + \frac{\Omega_0}{2} \sum_{i=1}^N \hat{\sigma}_i^z + g(\hat{a}^\dagger + \hat{a}) \sum_{i=1}^N (\hat{\sigma}_i^+ + \hat{\sigma}_i^-). \quad (1.2)$$

Here, \hat{a}^\dagger (\hat{a}) is the creation (annihilation) operator of photons, which satisfies the commutation relation $[\hat{a}, \hat{a}^\dagger] = 1$, $\hat{\sigma}^- = |g\rangle \langle e|$ and $\hat{\sigma}^+ = |e\rangle \langle g|$ are the lowering and rasing operators between the ground state $|g\rangle$ and the excited state $|e\rangle$ of a given two-level system, and $\hat{\sigma}^z = |e\rangle \langle e| - |g\rangle \langle g|$ is the Pauli operator in z -direction. The first and second terms represent the photon energy of quanta Ω_c and the emitter energy with the energy difference Ω_0 , respectively. The third term is the linear coupling term between the photons and the emitter. In the Dicke model, the N two-level systems are represented by $\hat{\sigma}_i$, where i is the label for each emitter. If we focus on the low-energy physics of the system, the Dicke model is simplified by introducing total spin operators $\hat{S}^\alpha = \sum_{i=1}^N \frac{1}{2} \hat{\sigma}_i^\alpha$ and using Holstein-Primakoff transformation. The transformation maps the total spin operators S^α to a bosonic mode \hat{b} ,

$$\hat{S}^z = -\frac{N}{2} + \hat{b}^\dagger \hat{b}, \quad (1.3)$$

$$\hat{S}^x = \frac{\hat{b}^\dagger + \hat{b}}{2} \sqrt{N - \hat{b}^\dagger \hat{b}}, \quad (1.4)$$

where \hat{b}^\dagger (\hat{b}) is the creation (annihilation) operator of collective excitation of matters, which satisfies the commutation relation $[\hat{b}, \hat{b}^\dagger] = 1$. If there is no macroscopic excitation (i.e., $N \gg \langle \hat{b}^\dagger \hat{b} \rangle$), Eq. (1.4) simplifies to $\hat{S}^x \rightarrow \frac{\sqrt{N}}{2} (\hat{b}^\dagger + \hat{b})$. In this situation, the Dicke model is transformed as

$$\begin{aligned} \hat{H}_{\text{Dicke}} &= \Omega_c \hat{a}^\dagger \hat{a} + \Omega_0 \hat{S}^z + 2g(\hat{a}^\dagger + \hat{a}) \hat{S}^x \\ &\simeq \Omega_c \hat{a}^\dagger \hat{a} + \Omega_0 \left(\hat{b}^\dagger \hat{b} - \frac{N}{2} \right) + \sqrt{N} g(\hat{a}^\dagger + \hat{a})(\hat{b}^\dagger + \hat{b}) =: \hat{H}_{\text{Hopfield}}. \end{aligned} \quad (1.5)$$

The final form of the Hamiltonian is often called the Hopfield Hamiltonian [17].

The Hopfield model Eq. (1.5) and the Rabi model Eq. (1.1) have the same form, except for the way to represent the matter excitation. In the Rabi model, the excitation of matter is described in terms of spins as excitations from a single emitter, whereas in the Hopfield model, the excitation of matter is described in terms of bosons as collective excitations. Still, the effective coupling strength $G = \sqrt{N}g$ increases proportionally to the square root of N . Thanks to the collective enhancement of the coupling, several setups achieve the (deep) ultrastrong coupling regime $G/\Omega \sim \mathcal{O}(0.1)$ ($\mathcal{O}(1)$) even when the coupling strength at one emitter level g is not so strong.

1.2 Cavity polariton

Cavity polaritons are commonly described as light-matter hybrid quasiparticles in a cavity, where both light and matter contribute to the formation of polariton. More precisely, a cavity polariton is a quantum mechanical superposition of a cavity photon and a collective matter excitation, such as a collective excitation in solids, an electronic excitation in atoms or molecules, or an excitation in superconducting qubits. As such, the notion of cavity polaritons is a universal concept in cavity QED. Cavity polaritons have potential applications in various fields, including quantum computing [18, 19] and optoelectronics [20]. In this thesis, we focus on the fundamental properties of cavity polaritons, which are distinct from their individual components. In the following, we explain the phenomena unique to cavity polaritons: vacuum Rabi splitting and virtual photons.

1.2.1 Vacuum Rabi splitting

In the strong coupling regime, one can observe an oscillatory exchange of energy quanta between matter and photons before they are lost from the cavity. This oscillation is called vacuum Rabi oscillation, and its signal in the frequency domain is called vacuum Rabi splitting because the single signal without the cavity splits into two signals within the cavity.

In order to understand the vacuum Rabi splitting, the Hopfield model with the rotating wave approximation is often used as a minimal model,

$$\hat{H}_{\text{Hopfield}} = \Omega_c \hat{a}^\dagger \hat{a} + \Omega_0 \hat{b}^\dagger \hat{b} + G (\hat{a}^\dagger \hat{b} + \hat{a} \hat{b}^\dagger). \quad (1.6)$$

In the rotating wave approximation, we neglect the counter-rotating term, $g(\hat{a}^\dagger \hat{b}^\dagger + \hat{a} \hat{b})$, but keep the rotating term, $g(\hat{a}^\dagger \hat{b} + \hat{a} \hat{b}^\dagger)$. We can solve this Hamiltonian because the Hamiltonian conserves the excitation number $\hat{N}_{\text{ext}} = \hat{a}^\dagger \hat{a} + \hat{b}^\dagger \hat{b}$. If we focus on the Hilbert space of $\hat{N}_{\text{ext}} = 1$, the bases are matter excitation with no photon $|e, 0\rangle$ and no matter excitation with a one photon $|g, 1\rangle$. Therefore, the Hamiltonian is expressed by a two-by-

two matrix, and its eigenenergy and eigenstates are solved as,

$$\hat{H}_{\text{Hopfield}, N_{\text{ext}}=1} = \begin{pmatrix} \Omega_c & G \\ G & \Omega_0 \end{pmatrix}, \quad (1.7)$$

$$\rightarrow E_{\pm} = \frac{\Omega_c + \Omega_0}{2} \pm \sqrt{\delta^2 + G^2}, \quad (1.8)$$

$$|+\rangle = \cos(\alpha) |g, 1\rangle + \sin(\alpha) |e, 0\rangle, \quad (1.9)$$

$$|-\rangle = \sin(\alpha) |g, 1\rangle + \cos(\alpha) |e, 0\rangle, \quad (1.10)$$

where the detuning parameter δ and the angle α are defined through

$$\delta = \frac{\Omega_c - \Omega_0}{2}, \quad (1.11)$$

$$\tan(\alpha) = \frac{\delta + \sqrt{\delta^2 + G^2}}{G}. \quad (1.12)$$

When the cavity frequency resonates to the two-level system ($\delta = 0$), the eigenenergy Ω_c splits into $\Omega_c \pm G$. Corresponding eigenstates $|+\rangle$ and $|-\rangle$ are in the form of the hybridization between a photon and matter excitation (cavity polariton).

In the strong coupling regime, the splitting width $2G$ is not hidden by the broadening of the signal κ . Therefore, this splitting signal can be observed by measuring the excitation signal of the cavity or matter in experiments. The vacuum Rabi splitting has been observed in several experimental setups, [10–14] and the coupling strength of the system is determined by obtaining the splitting width.

1.2.2 Virtual photons

The ground state of the Hopfield model with the rotating wave approximation is the state with no matter excitation and no photon $|g, 0\rangle$, since \hat{N}_{ext} is the conserved quantity. The rotating wave approximation is justified due to the presence of fast and slow oscillating components in the couplings. In the interaction picture, the rotating term oscillates as $e^{\pm i(\Omega_c - \Omega_0)t}$, and the counter-rotating term oscillates as $e^{\pm i(\Omega_c + \Omega_0)t}$. The latter oscillates faster than the former, so the counter-rotating term can be neglected in the rotating wave approximation.

However, this approximation breaks down in an ultrastrong coupling regime because the exchange between matter excitations and photons is also fast. In this regime, there appears deviations between the exact results and the rotating wave approximation. One deviation is the energy shift of the order of $\frac{g^2}{\Omega_c + \Omega_0}$ in the Rabi splitting, known as the Bloch-Siegert shift [21]. This shift has been observed in some experiments [22, 23]. Another deviation is that photons are present even in the ground state because \hat{N}_{ext} is not conserved anymore. In this way, photons that appear in the ground state are called virtual photons, as C. Ciuti and colleagues have pointed out in 2005 [24]. Although there has not been direct experimental evidence for virtual photons yet, there are several theoretical proposals [25, 26] to observe it in experiments.

In relation to the virtual photons, the intrinsic squeezing that appears in the ultrastrong coupling regime is also important. Here, the *intrinsic* nature lies in the fact that

squeezing exists even in the ground state of the coupled light-matter system without any external driving. The squeezing arises from the diamagnetic term in the form of $D(\hat{a}^\dagger + \hat{a})^2$. This coefficient is typically proportional to the square of the coupling strength. Therefore, intrinsic squeezing is essential in the ultrastrong coupling regime. The virtual photons also appear by squeezing because the expectation value of the photon number operator in the squeezed vacuum state is non-zero.

1.3 Cavity quantum material

Apart from the development of cavity QED, the control of quantum materials with charge, spin, orbital, and lattice degrees of freedom through an external driving field has been investigated in recent years. For example, material control with the periodic driving of classical light known as Floquet engineering [27, 28] or short and intense laser pulses [29, 30] has been reviewed recently. This driving field is regarded as classical light in which many photons created by a laser occupy a macroscopic coherent state. It is incorporated into the theory not as a dynamical degree of freedom of the system but as a control parameter for the system. Moreover, material driving using classical light cannot avoid the heating effects due to energy injection, so material control with the driving field is typically realized in a transient nonequilibrium regime.

In contrast cavity QED treat the light as the system's degrees of freedom. Light and matter interact with each other to form the ground state and the excited states. In addition, cavity QED utilizes vacuum fluctuations of photons in the ground state, offering a potential platform for stable material control. In traditional cavity QED, systems have been described as simple ensembles of independent two-level atoms, as in the Dicke model. However, there is still much room to study how the properties of light and matter can change when complex quantum materials are confined within a cavity.

Based on these backgrounds, a new field called cavity quantum materials [31] has emerged, and has been actively studied in recent years. This new emerging field has focused on the intersection between quantum materials and quantum optics [32, 33]. For example, the cavity-modified carrier mobility has been reported experimentally in organic semiconductors [34] and two-dimensional electron gases [35]. The breakdown of topological protection of edge states under the strong light-matter coupling [36] and Bose-Einstein condensation of exciton polaritons in semiconductors [37] have also attracted considerable attention. From the viewpoint of phase transitions in condensed matter physics, there have been reports on the metal-insulator transition [38] and the change of superconducting critical temperatures [39] in cavity quantum materials, whose origin and interpretation are still under debate. Theoretically, there are several proposals on a new pairing mechanism of superconductivity [40], cavity-enhanced ferroelectric phase transition [41], and cavity control of magnetic frustration [42]. Additionally, the newly emerging concepts, such as cavity-mediated long-range interactions [43], control of topological properties by chiral cavity [44], and quantum Floquet engineering [45] are also a fascinating frontier in cavity quantum materials.

Strongly correlated materials are particularly important in the study of quantum materials, because they exhibit rich properties that cannot be simply explained by the band

theory due to the strong interactions between electrons. In these materials, the collective behavior of electrons is crucial, where quantum many-body effects play an important role. This leads to physical phenomena such as the Mott transition, the high-temperature superconductivity, and the quantum Hall effect. Strongly correlated materials in cavities are still not well-studied among cavity quantum materials due to their difficulties in the analysis. In this thesis, we focus on the one-dimensional extended Hubbard model (1DEHM) as a prototype of a model of strongly correlated materials. In the following, we review the 1DEHM.

1.3.1 One-dimensional extended Hubbard model

The 1DEHM describes interacting electrons on a lattice and incorporates additional terms to account for long-range interactions beyond the on-site interactions of the standard Hubbard model:

$$\begin{aligned}\hat{H} = & -t \sum_{j,\sigma} (\hat{c}_{j,\sigma}^\dagger \hat{c}_{j+1,\sigma} + \text{h.c.}) \\ & + U \sum_j \hat{n}_{j,\uparrow} \hat{n}_{j,\downarrow} + V \sum_j \hat{n}_j \hat{n}_{j+1},\end{aligned}\quad (1.13)$$

where $c_{i,\sigma}^\dagger$ ($\hat{c}_{i,\sigma}$) is the creation (annihilation) operator of an electron with spin σ at site i , and $n_{i,\sigma} = c_{i,\sigma}^\dagger \hat{c}_{i,\sigma}$ is the number operator. t is the nearest-neighbor hopping term and U (V) is the on-site (nearest-neighbor) Coulomb interaction. Despite its simplicity, this model exhibits various phases at half-filling due to strong quantum fluctuations depending on the relationship among t, U and V . On-site repulsion U favors the localization of electrons, while the nearest-neighbor interaction V promotes charge ordering. Due to their competition, the ground state of this model exhibits the spin-density wave (SDW) phase (Mott insulator phase) for $V \lesssim U/2$ and a charge-density wave (CDW) phase for $V \gtrsim U/2$ [46]. The SDW has staggered spin arrangements of up and down while the CDW also has staggered charge arrangements of doublon (doubly occupied site) and holon (empty site). There is also the bond-order wave (BOW) phase between the CDW and SDW phases based on numerical results [47]. This BOW phase is characterized by alternating strengths of the expectation value of the local kinetic energy on the bond. The ground state phase diagram of the 1DEHM in the previous numerical study is shown in Fig. 1.2a

Not only the ground state properties but also the dynamical properties of the 1DEHM have been intensively investigated, because excitation spectra, such as the optical conductivity, reflect the structure of many-body excited states [48–51]. For $V > 2t$ in the SDW phase, a sharp peak emerges in the optical conductivity, which corresponds to the energy of the doublon-holon bound state (exciton) and the peak position decreases as V increases. The optical conductivity in the CDW phase also shows a sharp excitation peak which corresponds to the energy of dissociation of the CDW and the peak position increases as V increases. The optical conductivity of the 1DEHM in the previous numerical study is shown in Fig. 1.2b.

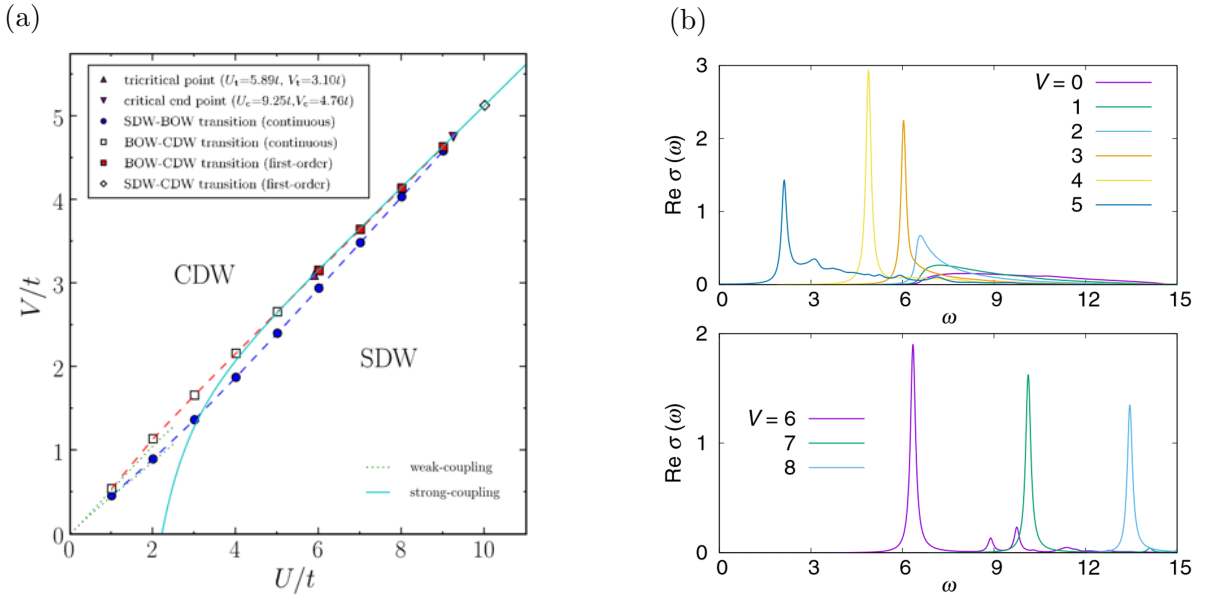


Figure 1.2: (a) Phase diagram of the 1DEHM at half-filling based on the DMRG method [46]. The SDW phase appears when $V \lesssim U/2$, and the CDW phase appears when $V \gtrsim U/2$. The BOW phase appears in between the SDW and CDW phases. The weak-coupling renormalization group results (green dot line) and the strong-coupling perturbation result (blue solid line) are also shown. (b) Real part of the optical conductivity of the 1DEHM for $U = 10$ and $t = 1$ based on the TEBD method with infinite boundary condition [48]. The top panel is the optical conductivity for the SDW phase at $V \lesssim U/2$. The bottom panel is the optical conductivity for the CDW phase at $V \gtrsim U/2$.

While the 1D Hubbard model is exactly solvable by Bethe Anzatz, the 1DEHM is no longer integrable. Therefore, various numerical studies have been performed to understand the 1DEHM. For example, there has been studies using the density matrix renormalization group (DMRG) method [52, 53] and related numerical techniques, such as the dynamical DMRG [54] or time-evolving block decimation (TEBD) method [55], which have been developed to simulate one-dimensional quantum systems.

We also comment that organic salt [56, 57] and halogen-bridged transition-metal compounds [58, 59] have been considered to realize the 1DEHM, where the optical properties of the materials have been studied, and these experimental data have been compared with the 1DEHM.

1.4 Purpose of the thesis

Cavity quantum material is an emerging field, and it is important to investigate the properties of complex quantum many-body systems in a cavity. In particular, it has not yet been fully explored cavity polariton in strongly correlated materials. We can deepen our understanding of cavity quantum materials by investigating how the effects of electron motion and Coulomb interactions, which are not considered in the Dicke model, are reflected in the properties of polaritons.

As one of the simplest models of the strongly correlated materials, we consider the 1DEHM. The 1DEHM exhibits various phases depending on the strength of Coulomb interactions and hopping amplitude. We research the relationship between the phases and phenomena of the virtual photon and Rabi splitting by exploiting the DMRG and TEBD methods.

1.5 Outline of the thesis

The outline of this thesis is as follows. In Chap. 2, we summarize the model and numerical methods. In the first part, we review the derivation of the lattice model coupled with a single-mode cavity. Then, we introduce the 1DEHM coupled with a single-mode cavity, which we investigate in this thesis. The remaining parts are devoted to the explanation of the DMRG and the TEBD methods employed in this study. We also introduce special techniques in the DMRG and the TEBD methods to deal with the global coupling of the cavity photon and electron. Our original results are given in Chap. 3 and Chap. 4. In Chap. 3, we show the numerical results of the ground state using the DMRG method. We calculate and discuss how the virtual photons appear in the ground state depending on the Colomb interaction and coupling strength. Numerical results of the excited state using the TEBD method are shown in Chap. 4. We calculate the optical conductivity and discuss how the excitation signal changes with and without a cavity. In Chap. 5, we summarize our results and discuss future directions of our work.

Chapter 2

Model and Numerical Methods

In this chapter, we introduce the model and review the numerical methods. In the first section, we review the derivation of the lattice model coupled with a single-mode cavity, and introduce the one-dimensional extended Hubbard model (1DEHM) coupled with a single-mode cavity. We also briefly review a previous related study that treats the non-interacting tight-binding model coupled with a single-mode cavity. The remaining section is devoted to numerical methods. It is difficult to deal with the ground state and the excited states of strongly correlated systems, and treating those with cavity degrees of freedom is even more challenging. However, in one-dimensional systems, we can use the density matrix renormalization group (DMRG) method and the time-evolving block decimation (TEBD) method, which are powerful numerical tools to treat the ground state and time-dependent states, respectively. These methods are based on the matrix product state (MPS). An overview of the MPS is given in the second section. In the third section, a review of the DMRG method is presented. We also explain how to treat the photon degrees of freedom in the DMRG method. In the fourth section, the TEBD method is reviewed. It is explained how to treat the global coupling term of the cavity-matter interaction in the TEBD algorithm.

2.1 One-dimensional extended Hubbard model coupled with an optical cavity

As the previous chapter shows, the Dicke model has been formulated by considering the emitters as independent two-level systems. However, many solid-state electron systems cannot be regarded as simple two-level systems. In solid-state systems, electrons can hop between atoms and experience Coulomb interactions with one another. In order to describe such complex phenomena, it is useful to consider lattice models, which are effective low-energy models. It is important that the electromagnetic field properly couples with these lattice models to preserve gauge invariance. In the following, we derive the lattice model coupled with a single-mode cavity that maintains the gauge invariance based on the previous study [60]. As a specific example, we introduce the 1DEHM coupled with a single-mode cavity.

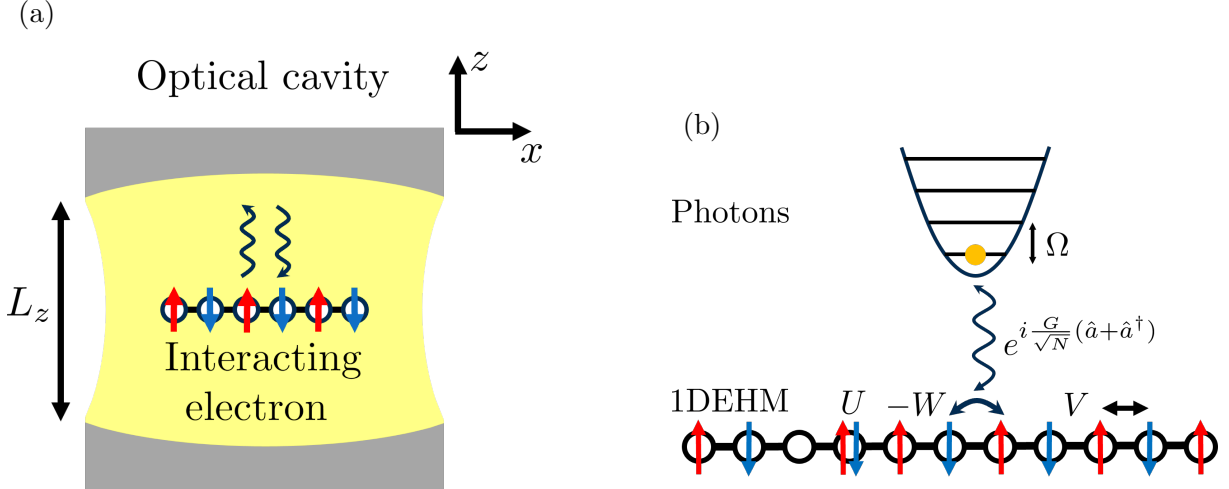


Figure 2.1: (a) Schematic picture of the one-dimensional interacting electron system confined in the cavity of length L_z . The cavity mirror is placed in parallel to the electron system. (b) Schematic picture of the 1DEHM coupled with an optical cavity. Electrons can hop to the nearest-neighbor site with the hopping amplitude W . Photons undergo excitation or de-excitation when an electron hops through the Peierls phase. Up-spin and down-spin electrons on the same site feel the Coulomb interaction U , and electrons between nearest-neighbor sites feel the Coulomb interaction V .

2.1.1 Derivation of the model

In order to introduce the 1DEHM coupled with an optical cavity, we first consider a one-dimensional electron system confined in a three-dimensional cavity. The one-dimensional interacting electrons are arranged in the x direction, and the cavity mirror is placed in the z direction, as shown in Fig. 2.1a. We take the Coulomb gauge $\nabla \cdot \hat{A}(x) = 0$, which gives the minimal coupling Hamiltonian ($\hbar = 1$),

$$\hat{H} = \hat{H}_{\text{kin},A} + \hat{H}_{\text{int}} + \hat{H}_{\text{photon}}, \quad (2.1)$$

$$\hat{H}_{\text{kin},A} = \sum_{\sigma} \int dx \hat{\Psi}_{\sigma}^{\dagger}(x) \left(\frac{(-i\partial_x + e\hat{A}(x))^2}{2m} + V(x) \right) \hat{\Psi}_{\sigma}(x), \quad (2.2)$$

$$\hat{H}_{\text{int}} = \sum_{\sigma, \sigma'} \frac{1}{2} \int dx \int dx' \frac{e^2}{4\pi\epsilon|x-x'|} \hat{\Psi}_{\sigma}^{\dagger}(x) \hat{\Psi}_{\sigma'}^{\dagger}(x') \hat{\Psi}_{\sigma'}(x') \hat{\Psi}_{\sigma}(x), \quad (2.3)$$

$$\hat{H}_{\text{photon}} = \sum_k \Omega(k) \hat{a}_k^{\dagger} \hat{a}_k, \quad (2.4)$$

where

$$\hat{A}(x) = \sum_k \sqrt{\frac{1}{2\epsilon V_c \Omega(k)}} (u_k \hat{a}_k e^{ikx} + u_k^* \hat{a}_k^{\dagger} e^{-ikx}), \quad (2.5)$$

$$\Omega(k) = c \sqrt{k_z^2 + k^2} = c \sqrt{(\pi n/L_z)^2 + k^2}. \quad (2.6)$$

Electrons with charge e and mass m are trapped in an atomic potential $V(x)$. ϵ is the dielectric constant in the system. $\hat{\Psi}_\sigma(x)$ is the annihilation operators of an electron with spin σ at the position x , which satisfy the anti-commutation relation,

$$\left\{ \hat{\Psi}_\sigma(x), \hat{\Psi}_{\sigma'}^\dagger(x') \right\} = \delta(x - x') \delta_{\sigma, \sigma'}. \quad (2.7)$$

The cavity has a volume V_c , and the z -directional length is L_z . The wavenumbers in z direction k_z are quantized into $\pi n/L_z$ ($n = 0, \pm 1, \pm 2, \dots$), since electromagnetic fields must have nodes at the cavity mirror position. The electromagnetic fields with other wavenumbers vanish due to interference. \hat{a}_k is the annihilation operator of an photon with the wavenumber k , which satisfies the commutation relation,

$$[\hat{a}_k, \hat{a}_{k'}] = \delta_{k, k'}. \quad (2.8)$$

The Hamiltonian (2.1) satisfies the gauge invariance, which means that the Hamiltonian is invariant under the gauge transformation as

$$\hat{\Psi}_\sigma(x) \rightarrow e^{i\Lambda(x)} \hat{\Psi}_\sigma(x), \quad (2.9)$$

$$\hat{A}(x) \rightarrow \hat{A}(x) - \frac{1}{e} \frac{\partial}{\partial x} \Lambda(x). \quad (2.10)$$

In order to check the gauge invariance, we rewrite the kinetic term as

$$\begin{aligned} \hat{H}_{\text{kin}, A} &= \sum_\sigma \int dx \hat{\Psi}_\sigma^\dagger(x) e^{-i\hat{\chi}(x)} \left(\frac{(-i\partial_x)^2}{2m} + V(x) \right) e^{i\hat{\chi}(x)} \hat{\Psi}_\sigma(x) \\ &= \sum_\sigma \int dx (\hat{U}_\chi^\dagger \hat{\Psi}_\sigma^\dagger(x) \hat{U}_\chi) \left(\frac{(-i\partial_x)^2}{2m} + V(x) \right) (\hat{U}_\chi^\dagger \hat{\Psi}_\sigma(x) \hat{U}_\chi) \\ &= \hat{U}_\chi^\dagger \sum_\sigma \int dx \hat{\Psi}_\sigma^\dagger(x) \left(\frac{(-i\partial_x)^2}{2m} + V(x) \right) \hat{\Psi}_\sigma(x) \hat{U}_\chi \\ &= \hat{U}_\chi^\dagger \hat{H}_{\text{kin}, 0} \hat{U}_\chi, \end{aligned} \quad (2.11)$$

where we introduce a unitary operator as

$$\hat{U}_\chi = \exp \left[i \sum_\sigma \int dx \hat{\Psi}_\sigma^\dagger(x) \hat{\chi}(x) \hat{\Psi}_\sigma(x) \right], \quad (2.12)$$

$$\frac{\partial}{\partial x} \hat{\chi}(x) = e \hat{A}(x). \quad (2.13)$$

In the second line of Eq. (2.11), we use the transformation of the electron annihilation operator under the action of \hat{U}_χ :

$$\begin{aligned} \hat{U}_\chi^\dagger \hat{\Psi}_\sigma(x) \hat{U}_\chi &= \hat{\Psi}_\sigma(x) + [i\hat{s}, \hat{\Psi}_\sigma(x)] + \frac{1}{2!} [i\hat{s}, [i\hat{s}, \hat{\Psi}_\sigma(x)]] + \dots \\ &= e^{i\hat{\chi}(x)} \hat{\Psi}_\sigma(x), \end{aligned} \quad (2.14)$$

$$i\hat{s} = -i \sum_\sigma \int dx \hat{\Psi}_\sigma^\dagger(x) \hat{\chi}(x) \hat{\Psi}_\sigma(x). \quad (2.15)$$

The gauge invariance is automatically satisfied when we keep the form of Eq. (2.11). The reason is that $\hat{U}_\chi^\dagger \hat{\Psi}_\sigma(x) \hat{U}_\chi$ is invariant under the gauge transformation as

$$\begin{aligned}\hat{U}_\chi^\dagger \hat{\Psi}_\sigma(x) \hat{U}_\chi &\rightarrow \hat{U}_{\chi-\Lambda}^\dagger e^{i\Lambda(x)} \hat{\Psi}_\sigma(x) \hat{U}_{\chi-\Lambda} \\ &= \hat{U}_\chi^\dagger e^{i\Lambda(x)} (\hat{U}_{-\Lambda}^\dagger \hat{\Psi}_\sigma(x) \hat{U}_{-\Lambda}) \hat{U}_\chi \\ &= \hat{U}_\chi^\dagger \hat{\Psi}_\sigma(x) \hat{U}_\chi.\end{aligned}\quad (2.16)$$

In order to obtain an effective lattice Hamiltonian, we take several approximations in the Hamiltonian. The first one is made in the cavity photon part. We neglect modes that have wavenumbers with non-zero components in the direction of the chain. This approximation is called the long-wavelength approximation or dipole approximation, which is justified in cases where the size of the matter system is much smaller than the wavelength of the electromagnetic field. In the one-dimensional system, this condition means that the spatial extension of the material in the x direction is much smaller than the wavelength of the cavity mode. Moreover, the main contribution of the cavity mode is the first transmittance resonance of a cavity because we are interested in low-energy physics. This means that we take into account the z direction wavenumber $k_z = \pi/L_z$ only. Under these approximations, the quantized vector potential and the photon part of the Hamiltonian are simplified as

$$\hat{A}(x) \rightarrow \hat{A} = A_0(\hat{a} + \hat{a}^\dagger), \quad (2.17)$$

$$\hat{H}_{\text{photon}} \rightarrow \Omega \hat{a}^\dagger \hat{a}, \quad (2.18)$$

where we define $\Omega = c\pi/L_z$, $A_0 = \sqrt{\frac{1}{2\epsilon V_c \Omega}}$.

The second approximation is made in the matter part. In order to construct a lattice model from the continuous model, let us introduce the Bloch function $\phi_k(x)$ and the Wannier function $w_i(x)$ through the following relations:

$$\left(\frac{(-i\partial_x)^2}{2m} + V(x) \right) \phi_k(x) = \varepsilon_k \phi_k(x), \quad (2.19)$$

$$w_i(x) = \frac{1}{\sqrt{N}} \sum_k \phi_k(x). \quad (2.20)$$

Here, k is the label of the wavenumber of the Bloch function, which extends across the entire system. Therefore, the Wannier function $w_i(x)$, the Fourier transform of the Bloch function $\phi_k(x)$, is localized around the i -site atom position R_i . We can write the field operator $\hat{\Psi}_\sigma(x)$ with the Wannier function as

$$\hat{\Psi}_\sigma(x) = \sum_i w_i(x) \hat{c}_{i,\sigma}, \quad (2.21)$$

where $\hat{c}_{i,\sigma}$ is the annihilation operator of an electron in the Wannier orbital $w_i(x)$ with spin σ , which satisfies the anti-commutation relation as

$$\left\{ \hat{c}_{i,\sigma}, \hat{c}_{j,\sigma'}^\dagger \right\} = \delta_{i,j} \delta_{\sigma,\sigma'}. \quad (2.22)$$

Then, we can express the kinetic term and the unitary operator in Eq. (2.11) using the $\hat{c}_{i,\sigma}$ as

$$\hat{H}_{\text{kin},0} = - \sum_{i,j,\sigma} W_{i,j} \hat{c}_{i,\sigma}^\dagger \hat{c}_{j,\sigma}, \quad (2.23)$$

$$\hat{U}_\chi = \exp \left[ieA_0(\hat{a} + \hat{a}^\dagger) \sum_{i,j,\sigma} \chi_{i,j} \hat{c}_{i,\sigma}^\dagger \hat{c}_{j,\sigma} \right] \quad (2.24)$$

with the coefficients

$$W_{i,j} = - \int dx w_i^*(x) \left(\frac{(-i\partial_x)^2}{2m} + V(x) \right) w_j(x), \quad (2.25)$$

$$\begin{aligned} \chi_{i,j} &= \int dx w_i^*(x) x w_j(x) \\ &= R_i \delta_{i,j} + \int dx w_i^*(x) (x - R_i) w_j(x). \end{aligned} \quad (2.26)$$

Due to the localization of the Wannier basis, we can assume that $W_{i,j}$ is non-zero for $i = j, j \pm 1$. We can set the $W_{j,j}$ to zero because $W_{j,j}$ induces a homogeneous on-site potential, which has a constant energy shift. We can also assume that $\int dx w_i^*(x)(x - R_i)w_j(x)$ is zero. Under these assumptions, we can map the continuum Hamiltonian into the lattice one while keeping the gauge invariance. The kinetic term becomes

$$\begin{aligned} \hat{H}_{\text{kin},A} &= \hat{U}_\chi^\dagger \left(-W \sum_{j,\sigma} (\hat{c}_{j,\sigma}^\dagger \hat{c}_{j+1,\sigma} + \text{h.c.}) \right) \hat{U}_\chi \\ &= -W \sum_{j,\sigma} \left((\hat{U}_\chi^\dagger \hat{c}_{j,\sigma}^\dagger \hat{U}_\chi) (\hat{U}_\chi^\dagger \hat{c}_{j+1,\sigma} \hat{U}_\chi) + \text{h.c.} \right) \\ &= -W \sum_j \left(e^{ieA_0(\hat{a}+\hat{a}^\dagger)a_0} \hat{c}_{j,\sigma}^\dagger \hat{c}_{j+1,\sigma} + \text{h.c.} \right) \\ &= -W \sum_j \left(e^{i\frac{G}{\sqrt{N}}(\hat{a}+\hat{a}^\dagger)} \hat{c}_{j,\sigma}^\dagger \hat{c}_{j+1,\sigma} + \text{h.c.} \right), \end{aligned} \quad (2.27)$$

where a_0 , N , and W are the atomic spacing, the number of electrons, and the hopping amplitude to the nearest-neighbor site $W_{j,j+1}$, respectively. $G = ea_0\sqrt{N}A_0 = \sqrt{\frac{e^2 a_0^2 N}{2\epsilon V_c \Omega}}$ is the collective coupling constant. In the third line of Eq. (2.27), we use the transformation of the electron annihilation operator under the action of \hat{U}_χ :

$$\begin{aligned} \hat{U}_\chi^\dagger \hat{c}_{j,\sigma} \hat{U}_\chi &= \hat{c}_{j,\sigma} + [i\hat{s}, \hat{c}_{j,\sigma}] + \frac{1}{2!} [i\hat{s}, [i\hat{s}, \hat{c}_{j,\sigma}]] + \dots \\ &= e^{ieA_0(\hat{a}+\hat{a}^\dagger)R_j} \hat{c}_{j,\sigma}, \end{aligned} \quad (2.28)$$

$$i\hat{s} = -ieA_0(\hat{a} + \hat{a}^\dagger) \sum_{i,\sigma} R_i \hat{c}_{i,\sigma}^\dagger \hat{c}_{i,\sigma}. \quad (2.29)$$

$e^{i\frac{G}{\sqrt{N}}(\hat{a}+\hat{a}^\dagger)}$ is the quantized version of Peierls substitution, which is widely used in solid-state physics when vector potential is a classical c-number. In the same way, H_{int} can also be expressed with the Wannier basis as

$$H_{\text{int}} = \frac{1}{2} \sum_{i,j,k,l,\sigma,\sigma'} U_{i,j,k,l} c_{i,\sigma}^\dagger c_{j,\sigma'}^\dagger c_{k,\sigma'} c_{l,\sigma} \quad (2.30)$$

with the Coulomb interaction coefficient

$$U_{i,j,k,l} = \int dx \int dx' \frac{e^2}{4\pi\epsilon|x-x'|} w_i^*(x) w_j^*(x') w_k(x') w_l(x). \quad (2.31)$$

Note that the Peierls phase does not appear in the Coulomb interaction because H_{int} does not include the differential term. The coefficient of the Coulomb interaction is monotonically decreasing as i, j, k and l become farther apart from each other because of the localization of the Wannier basis. If we only include the contribution of the on-site Coulomb interaction $U_{i,i,i,i} =: U$ and the nearest-neighbor Coulomb interaction $U_{i,j,j,i} =: V$, we reach the Hamiltonian on a lattice :

$$\begin{aligned} \hat{H} = & \Omega \hat{a}^\dagger \hat{a} - W \sum_{j,\sigma} (e^{i\frac{G}{\sqrt{N}}(\hat{a}+\hat{a}^\dagger)} \hat{c}_{j,\sigma}^\dagger \hat{c}_{j+1,\sigma} + \text{h.c.}) \\ & + U \sum_j \hat{n}_{j,\uparrow} \hat{n}_{j,\downarrow} + V \sum_j \hat{n}_j \hat{n}_{j+1}, \end{aligned} \quad (2.32)$$

where $n_{i,\sigma} = \hat{c}_{i,\sigma}^\dagger \hat{c}_{i,\sigma}$ is the electron number operator at site i with spin σ and $n_i = n_{i,\uparrow} + n_{i,\downarrow}$ is the summation over spins. Due to the Pauli exclusion principle, electrons with the same spin cannot occupy the same site. This model is what we focus on in this thesis. In this model, cavity photons globally couple to electrons through the Peierls phase as shown in Fig. 2.1b.

In this thesis, we treat the model with several U, V regions using the DMRG and TEBD methods. However, the specific case of $U = V = 0$, i.e., a non-interacting tight-binding model coupled with a single-mode cavity, has been well studied in a previous study using a different numerical approach [61]. Since several analytical methods of the previous study are also used in this thesis, we briefly review the previous study in the following.

2.1.2 Non-interacting tight-binding model coupled with an optical cavity

C. J. Eckhardt *et al.* [61] have studied the non-interacting (spinless) tight-binding model coupled with a single mode cavity based on a variational scheme. The eigenstates of the Hamiltonian can be written as the product state of a fermion state $|\psi\rangle_f$ and a photon state $|\phi\rangle_b$, since the Hamiltonian commutes with the number operator of fermions with quasi-momentum k , namely $\hat{\rho}_k = \hat{c}_k^\dagger \hat{c}_k$ and $[\hat{\rho}_k, \hat{H}] = 0$. Using the variational method, they search for the optimal fermion and photon states to minimize the energy. As a result,

the energy minimum can be found when the Fermi sea is centered around $k = 0$, and the photon state is squeezed vacuum. This result can be explained through the following discussions. If there is no photon condensation¹, the expansion of the Peierls substitution up to the second order is relevant in the thermodynamic limit,

$$\begin{aligned} \langle \Psi_{\text{GS}} | \hat{H} | \Psi_{\text{GS}} \rangle &= \underbrace{\langle \Psi_{\text{GS}} | \hat{T} | \Psi_{\text{GS}} \rangle}_{\sim N} + \underbrace{\langle \Psi_{\text{GS}} | \frac{G}{\sqrt{N}} \hat{J}(\hat{a} + \hat{a}^\dagger) | \Psi_{\text{GS}} \rangle}_{\sim \sqrt{N}} \\ &\quad - \underbrace{\langle \Psi_{\text{GS}} | \frac{1}{2} \frac{G^2}{N} \hat{T}(\hat{a} + \hat{a}^\dagger)^2 | \Psi_{\text{GS}} \rangle}_{\sim 1} + \underbrace{\langle \Psi_{\text{GS}} | \Omega \hat{a}^\dagger \hat{a} | \Psi_{\text{GS}} \rangle}_{\sim 1} \\ &\quad + \mathcal{O}\left(\frac{1}{\sqrt{N}}\right), \end{aligned} \quad (2.33)$$

where $|\Psi_{\text{GS}}\rangle = |\psi_{\text{GS}}\rangle_f \otimes |\phi_{\text{GS}}\rangle_b$ is the ground state of the system, and a kinetic energy operator and a current operator are introduced as

$$\hat{T} = -W \sum_j (\hat{c}_j^\dagger \hat{c}_{j+1} + \text{h.c.}) = -2W \sum_k \cos(k) \hat{c}_k^\dagger \hat{c}_k, \quad (2.34)$$

$$\hat{J} = -Wi \sum_j (\hat{c}_j^\dagger \hat{c}_{j+1} - \text{h.c.}) = -2W \sum_k \sin(k) \hat{c}_k^\dagger \hat{c}_k. \quad (2.35)$$

Provided that the fermionic part of the ground state $|\psi_{\text{GS}}\rangle_f$ is the unshifted Fermi sea, one can replace the kinetic operator and current operator as $\langle \psi_{\text{GS}} | \hat{T} | \psi_{\text{GS}} \rangle_f \rightarrow t_{\text{GS}} N$ and $\langle \psi_{\text{GS}} | \hat{J} | \psi_{\text{GS}} \rangle_f \rightarrow 0$. Then, one can diagonalize the photonic part of the Hamiltonian using the squeezed transformation, and find that the ground state of photons is the squeezed vacuum state $|\phi_{\text{GS}}\rangle_b = \hat{S}(\zeta) |0\rangle$,

$$_f \langle \psi_{\text{GS}} | \hat{H} | \psi_{\text{GS}} \rangle_f = \tilde{\Omega} \hat{S}(\zeta) \hat{a}^\dagger \hat{a} \hat{S}^\dagger(\zeta) - |t_{\text{GS}}| N, \quad (2.36)$$

$$\hat{S}(\zeta) = e^{\frac{\zeta}{2}(\hat{a}^2 - \hat{a}^{\dagger 2})}, \quad (2.37)$$

$$\zeta = \frac{1}{2} \ln \left(\frac{\tilde{\Omega}}{\Omega} \right), \quad (2.38)$$

$$\tilde{\Omega} = \Omega \sqrt{1 + 2 \frac{G^2}{\Omega} |t_{\text{GS}}|}, \quad (2.39)$$

where ζ is the squeeze factor, $\tilde{\Omega}$ is the dressed cavity frequency and $|0\rangle$ is the cavity vacuum state. In the squeezed vacuum state, as the variance of the canonical momentum operator $P = i(\hat{a}^\dagger - \hat{a})$ increase, that of the canonical coordinate operator $X = (\hat{a}^\dagger + \hat{a})$ decreases (Fig. 2.2a). Moreover, one can also analytically calculate the spectral function and optical conductivity using the second-order expanded Hamiltonian. It is shown that

¹Photon condensation in the Dicke model is known as the superradiant phase transition (SRPT) [62]. However, the existence of SRPT is prohibited by the no-go theorem for the Dicke model with the diamagnetic term and also for more general models [63–67].

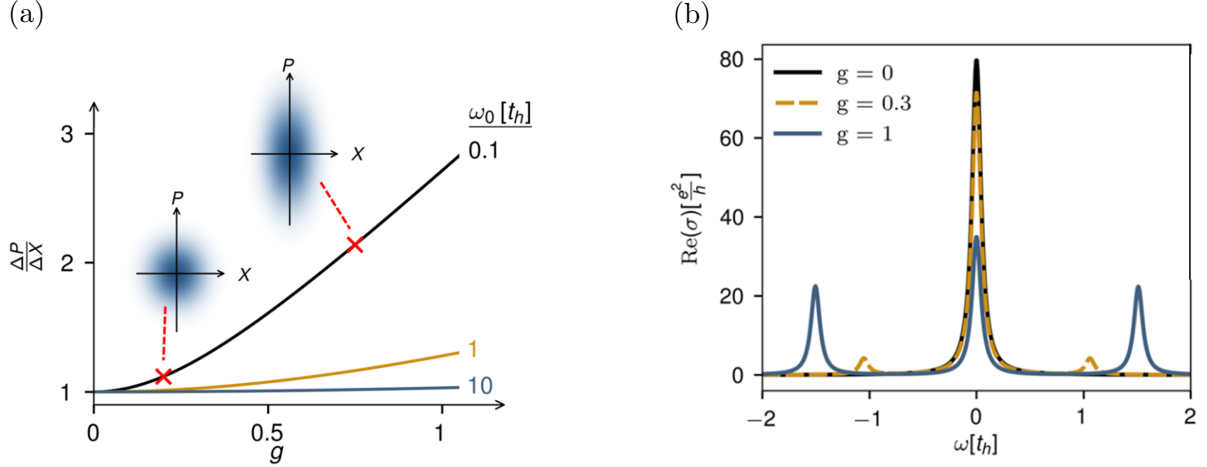


Figure 2.2: (a) The ratio of the variance of the canonical momentum and the coordinate operator $\Delta P / \Delta X$ in the ground state as a function of the coupling constant g for three different values of ω_0 [61]. Two inset figures represent squeezing ellipses. (b) The real part of the optical conductivity for the case of the zero coupling ($g = 0$, dark line), intermediate coupling ($g = 0.3$, dashed yellow line), and strong coupling ($g = 1$, dark blue line). The Drude peak is suppressed, and two new side peaks appear. t_h , g and ω_0 in the figure corresponds to the W , G and Ω in this thesis.

the spectral function in the thermodynamic limit is the same as that without the cavity. However, the optical conductivity dramatically changes even in the thermodynamic limit. The Drude peak is suppressed with increasing G , and the two side peaks, whose positions correspond to the dressed cavity frequency $\tilde{\Omega}$, appear at the same time (Fig. 2.2b).

2.2 Matrix Product state

The MPS is one of the well-understood tensor networks for which many efficient algorithms have been developed. The DMRG and TEBD methods are among the algorithms to treat one-dimensional many-body quantum systems. In this section, we review the MPS. First, we explain singular value decomposition (SVD) and Schmidt decomposition, which are important for understanding the structure of MPS. Next, we show how to construct the MPS form from a general pure state in a finite lattice system. Then, canonical conditions of MPS are stated.

2.2.1 Mathematical formulation for the MPS

The Schmidt decomposition is a way to decompose a state in Hilbert space into two parts, which is closely related to the principle of the MPS. To define the Schmidt decomposition, we first introduce SVD for general matrices.

SVD

Let M be an arbitrary $m \times n$ matrix. We introduce a $n \times n$ hermitian matrix $M^\dagger M$ and a $m \times m$ hermitian matrix MM^\dagger . Their eigenvalues and eigenvectors are defined as

$$M^\dagger M \mathbf{v}_i = \lambda_i \mathbf{v}_i \quad (i = 0, 1, \dots, n-1), \quad (2.40)$$

$$MM^\dagger \mathbf{u}_i = \lambda'_i \mathbf{u}_i \quad (i = 0, 1, \dots, m-1), \quad (2.41)$$

respectively. We define λ_i in the descending order, $\lambda_0 \geq \lambda_1 \geq \dots \geq \lambda_{n-1}$ (λ'_i is also in the descending order). λ_i and λ'_i are positive because

$$\lambda_i = \mathbf{v}_i^\dagger M^\dagger M \mathbf{v}_i = \|M \mathbf{v}_i\| \geq 0, \quad (2.42)$$

$$\lambda'_i = \mathbf{u}_i^\dagger MM^\dagger \mathbf{u}_i = \|M^\dagger \mathbf{u}_i\| \geq 0. \quad (2.43)$$

Let only r of the λ_i be non-zero, $\lambda_0 \geq \lambda_1 \geq \dots \geq \lambda_{r-1} > 0$. $r = \text{rank}(M^\dagger M) = \text{rank}(MM^\dagger)$ is satisfied because $\text{rank}(A^\dagger A) = \text{rank}(A)$ and $\text{rank}(A) = \text{rank}(A^\dagger)$ are satisfied in general. Therefore, only r of the λ'_i are also non-zero, $\lambda'_0 \geq \lambda'_1 \geq \dots \geq \lambda'_{r-1} > 0$. There are relations between λ_i and λ'_i and between \mathbf{v}_i and \mathbf{u}_i for $i = 0, 1, \dots, r-1$. In order to see the relation between λ_i and λ'_i , we calculate the same quantity in two different way as

$$\mathbf{u}_i^\dagger MM^\dagger M \mathbf{v}_i = \mathbf{u}_i^\dagger M(M^\dagger M \mathbf{v}_i) = \lambda_i \mathbf{u}_i^\dagger M \mathbf{v}_i \quad (2.44)$$

$$= (\mathbf{u}_i^\dagger MM^\dagger) M \mathbf{v}_i = \lambda'_i \mathbf{u}_i^\dagger M \mathbf{v}_i. \quad (2.45)$$

Therefore, we find $\lambda_i = \lambda'_i$ ($i = 0, 1, \dots, r-1$). In order to see the relation between \mathbf{v}_i and \mathbf{u}_i , we focus on the fact that $M \mathbf{v}_i$ is proportional to \mathbf{u}_i . This is because $M \mathbf{v}_i$ is the eigenvector of MM^\dagger , i.e.,

$$MM^\dagger(M \mathbf{v}_i) = \lambda_i M \mathbf{v}_i. \quad (2.46)$$

Then, we can write down \mathbf{u}_i using \mathbf{v}_i as

$$\mathbf{u}_i = \frac{M \mathbf{v}_i}{\sqrt{\mathbf{v}_i^\dagger M^\dagger M \mathbf{v}_i}} = \frac{M \mathbf{v}_i}{\sqrt{\lambda_i}} \quad (i = 0, 1, \dots, r-1). \quad (2.47)$$

For $i \geq r$, $M \mathbf{v}_i = M^\dagger \mathbf{u}_i = 0$ because

$$\|M \mathbf{v}_i\| = \mathbf{v}_i^\dagger M^\dagger M \mathbf{v}_i = \lambda_i = 0 \quad (i = r, r+1, \dots, n-1), \quad (2.48)$$

$$\|M^\dagger \mathbf{u}_i\| = \mathbf{u}_i^\dagger MM^\dagger \mathbf{u}_i = \lambda'_i = 0 \quad (i = r, r+1, \dots, m-1). \quad (2.49)$$

Combining Eq. (2.47), Eq. (2.48) and Eq. (2.49), we can obtain the matrix elements of M as

$$\mathbf{u}_i^\dagger M \mathbf{v}_j = \begin{cases} \frac{\mathbf{v}_i^\dagger M^\dagger M \mathbf{v}_j}{\sqrt{\lambda_i}} = \sqrt{\lambda_i} \delta_{i,j} & (i \leq r-1) \\ 0 & (i \geq r) \end{cases} \quad (2.50)$$

Next, we define two $m \times m$ and $n \times n$ unitary matrices as

$$\tilde{U} = (\mathbf{u}_0, \mathbf{u}_1, \dots, \mathbf{u}_{m-1}) \quad (2.51)$$

$$\tilde{V}^\dagger = (\mathbf{v}_0, \mathbf{v}_1, \dots, \mathbf{v}_{n-1}) \quad (2.52)$$

From Eq. (2.50) we obtain

$$\begin{aligned} \tilde{U}^\dagger M \tilde{V}^\dagger &= \begin{pmatrix} \mathbf{u}_0^\dagger M \mathbf{v}_0 & \mathbf{u}_0^\dagger M \mathbf{v}_1 & \cdots & \mathbf{u}_0^\dagger M \mathbf{v}_{r-1} & \cdots & \mathbf{u}_0^\dagger M \mathbf{v}_{n-1} \\ \mathbf{u}_1^\dagger M \mathbf{v}_0 & \mathbf{u}_1^\dagger M \mathbf{v}_1 & \cdots & \mathbf{u}_1^\dagger M \mathbf{v}_{r-1} & \cdots & \mathbf{u}_1^\dagger M \mathbf{v}_{n-1} \\ \vdots & \vdots & & \vdots & & \vdots \\ \mathbf{u}_{r-1}^\dagger M \mathbf{v}_0 & \mathbf{u}_{r-1}^\dagger M \mathbf{v}_1 & \cdots & \mathbf{u}_{r-1}^\dagger M \mathbf{v}_{r-1} & \cdots & \mathbf{u}_{r-1}^\dagger M \mathbf{v}_{n-1} \\ \vdots & \vdots & & \vdots & & \vdots \\ \mathbf{u}_{m-1}^\dagger M \mathbf{v}_0 & \mathbf{u}_{m-1}^\dagger M \mathbf{v}_1 & \cdots & \mathbf{u}_{m-1}^\dagger M \mathbf{v}_{r-1} & \cdots & \mathbf{u}_{m-1}^\dagger M \mathbf{v}_{n-1} \end{pmatrix} \\ &= \begin{pmatrix} \sqrt{\lambda_0} & 0 & \cdots & 0 & \cdots & 0 \\ 0 & \sqrt{\lambda_1} & \cdots & 0 & \cdots & 0 \\ \vdots & \vdots & & \vdots & & \vdots \\ 0 & 0 & \cdots & \sqrt{\lambda_{r-1}} & \cdots & 0 \\ \vdots & \vdots & & \vdots & & \vdots \\ 0 & 0 & \cdots & 0 & \cdots & 0 \end{pmatrix} =: \tilde{S} \end{aligned} \quad (2.53)$$

$$\therefore M = \tilde{U} \tilde{S} \tilde{V} \quad (2.54)$$

Since all the matrix elements of \tilde{S} beyond the r -th row and r -th column are zero, M can also be decomposed using a $r \times r$ diagonal matrix S as

$$M = USV \quad (2.55)$$

$$U = (\mathbf{u}_0, \mathbf{u}_1, \dots, \mathbf{u}_{r-1}) \quad (2.56)$$

$$V^\dagger = (\mathbf{v}_0, \mathbf{v}_1, \dots, \mathbf{v}_{r-1}) \quad (2.57)$$

$$S = \begin{pmatrix} \sqrt{\lambda_0} & 0 & \cdots & 0 \\ 0 & \sqrt{\lambda_1} & \cdots & 0 \\ \vdots & \vdots & & \vdots \\ 0 & 0 & \cdots & \sqrt{\lambda_{r-1}} \end{pmatrix}. \quad (2.58)$$

Eq. (2.55) is the SVD of the matrix M . The diagonal matrix elements of S are called singular values. In general, $m \times r$ matrix U and $r \times n$ matrix V are not necessarily unitary matrices since $r \neq n, m$. However, they always satisfy the following relationships.

$$U^\dagger U = I_{r \times r}. \quad (2.59)$$

$$VV^\dagger = I_{r \times r}. \quad (2.60)$$

Schmidt decomposition

We can define the Schmidt decomposition of a state $|\psi\rangle$ using SVD. We divide the system

into A and B. Let each of the complete orthonormal bases be $|i\rangle_A$ and $|j\rangle_B$. $|\psi\rangle$ can be expanded as

$$|\psi\rangle = \sum_{i,j} c_{ij} |i\rangle_A |j\rangle_B. \quad (2.61)$$

The Coefficients c_{ij} can be regarded as a matrix, so that c_{ij} is decomposed by SVD as

$$c_{ij} = \sum_{\alpha=1}^{\chi} U_{i\alpha} \lambda_{\alpha} V_{\alpha j}. \quad (2.62)$$

Here we write the singular values as λ_{α} . Putting this decomposition into Eq. (2.61), one obtains

$$\begin{aligned} |\psi\rangle &= \sum_{i,j} \sum_{\alpha} U_{i\alpha} \lambda_{\alpha} V_{\alpha j} |i\rangle_A |j\rangle_B \\ &= \sum_{\alpha} \lambda_{\alpha} \left(\sum_i U_{i\alpha} |i\rangle_A \right) \left(\sum_j V_{\alpha j} |j\rangle_B \right) \\ &= \sum_{\alpha} \lambda_{\alpha} |\alpha\rangle_A |\alpha\rangle_B. \end{aligned} \quad (2.63)$$

This expression of the state $|\psi\rangle$ is called Schmidt decomposition. λ_{α} and $|\alpha\rangle_{A,B}$ are called Schmidt values and Schmidt vectors, respectively. Because of the conditions $U^\dagger U = I$ and $VV^\dagger = I$, Schmidt vectors and Schmidt values satisfy

$$\begin{aligned} \langle \alpha | \beta \rangle_A &= \sum_{i,j} U_{i\alpha}^* U_{j\beta} \langle i | j \rangle_A \\ &= \sum_i U_{i\alpha}^* U_{i\beta} \\ &= \delta_{\alpha,\beta}, \end{aligned} \quad (2.64)$$

$$\begin{aligned} \langle \alpha | \beta \rangle_B &= \sum_{i,j} V_{\alpha i}^* V_{\beta j} \langle i | j \rangle_B \\ &= \sum_i V_{\beta i}^* V_{\alpha i} \\ &= \delta_{\beta,\alpha}, \end{aligned} \quad (2.65)$$

$$\begin{aligned} 1 &= \langle \psi | \psi \rangle \\ &= \sum_{\alpha,\beta} \lambda_{\alpha} \lambda_{\beta} \langle \alpha | \beta \rangle_A \langle \alpha | \beta \rangle_B \\ &= \sum_{\alpha} \lambda_{\alpha}^2. \end{aligned} \quad (2.66)$$

The reduced density matrix ρ_A is written down as

$$\begin{aligned}\rho_A &= \text{Tr}_B [|\psi\rangle\langle\psi|] \\ &= \sum_{\alpha,\beta} \lambda_\alpha \lambda_\beta |\alpha\rangle_A \langle\beta|_A \text{Tr}_B [|\alpha\rangle_B \langle\beta|_B] \\ &= \sum_{\alpha} \lambda_\alpha^2 |\alpha\rangle_A \langle\alpha|_A.\end{aligned}\tag{2.67}$$

Therefore, the square of Schmidt values λ_α^2 and Schmidt vectors $|\alpha\rangle_A$ are the eigenvalues and eigenvectors of the reduced density matrix ρ_A . Similarly, $|\alpha\rangle_B$ are the eigenvectors of the reduced density matrix ρ_B . The entanglement entropy S_A is given by

$$S_A = -\text{Tr}_A(\rho_A \ln \rho_A) = -\sum_{\alpha} \lambda_\alpha^2 \ln(\lambda_\alpha^2).\tag{2.68}$$

Finally, we comment on the relation between the entanglement entropy and the number of Schmidt values χ . When $\chi = 1$, $|\psi\rangle$ is a product state of two states in each subsystem, and can be considered disentangled. In contrast, $\chi \geq 1$ means that the two subsystems, A and B, are entangled. If two subsystems are maximally entangled, $\lambda_\alpha = \frac{1}{\sqrt{\chi}}$ and $S_A = \ln(\chi)$. From this relation, we can roughly estimate the maximum required number of Schmidt values $\chi \sim e^{S_A}$. As explained later, we don't use all of the singular values but some of the larger ones when constructing MPS. The required number of singular values may depend on the system to be analyzed, but it can be as large as $\chi \sim e^{S_A}$. Therefore, the entanglement entropy of the system is important. In a one-dimensional lattice system, it is known [68] that the entanglement entropy of a ground state for a gapped, local Hamiltonian is

$$S_A \sim |\partial V|\tag{2.69}$$

where V is volume of the subsystem A , and $|\partial V|$ is the boundary area of the subsystem A . This relation is called the area law of entanglement entropy. The entanglement entropy of the ground states for a gapless and local Hamiltonian also satisfies

$$S_A \sim |\partial V| \ln |V|.\tag{2.70}$$

In a one-dimensional lattice system, the volume of the subsystem corresponds to the length of the chain L . Therefore, S_A and χ are estimated to be $S_A \sim \mathcal{O}(1)$ and $\chi \sim \mathcal{O}(1)$ in a gapped system, $S_A \sim c \ln L$ and $\chi \sim \mathcal{O}(L^c)$ in a gapless system. This is why one-dimensional systems have the advantage in expressing the states with MPS efficiently. In a higher dimensional system, the entanglement entropy of the ground state is proportional to at least the first power of L . The required number of Schmidt values increases exponentially, $\chi \sim e^L$.

2.2.2 Construction of MPS

We introduce MPS to express one-dimensional quantum systems efficiently. The Hilbert space of the entire system with N sites, each having local internal degrees of freedom d ,

has a dimension $D = d^N$. These internal degrees of freedom are represented by $\{|\sigma_j\rangle\}_{j=1}^N$, where $\sigma_j = 1, \dots, d$. A general quantum state $|\psi\rangle$ can be expressed as

$$|\psi\rangle = \sum_{\sigma_1, \dots, \sigma_N} c_{\sigma_1, \dots, \sigma_N} |\sigma_1 \dots, \sigma_N\rangle. \quad (2.71)$$

In order to construct MPS, we first regard $\sigma_2, \dots, \sigma_N$ as one index and perform SVD for the matrix $c_{\sigma_1, (\sigma_2, \dots, \sigma_N)}$,

$$c_{\sigma_1, (\sigma_2, \dots, \sigma_N)} = \sum_{\alpha_1=1}^{\chi_1} U_{\sigma_1 \alpha_1}^{[1]} \lambda_{\alpha_1}^{[1]} V_{\alpha_1 (\sigma_2, \dots, \sigma_N)}^{[1]} =: \sum_{\alpha_1=1}^{\chi_1} \Gamma_{\alpha_1}^{[1]\sigma_1} \lambda_{\alpha_1}^{[1]} V_{\alpha_1 (\sigma_2, \dots, \sigma_N)}^{[1]}. \quad (2.72)$$

Next we apply SVD to $V_{\alpha_1 (\sigma_2, \dots, \sigma_N)}^{[1]}$, and repeat this procedure until the end of system,

$$\begin{aligned} c_{\sigma_1, \sigma_2, \dots, \sigma_N} &= \sum_{\alpha_1, \alpha_2} \Gamma_{\alpha_1}^{[1]\sigma_1} \lambda_{\alpha_1}^{[1]} \Gamma_{\alpha_1, \alpha_2}^{[2]\sigma_2} \lambda_{\alpha_2}^{[2]} V_{\alpha_2 (\sigma_3, \dots, \sigma_N)}^{[2]} \\ &= \dots \\ &= \sum_{\alpha_1, \dots, \alpha_{N-1}} \Gamma_{\alpha_1}^{[1]\sigma_1} \lambda_{\alpha_1}^{[1]} \Gamma_{\alpha_1, \alpha_2}^{[2]\sigma_2} \lambda_{\alpha_2}^{[2]} \dots \lambda_{\alpha_{N-1}}^{[N-1]} V_{\alpha_{N-1} \sigma_N}^{[N-1]} \\ &= \sum_{\alpha_1, \dots, \alpha_{N-1}} \Gamma_{\alpha_1}^{[1]\sigma_1} \lambda_{\alpha_1}^{[1]} \Gamma_{\alpha_1, \alpha_2}^{[2]\sigma_2} \lambda_{\alpha_2}^{[2]} \dots \lambda_{\alpha_{N-1}}^{[N-1]} \Gamma_{\alpha_{N-1}}^{[N]\sigma_N}. \end{aligned} \quad (2.73)$$

By combining $\Gamma_{\alpha_{i-1}, \alpha_i}^{[i]\sigma_i}$ and $\lambda_{\alpha_i}^{[i]}$ into $A_{\alpha_{i-1}, \alpha_i}^{[i]\sigma_i} = \Gamma_{\alpha_{i-1}, \alpha_i}^{[i]\sigma_i} \lambda_{\alpha_i}^{[i]}$, the following simple expression can also be obtained.

$$c_{\sigma_1, \sigma_2, \dots, \sigma_N} = \sum_{\alpha_1, \dots, \alpha_{N-1}} A_{\alpha_1}^{[1]\sigma_1} A_{\alpha_1, \alpha_2}^{[2]\sigma_2} \dots A_{\alpha_{N-1}}^{[N]\sigma_N}. \quad (2.74)$$

Finally, we obtain MPS representation of $|\psi\rangle$,

$$\begin{aligned} |\psi\rangle &= \sum_{\sigma_1, \dots, \sigma_N} c_{\sigma_1, \dots, \sigma_N} |\sigma_1 \dots, \sigma_N\rangle \\ &= \sum_{\sigma_1, \dots, \sigma_N} \sum_{\alpha_1, \dots, \alpha_{N-1}} \Gamma_{\alpha_1}^{[1]\sigma_1} \lambda_{\alpha_1}^{[1]} \Gamma_{\alpha_1, \alpha_2}^{[2]\sigma_2} \lambda_{\alpha_2}^{[2]} \dots \lambda_{\alpha_{N-1}}^{[N-1]} \Gamma_{\alpha_{N-1}}^{[N]\sigma_N} |\sigma_1 \dots, \sigma_N\rangle \end{aligned} \quad (2.75)$$

$$= \sum_{\sigma_1, \dots, \sigma_N} \sum_{\alpha_1, \dots, \alpha_{N-1}} A_{\alpha_1}^{[1]\sigma_1} A_{\alpha_1, \alpha_2}^{[2]\sigma_2} \dots A_{\alpha_{N-1}}^{[N]\sigma_N} |\sigma_1 \dots, \sigma_N\rangle. \quad (2.76)$$

A diagrammatic representation of this construction of MPS is shown in Fig. 2.3. This MPS construction is related to Schmidt decomposition. To see this fact, we define new bases as

$$|\alpha_i^{[-]}\rangle = \sum_{\sigma_1, \dots, \sigma_i} \sum_{\alpha_1, \dots, \alpha_{i-1}} \Gamma_{\alpha_1}^{[1]\sigma_1} \dots \lambda_{\alpha_{i-1}}^{[i-1]} \Gamma_{\alpha_{i-1}, \alpha_i}^{[i]\sigma_i} |\sigma_1 \dots, \sigma_i\rangle, \quad (2.77)$$

$$|\alpha_i^{[+]}\rangle = \sum_{\sigma_{i+1}, \dots, \sigma_N} \sum_{\alpha_{i+1}, \dots, \alpha_{N-1}} \Gamma_{\alpha_i, \alpha_{i+1}}^{[i+1]\sigma_{i+1}} \dots \lambda_{\alpha_{N-1}}^{[N-1]} \Gamma_{\alpha_{N-1}}^{[N]\sigma_N} |\sigma_{i+1} \dots, \sigma_N\rangle. \quad (2.78)$$

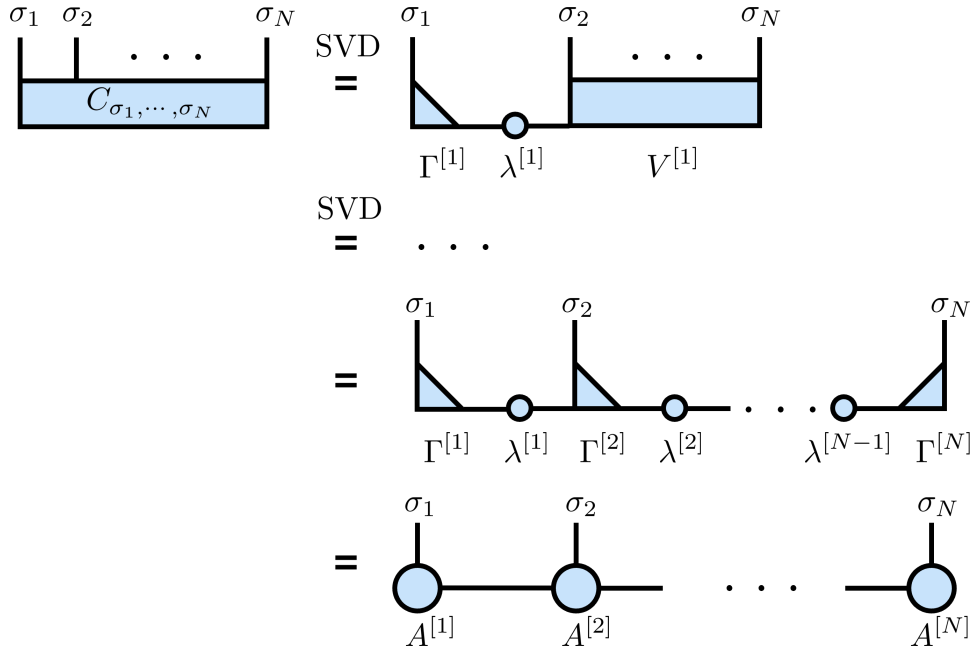


Figure 2.3: A diagrammatic representation of the construction of MPS for the coefficient of a general quantum state $|\psi\rangle = \sum_{\sigma_1, \dots, \sigma_N} c_{\sigma_1, \dots, \sigma_N} |\sigma_1 \dots, \sigma_N\rangle$.

From the properties of the SVD, $\left| \alpha_i^{[-]} \right\rangle$ and $\left| \alpha_i^{[+]} \right\rangle$ form orthonormal bases. $|\psi\rangle$ is rewritten by using these bases

$$|\psi\rangle = \sum_{\alpha_i}^{\chi_i} \lambda_{\alpha_i}^{[i]} |\alpha_i^{[\leftarrow]}\rangle |\alpha_i^{[\rightarrow]}\rangle. \quad (2.79)$$

This expression is Schmidt decomposition of $|\psi\rangle$ when the system A is ranging from site 1 to site i and the system B is ranging from site $i+1$ to site N . $\lambda_{\alpha_i}^{[i]}$ corresponds to Schmidt values. χ_i is called the bond dimension in the MPS expression, and corresponds to the number of Schmidt values.

2.2.3 Left and right canonical conditions

In the previous subsection, we constructed MPS for any state by performing SVD from the beginning of the chain. From Eq. (2.59) and Eq. (2.66), the matrix $A^{[i]}$ satisfies the left canonical condition $\sum_{\sigma_i, \alpha_{i-1}} A_{\alpha_{i-1}, \alpha_i}^{[i]\sigma_i*} A_{\alpha_{i-1}, \beta_i}^{[i]\sigma_i} = \delta_{\alpha_i, \beta_i}$. However, there is another way

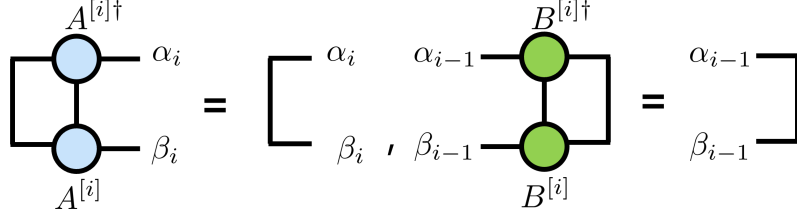


Figure 2.4: Left and right canonical conditions of $A^{[i]}$ matrices and $B^{[i]}$ matrices.

to construct MPS by performing SVD from the end of the chain,

$$\begin{aligned}
 c_{(\sigma_1, \dots, \sigma_{N-1}), \sigma_N} &= \sum_{\alpha_{N-1}=1}^{\chi_{N-1}} U_{(\sigma_1, \dots, \sigma_{N-1})\alpha_{N-1}}^{[N]} \lambda_{\alpha_{N-1}}^{[N]} V_{\alpha_{N-1}\sigma_N}^{[N]} \\
 &= \sum_{\alpha_{N-1}=1}^{\chi_{N-1}} U_{(\sigma_1, \dots, \sigma_{N-1})\alpha_{N-1}}^{[N]} \lambda_{\alpha_{N-1}}^{[N]} \Gamma_{\alpha_{N-1}}^{[N]\sigma_N} \\
 &= \sum_{\alpha_{N-1}=1}^{\chi_{N-1}} U_{(\sigma_1, \dots, \sigma_{N-1})\alpha_{N-1}}^{[N]} B_{\alpha_{N-1}}^{[N]\sigma_N}.
 \end{aligned} \tag{2.80}$$

Repeating SVD toward the beginning of the chain, we can obtain another MPS form,

$$c_{\sigma_1, \sigma_2, \dots, \sigma_N} = \sum_{\alpha_1, \dots, \alpha_{N-1}} B_{\alpha_1}^{[1]\sigma_1} B_{\alpha_1, \alpha_2}^{[2]\sigma_2} \cdots B_{\alpha_{N-1}}^{[N]\sigma_N}. \tag{2.81}$$

From Eq. (2.60) and Eq. (2.66), the matrix $B^{[i]}$ satisfies the right canonical condition, $\sum_{\sigma_i, \alpha_i} B_{\alpha_{i-1}, \alpha_i}^{[i]\sigma_i} B_{\beta_{i-1}, \alpha_i}^{[i]\sigma_i*} = \delta_{\alpha_{i-1}, \beta_{i-1}}$. The left and right canonical conditions are shown in Fig. 2.4. We can also mix the decomposition of the state from the beginning to the site i and from the end to the site $i+1$,

$$\begin{aligned}
 c_{\sigma_1, \sigma_2, \dots, \sigma_N} &= \sum_{\alpha_1, \dots, \alpha_{N-1}} A_{\alpha_1}^{[1]\sigma_1} \cdots A_{\alpha_{i-1}, \alpha_i}^{[i]\sigma_i} \lambda_{\alpha_i} V_{\alpha_i, (\sigma_{i+1}, \dots, \sigma_N)} \\
 &= \sum_{\alpha_1, \dots, \alpha_{N-1}} A_{\alpha_1}^{[1]\sigma_1} \cdots A_{\alpha_{i-1}, \alpha_i}^{[i]\sigma_i} \lambda_{\alpha_i} B_{\alpha_i, \alpha_{i+1}}^{[i+1]\sigma_{i+1}} \cdots B_{\alpha_{N-1}}^{[N]\sigma_N}
 \end{aligned} \tag{2.82}$$

$$= \sum_{\alpha_1, \dots, \alpha_{N-1}} A_{\alpha_1}^{[1]\sigma_1} \cdots A_{\alpha_{i-2}, \alpha_{i-1}}^{[i-1]\sigma_{i-1}} M_{\alpha_{i-1}, \alpha_i}^{[i]\sigma_i} B_{\alpha_i, \alpha_{i+1}}^{[i+1]\sigma_{i+1}} \cdots B_{\alpha_{N-1}}^{[N]\sigma_N}, \tag{2.83}$$

where we define $M_{\alpha_{i-1}, \alpha_i}^{[i]\sigma_i} = A_{\alpha_{i-1}, \alpha_i}^{[i]\sigma_i} \lambda_{\alpha_i}$. This is called the mixed canonical form. $A^{[i]}$ matrices and $B^{[j]}$ matrices satisfy the left and right canonical conditions, respectively. In the following, the notations $A^{[i]}$ and $B^{[j]}$ are used for the left and right canonical forms. When the canonical conditions are not of concern, matrices will be denoted by symbols like $M^{[i]}$.

2.3 Density matrix renormalization group method

The DMRG method is used to simulate the ground state of one-dimensional strongly correlated quantum lattice systems, which is hard to solve analytically and numerically,

except for exactly solvable models. In 1992, Steve White invented the DMRG method [52, 53], which is now one of the most powerful numerical method in the study of one-dimensional quantum lattices. For the numerical implementation of the DMRG algorithm (and the TEBD algorithm), we use the ITensor library [69]. In this section, we review the DMRG method based on [70].

2.3.1 Matrix Product Operator

Analogously to the MPS, we can also express operators as Matrix Product Operators (MPO). A general operator can be expressed as

$$\hat{O} = \sum_{\sigma_1, \dots, \sigma_N} \sum_{\sigma'_1, \dots, \sigma'_N} O_{(\sigma_1, \dots, \sigma_N), (\sigma'_1, \dots, \sigma'_N)} |\sigma_1, \dots, \sigma_N\rangle \langle \sigma'_1, \dots, \sigma'_N|. \quad (2.84)$$

When we regard the coefficient $O_{(\sigma_1, \dots, \sigma_N), (\sigma'_1, \dots, \sigma'_N)}$ as $O_{(\sigma_1 \sigma'_1), \dots, (\sigma_N \sigma'_N)}$, we can decompose it in a similar way as we did for an MPS, with the double indices (σ_i, σ'_i) taking the role of the index σ_i in an MPS, i.e. :

$$O_{(\sigma_1 \sigma'_1), \dots, (\sigma_N \sigma'_N)} = W[1]^{\sigma_1, \sigma'_1} W[2]^{\sigma_2, \sigma'_2} \dots W[N]^{\sigma_N, \sigma'_N}. \quad (2.85)$$

This simplified form of the MPO is useful when we calculate the expectation value of the operator \hat{O} in terms of $|\psi\rangle$. In order to obtain the expectation value, we have to apply \hat{O} to $|\psi\rangle$. The application of a matrix product operator to a matrix product state runs as

$$\begin{aligned} \hat{O} |\psi\rangle &= \sum_{\sigma, \sigma'} \left(W[1]^{\sigma_1, \sigma'_1} \dots W[N]^{\sigma_N, \sigma'_N} \right) \left(M^{[1]\sigma''_1} \dots M^{[N]\sigma''_N} \right) |\sigma\rangle \langle \sigma' | \sigma'' \rangle \\ &= \sum_{\sigma, \sigma'} \sum_{\beta, \alpha} \left(W[1]_{\beta_1}^{\sigma_1, \sigma'_1} M_{\alpha_1}^{[1]\sigma'_1} \right) \dots \left(W[N]_{\beta_{N-1}}^{\sigma_N, \sigma'_N} M_{\alpha_{N-1}}^{[N]\sigma'_N} \right) |\sigma\rangle \\ &= \sum_{\sigma} N^{[1]\sigma_1} \dots N^{[N]\sigma_N} |\sigma\rangle, \end{aligned} \quad (2.86)$$

where

$$N_{(\beta_{i-1}, \alpha_{i-1}), (\beta_i, \alpha_i)}^{[i]\sigma_i} = \sum_{\sigma'} W[i]_{\beta_{i-1}, \beta_i}^{\sigma_i, \sigma'_i} M_{\alpha_{i-1}, \alpha_i}^{[i]\sigma'_i}. \quad (2.87)$$

Then, we can calculate the expectation value of the operator \hat{O} as

$$\begin{aligned} \langle \psi | \hat{O} | \psi \rangle &= \sum_{\sigma, \sigma'} \langle \sigma' | \sigma \rangle M^{[N]\sigma'_N \dagger} \dots M^{[1]\sigma'_1 \dagger} N^{[1]\sigma_1} \dots N^{[N]\sigma_N} \\ &= \sum_{\sigma_N} M^{[N]\sigma'_N \dagger} \left(\dots \left(\sum_{\sigma_1} M^{[1]\sigma'_1 \dagger} N^{[1]\sigma_1} \right) \dots \right) N^{[N]\sigma_N}. \end{aligned} \quad (2.88)$$

The schematic representation of the calculation is shown in Fig. 2.5.

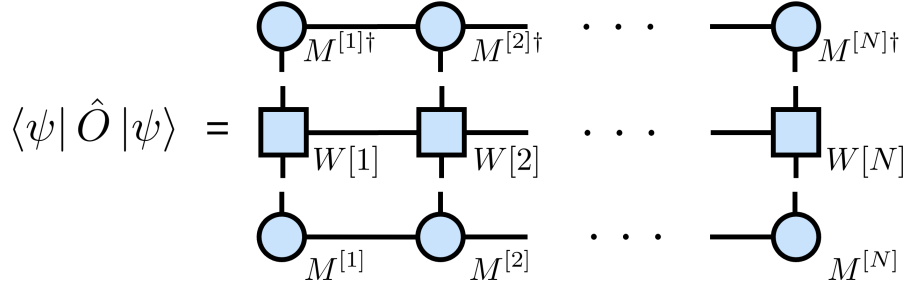


Figure 2.5: A schematic picture of the expectation value of the operator \hat{O} in terms of $|\psi\rangle$ calculated by MPO and MPS.

2.3.2 Variational ground state search

Here, we review the variational ground state search for MPS. In order to find the optimal approximation to the ground state, we use the variational principle. We have to find $|\psi\rangle$ that minimizes

$$E = \frac{\langle\psi|\hat{H}|\psi\rangle}{\langle\psi|\psi\rangle} \quad (2.89)$$

We can reformulate this problem into a Lagrange-multiplier problem, which minimizes $\langle\psi|\hat{H}|\psi\rangle$ under the condition $\langle\psi|\psi\rangle = 1$. Therefore, the Lagrange function L we have to minimize is

$$L = \langle\psi|\hat{H}|\psi\rangle - E(\langle\psi|\psi\rangle - 1). \quad (2.90)$$

There are some ways to minimize this function. One way is to choose a trial wavefunction with parameters and then minimize L with respect to these parameters. In the DMRG algorithm, we use one of the MPS matrices as a variational parameter. The idea is not to optimize all matrices at once, but just optimize one matrix at site i in the MPS and then move to the next matrix and repeat the same procedure. In order to see this, we first show the compact form of the $\langle\psi|\psi\rangle$ and $\langle\psi|\hat{H}|\psi\rangle$ focusing on a matrix at site i . Let $|\psi\rangle$

be expressed as a mixed canonical form,

$$\begin{aligned}
 \langle\psi|\psi\rangle &= \sum_{\sigma,\sigma'} \underbrace{\langle\sigma|\sigma'\rangle}_{\delta_{\sigma,\sigma'}} B^{[N]\sigma_N\dagger} \dots B^{[i+1]\sigma_{i+1}\dagger} M^{[i]\sigma_i\dagger} \\
 &\quad \underbrace{A^{[i-1]\sigma_{i-1}\dagger} \dots A^{[1]\sigma_1\dagger}}_I A^{[1]\sigma'_1} \dots A^{[i-1]\sigma'_{i-1}} M^{[i]\sigma'_i} B^{[i+1]\sigma'_{i+1}} \dots B^{[N]\sigma'_N} \\
 &= \sum_{\sigma,\alpha_i} \left(M^{[i]\sigma_i\dagger} M^{[i]\sigma_i} \underbrace{B^{[i+1]\sigma_{i+1}} \dots B^{[N]\sigma_N} B^{[N]\sigma_N\dagger} \dots B^{[i+1]\sigma_{i+1}\dagger}}_I \right)_{\alpha_i,\alpha_i} \\
 &= \sum_{\sigma_i} \sum_{\alpha_{i-1},\alpha_i} (M_{\alpha_{i-1},\alpha_i}^{[i]\sigma_i*} M_{\alpha_{i-1},\alpha_i}^{[i]\sigma_i}),
 \end{aligned} \tag{2.91}$$

$$\begin{aligned}
 \langle\psi|\hat{H}|\psi\rangle &= \sum_{\sigma,\sigma'} \sum_{\tilde{\sigma},\tilde{\sigma}'} B^{[N],\sigma_N\dagger} \dots A^{[1]\sigma_1\dagger} \underbrace{\langle\sigma|\tilde{\sigma}\rangle}_{\delta_{\sigma,\tilde{\sigma}}} W[1]^{\tilde{\sigma}_1,\tilde{\sigma}'_1} \dots W[N]^{\tilde{\sigma}_N,\tilde{\sigma}'_N} \\
 &\quad \underbrace{\langle\tilde{\sigma}'|\sigma'\rangle}_{\delta_{\tilde{\sigma}'},\sigma'} A^{[1]\sigma'_1\dagger} \dots B^{[N],\sigma_N\dagger'} \\
 &= \sum_{\alpha_i,\alpha'_{i-1},\beta_{i-1}} L_{\alpha'_{i-1},\beta_{i-1}}^{\alpha_{i-1}} \left(\sum_{\sigma_i,\sigma'_i} M_{\alpha_{i-1},\alpha_i}^{[i]\sigma_i*} W[i]_{\beta_{i-1},\beta_i}^{\sigma_i,\sigma'_i} M_{\alpha'_{i-1},\alpha'_i}^{[i]\sigma'_i} \right) R_{\alpha'_i,\beta_i}^{\alpha_i}, \tag{2.92}
 \end{aligned}$$

where

$$\begin{aligned}
 L_{\alpha'_{i-1},\beta_{i-1}}^{[i-1]\alpha_{i-1}} &= \sum_{\alpha,\alpha',\beta} \sum_{\sigma,\sigma'} \left(A_{\alpha_1}^{[1]\sigma_1*} W[1]_{\beta_1}^{\sigma_1,\sigma'_1} A_{\alpha'_1}^{[1]\sigma'_1} \right) \dots \\
 &\quad \left(A_{\alpha_{i-2},\alpha_{i-1}}^{[i-1]\sigma_{i-1}*} W[i-1]_{\beta_{i-2},\beta_{i-1}}^{\sigma_{i-1},\sigma'_{i-1}} A_{\alpha'_{i-2},\alpha'_{i-1}}^{[i-1]\sigma'_{i-1}} \right), \tag{2.93}
 \end{aligned}$$

$$\begin{aligned}
 R_{\alpha'_i,\beta_i}^{[i+1]\alpha_i} &= \sum_{\alpha,\alpha',\beta} \sum_{\sigma,\sigma'} \left(B_{\alpha_i,\alpha_{i+1}}^{[i+1]\sigma_{i+1}*} W[i+1]_{\beta_i,\beta_{i+1}}^{\sigma_{i+1},\sigma'_{i+1}} B_{\alpha'_i,\alpha'_{i+1}}^{[i+1]\sigma'_{i+1}} \right) \dots \\
 &\quad \left(B_{\alpha_N}^{[N]\sigma_N*} W[N]_{\beta_N}^{\sigma_N,\sigma'_N} B_{\alpha'_N}^{[N]\sigma'_N} \right). \tag{2.94}
 \end{aligned}$$

Now, we use the variational principle. We differentiate the Lagrange function with respect to $M_{\alpha_{i-1},\alpha_i}^{[i]\sigma_i*}$, and set these differentiations to zero :

$$\begin{aligned}
 0 &= \frac{\partial L}{\partial M_{\alpha_{i-1},\alpha_i}^{[i]\sigma_i*}} \\
 &= \frac{\partial \langle\psi|\hat{H}|\psi\rangle}{\partial M_{\alpha_{i-1},\alpha_i}^{[i]\sigma_i*}} - E \frac{\partial \langle\psi|\psi\rangle}{\partial M_{\alpha_{i-1},\alpha_i}^{[i]\sigma_i*}} \\
 &= \sum_{\alpha'_i,\beta_i} \sum_{\alpha'_{i-1},\beta_{i-1}} \sum_{\sigma'_i} L_{\alpha'_{i-1},\beta_{i-1}}^{[i-1]\alpha_{i-1}} W[i]_{\beta_{i-1},\beta_i}^{\sigma_i,\sigma'_i} M_{\alpha'_{i-1},\alpha'_i}^{[i]\sigma'_i} R_{\alpha'_i,\beta_i}^{[i+1]\alpha_i} - EM_{\alpha_{i-1},\alpha_i}^{[i]\sigma_i}. \tag{2.95}
 \end{aligned}$$

This equation is regarded as an eigenvalue equation if we set

$$P_{(\sigma_i,\alpha_{i-1},\alpha_i),(\sigma'_i,\alpha'_{i-1},\alpha'_i)} = \sum_{\beta_{i-1},\beta_i} L_{\alpha'_{i-1},\beta_{i-1}}^{[i-1]\alpha_{i-1}} W[i]_{\beta_{i-1},\beta_i}^{\sigma_i,\sigma'_i} R_{\alpha'_i,\beta_i}^{[i+1]\alpha_i} \tag{2.96}$$

$$\nu_{\sigma_i,\alpha_{i-1},\alpha_i} = M_{\alpha_{i-1},\alpha_i}^{[i]\sigma_i}. \tag{2.97}$$

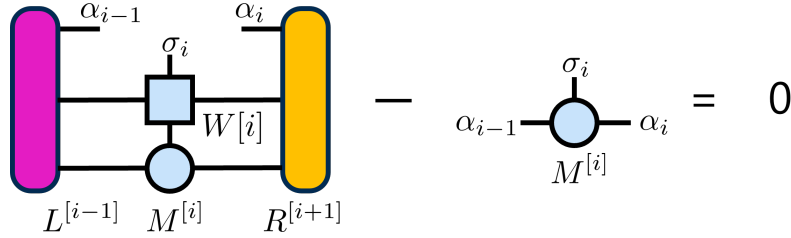


Figure 2.6: Eigenvalue equation to optimize the Matrix $M^{[i]}$.

Then, the eigenvalue equation we have to solve is

$$P\nu - E\nu = 0. \quad (2.98)$$

A diagrammatic representation of this equation is shown in Fig. 2.6. In general, the size of the P matrix with the bond dimension χ is $d\chi^2$. This is too large to perform an exact diagonalization. However, as we are only interested in the lowest eigenvalue and the corresponding eigenvector, an iterative eigensolver such as the Krylov subspace method can be used. Then, we can obtain the optimized matrices $M_{\alpha_{i-1}, \alpha_i}^{[i]\sigma_i}$ and the lowest eigenvalue E . In order to optimize a given starting state $|\psi\rangle$ iteratively to represent the ground state, we will proceed as follows :

- (i) Start from a certain random MPS which is in the right canonical form, i.e. :

$$M^{[1]\sigma_1} B^{[2]\sigma_2} \dots B^{[N]\sigma_N}.$$

We also express the Hamiltonian in the form of MPO.

- (ii) Calculate all of the $R^{[i]}$ -matrices iteratively.
- (iii) Start from site $i = 1$. We update the matrix $M^{[i]}$ by solving the eigenvalue problem $M^{[i]\sigma_i} \rightarrow \tilde{M}^{[i]\sigma_i}$. Once the solution is obtained, we left-normalize $\tilde{M}^{[i]}$ into $A^{[i]}$ by SVD, i.e. :

$$\begin{aligned} & A^{[1]\sigma_1} \dots A^{[i-1]\sigma_{i-1}} M^{[i]\sigma_i} B^{[i+1]\sigma_{i+1}} \dots B^{[N]\sigma_N} \\ \rightarrow & A^{[1]\sigma_1} \dots A^{[i-1]\sigma_{i-1}} \tilde{M}^{[i]\sigma_i} B^{[i+1]\sigma_{i+1}} \dots B^{[N]\sigma_N} \\ \xrightarrow{\text{SVD}} & A^{[1]\sigma_1} \dots A^{[i-1]\sigma_{i-1}} \underbrace{U}_{A^{[i]\sigma_i}} \underbrace{S V B^{[i+1]\sigma_{i+1}} \dots B^{[N]\sigma_N}}_{M^{[i+1]\sigma_{i+1}}} \\ \rightarrow & A^{[1]\sigma_1} \dots A^{[i]\sigma_i} M^{[i+1]\sigma_{i+1}} B^{[i+2]\sigma_{i+2}} \dots B^{[N]\sigma_N} \end{aligned}$$

In this procedure, we calculate the $L^{[i]}$ -matrices iteratively.

- (iv) Repeat the procedure above until we have reached $i = N$. The MPS is now in the left canonical form, i.e. :

$$A^{[1]\sigma_1} \dots A^{[N-1]\sigma_{N-1}} \dots M^{[N]\sigma_N}$$

- (v) Similarly, perform the procedure from the end of the chain $i = N$ to the beginning of the chain $i = 1$. This gives the right canonical form. This is one step of the iterative process. The procedure continues until the convergence is achieved. The convergence is checked by calculating the energy difference ϵ between the previous and current steps. In this study, we keep $\epsilon < 10^{-7}$.

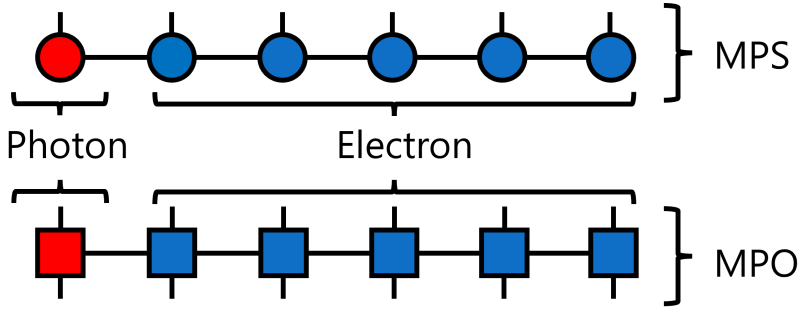


Figure 2.7: MPS and MPO representation of the cavity-matter system. The cavity single photon site is placed at the beginning of the chain. The electron is placed at the rest of the chain.

2.3.3 DMRG method for the cavity-matter systems

Here, we explain the DMRG method for cavity-matter systems. There are several challenges to simulate such a system using the DMRG method.

The first difficulty is the configuration of MPS and MPO. The DMRG method is suited to calculate the ground state of one-dimensional quantum lattice systems, where MPS and MPO are arranged along the one-dimensional axis. This technique is also applied to cavity-matter systems in the previous work [71–73], where the cavity single photon site is placed at one end of the MPS chain, while the rest of the MPS chain consists of matter degrees of freedom. Following the previous research, we calculate the ground state using the same MPS configuration. The specific expression of the MPS is shown in Fig. 2.7.

The second difficulty arises due to the infinite local physical dimension of the Hilbert space of the cavity field. The basis of the cavity field is spanned by the photon number basis (Fock basis). The dimension of the Hilbert space for photons, which are bosons, is infinite. However, a finite cutoff N_{\max} is introduced for a computational purpose. It is expected that states with small photon numbers are more relevant in the low-energy states because states with larger photon numbers have energies higher by Ω . Therefore, truncating Hilbert space for photons corresponds to discarding the higher-energy components.

We can also comment on the non-linear nature of the Peierls phase. Calculating the matrix elements of the quantized Peierls phase on the Fock basis is performed, focusing on the relation between Peierls phase and displacement operator $\hat{D}(\alpha) = e^{\alpha\hat{a}-\alpha^*\hat{a}^\dagger}$,

$$\exp\left(i\frac{G}{\sqrt{N}}(\hat{a} + \hat{a}^\dagger)\right) = \hat{D}\left(i\frac{G}{\sqrt{N}}\right). \quad (2.99)$$

The exact matrix elements in the Fock basis of the displacement operator are [74]

$$\langle n | \hat{D}(\alpha) | m \rangle = \sqrt{\frac{n!}{m!}} \alpha^{m-n} \exp\left(-\frac{|\alpha|^2}{2}\right) L_n^{m-n}(|\alpha|^2), \quad (2.100)$$

where $L_n^{m-n}(x)$ is the generalized Laguerre polynomial.

2.4 Time Evolving Block Decimation method

In this section, we review the TEBD method [55], which is a real and imaginary time evolution method of MPS. In this study, we obtain a ground-state MPS using the DMRG method, and then calculate the real-time evolution of the MPS using the TEBD.

2.4.1 Suzuki-Trotter decomposition

A state after an infinitesimal time is given by

$$|\psi(t + \delta t)\rangle = \hat{U}(t, \delta t) |\psi(t)\rangle, \quad (2.101)$$

$$\hat{U}(t, \delta t) = e^{-iH(t)\delta t}. \quad (2.102)$$

It is difficult to apply the time evolution operator $\hat{U}(t, \delta t)$ to an MPS directly because it acts globally on the MPS. However, Suzuki-Trotter decomposition [75] changes the time evolution operator into a product of local operators. We consider the time evolution operator which has the form of $e^{i(\hat{H}_1 + \hat{H}_2)\delta t}$. The operator \hat{H}_1 and \hat{H}_2 are not mutually-commuting. Suzuki-Trotter decompositions of the first and second orders are written as

$$e^{-i(\hat{H}_1 + \hat{H}_2)\delta t} = e^{-i\hat{H}_1\delta t} e^{-i\hat{H}_2\delta t} + \mathcal{O}(\delta t^2), \quad (2.103)$$

$$e^{-i(\hat{H}_1 + \hat{H}_2)\delta t} = e^{-i\hat{H}_1\delta t/2} e^{-i\hat{H}_2\delta t} e^{-i\hat{H}_1\delta t/2} + \mathcal{O}(\delta t^3). \quad (2.104)$$

Each factored exponential is known as a Trotter gate. This decomposition can be generalized to more complicated divisions of the full Hamiltonian \hat{H} into N parts, $\hat{H}_1, \hat{H}_2, \dots, \hat{H}_N$, i.e. :

$$\hat{H} = \sum_{\alpha=1}^N \hat{H}_\alpha. \quad (2.105)$$

The first and second orders of the TEBD time evolution operator can then be written as

$$\begin{aligned} e^{-i\hat{H}\delta t} &= e^{-i\hat{H}_1\delta t} e^{-i\hat{H}_2\delta t} \dots e^{-i\hat{H}_N\delta t} + \mathcal{O}(\delta t^2) \\ &= \prod_{\alpha=1}^N e^{-i\hat{H}_\alpha\delta t} + \mathcal{O}(\delta t^2), \end{aligned} \quad (2.106)$$

$$\begin{aligned} e^{-i\hat{H}\delta t} &= e^{-i\hat{H}_1\delta t/2} \dots e^{-i\hat{H}_{N-1}\delta t/2} e^{-i\hat{H}_N\delta t} e^{-i\hat{H}_{N-1}\delta t/2} \dots e^{-i\hat{H}_1\delta t/2} + \mathcal{O}(\delta t^3) \\ &= \prod_{\alpha=1}^N e^{-i\hat{H}_\alpha\delta t/2} \prod_{\alpha=N}^1 e^{-i\hat{H}_\alpha\delta t/2} + \mathcal{O}(\delta t^3). \end{aligned} \quad (2.107)$$

If we devide the Hamiltonian into local Hamiltonians which act locally, $e^{-i\hat{H}_\alpha \delta t/2}$ is a local gate. For example, the N -site 1DEHM is devided into two-site Hamiltonians such as

$$\hat{H}_{\text{EHM}} = \sum_{i=1}^{N-1} \hat{H}_{i,i+1}, \quad (2.108)$$

$$\begin{aligned} \hat{H}_{i,i+1} &= -W \sum_{\sigma} (\hat{c}_{i,\sigma}^\dagger \hat{c}_{i+1,\sigma} + \hat{c}_{i+1,\sigma}^\dagger \hat{c}_{i,\sigma}) + V \hat{n}_i \hat{n}_{i+1} \\ &\quad + \frac{U}{2} \hat{n}_{i,\uparrow} \hat{n}_{i,\downarrow} + \frac{U}{2} \hat{n}_{i+1,\uparrow} \hat{n}_{i+1,\downarrow} \quad (i = 2, 3, \dots, N-2), \end{aligned} \quad (2.109)$$

$$\begin{aligned} \hat{H}_{1,2} &= -W \sum_{\sigma} (\hat{c}_{1,\sigma}^\dagger \hat{c}_{2,\sigma} + \hat{c}_{2,\sigma}^\dagger \hat{c}_{1,\sigma}) + V \hat{n}_1 \hat{n}_2 \\ &\quad + U \hat{n}_{1,\uparrow} \hat{n}_{1,\downarrow} + \frac{U}{2} \hat{n}_{2,\uparrow} \hat{n}_{2,\downarrow}, \end{aligned} \quad (2.110)$$

$$\begin{aligned} \hat{H}_{N-1,N} &= -W \sum_{\sigma} (\hat{c}_{N-1,\sigma}^\dagger \hat{c}_{N,\sigma} + \hat{c}_{N,\sigma}^\dagger \hat{c}_{N-1,\sigma}) + V \hat{n}_{N-1} \hat{n}_N \\ &\quad + \frac{U}{2} \hat{n}_{N-1,\uparrow} \hat{n}_{N-1,\downarrow} + U \hat{n}_{N,\uparrow} \hat{n}_{N,\downarrow}. \end{aligned} \quad (2.111)$$

In this study, we use the second order Suzuki-Trotter decomposition to calculate the time evolution.

2.4.2 Updating MPS after the action of local operators

In this subsection, we explain how to update MPS after applying the gate. Here, we consider the action of a two-site gate decomposed by Suzuki-Trotter decomposition. Let \hat{U} be two-site gate acting on sites i and $i+1$,

$$\hat{U} = \sum_{\sigma_i, \sigma_{i+1}, \sigma'_i, \sigma'_{i+1}} U_{\sigma'_i, \sigma'_{i+1}}^{\sigma_i, \sigma_{i+1}} |\sigma_i, \sigma_{i+1}\rangle \langle \sigma'_i, \sigma'_{i+1}|. \quad (2.112)$$

MPS for $\hat{U}|\psi\rangle$ is obtained by redefining the tensors $M^{[i]}, M^{[i+1]}$. To do this, we use SVD for a rank-2 tensor $\Theta_{(\alpha_{i-1}, \sigma_i), (\sigma_{i+1}, \alpha_{i+1})}$ defined by

$$\sum_{\sigma'_i, \sigma'_{i+1}, \alpha_i} (M_{\alpha_{i-1}, \alpha_i}^{[i]\sigma'_i} M_{\alpha_i, \alpha_{i+1}}^{[i+1]\sigma'_{i+1}}) U_{\sigma'_i, \sigma'_{i+1}}^{\sigma_i, \sigma_{i+1}} =: \Theta_{(\alpha_{i-1}, \sigma_i), (\sigma_{i+1}, \alpha_{i+1})} \quad (2.113)$$

$$\begin{aligned} &\stackrel{\text{SVD}}{=} \sum_{\beta} U_{(\alpha_{i-1}, \sigma_i)\beta} \tilde{\lambda}_{\beta}^{[i]} V_{\beta(\sigma_{i+1}, \alpha_{i+1})} \\ &= \sum_{\beta} \tilde{M}_{\alpha_{i-1}, \beta}^{[i]\sigma_i} \tilde{M}_{\beta, \alpha_{i+1}}^{[i+1]\sigma_{i+1}}, \end{aligned} \quad (2.114)$$

where

$$\tilde{M}_{\alpha_{i-1}, \beta}^{[i]\sigma_i} = U_{(\alpha_{i-1}, \sigma_i)\beta} \tilde{\lambda}_{\beta}^{[i]}, \quad (2.115)$$

$$\tilde{M}_{\beta, \alpha_{i+1}}^{[i+1]\sigma_{i+1}} = V_{\beta(\sigma_{i+1}, \alpha_{i+1})}. \quad (2.116)$$

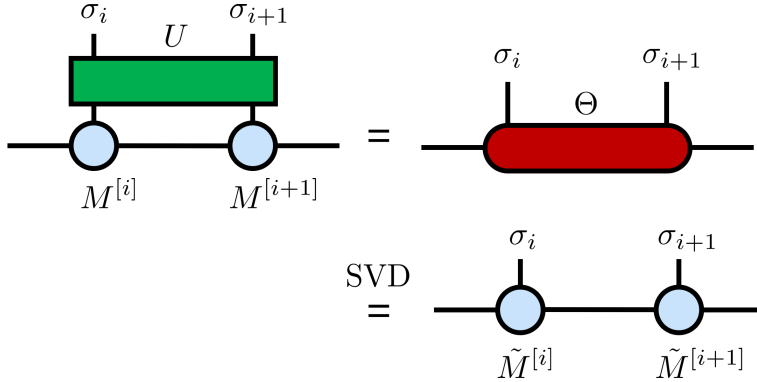


Figure 2.8: Update of MPS after applying a Trotter gate \hat{U} .

These procedures to update MPS are shown in Fig. 2.8. Note that the bond dimension needed in this operation increases, such as $\chi \rightarrow d\chi$. It is difficult to avoid the increase of the bond dimension because the computational cost of SVD for a $d\chi \times d\chi$ matrix is $\mathcal{O}((d\chi)^3)$. In the actual calculation, we only use larger χ_{\max} singular values among those obtained to prevent the bond dimension from increasing. This operation extracts only the significant singular values, providing an optimal approximation in a finite bond dimension χ_{\max} . From the perspective of the Schmidt decomposition, this corresponds to an approximation that retains the essential part of the contribution to the entanglement entropy. Due to the truncation of singular values, we have to recover the normalization condition Eq. (2.66) of a state by modifying Schmidt values as

$$\lambda_{\beta}^{[i]} : = \frac{\tilde{\lambda}_{\beta}^{[i]}}{\sqrt{N_{\text{norm}}}}, \quad (2.117)$$

$$N_{\text{norm}} = \sum_{\beta=1}^{\chi_{\max}} (\tilde{\lambda}_{\beta}^{[i]})^2. \quad (2.118)$$

This newly defined $\lambda_{\beta}^{[i]}$ satisfies the normalization condition $\langle \psi | \psi \rangle = \sum_{\beta=1}^{\chi_{\max}} (\lambda_{\beta}^{[i]})^2 = 1$.

2.4.3 TEBD method for cavity-matter systems

In this subsection, we explain the TEBD method for cavity-matter systems. In addition to the challenges explained in the context of the DMRG method for the cavity-matter systems, the TEBD method encounters another challenge.

This challenge comes from the global coupling of the cavity to electrons. The TEBD method explained above is based on the locally interacting Hamiltonian, so it is impossible to apply the process directly. The swap gate is the key to connecting the TEBD method and the simulation of the global coupled systems. Long-range terms in the Hamiltonian can be treated by introducing swap gates to exponentiate each contribution [76–78]. The swap gate allows one to change the order of the sites as needed. In recent years, the cavity-matter systems have also been simulated by the TEBD method with the swap gates [79–82]. In the following, we describe our procedure to perform the TEBD method

with the swap gates. First, we divide the cavity-matter Hamiltonian into the sum of the three site terms: photon site p , site i , and site $i + 1$.

$$\hat{H} = \sum_{i=1}^{N-1} \hat{H}_{p,i,i+1}, \quad (2.119)$$

$$\begin{aligned} \hat{H}_{p,i,i+1} &= \frac{\Omega}{N-1} \hat{a}^\dagger \hat{a} + \hat{H}_{i,i+1} \\ &\quad - W(e^{i\frac{G}{\sqrt{N}}(\hat{a}+\hat{a}^\dagger)} \hat{c}_{i,\sigma}^\dagger \hat{c}_{i+1,\sigma} + \text{h.c.}) \end{aligned} \quad (2.120)$$

$\hat{H}_{i,i+1}$ is the local two-site Hamiltonian of the Coulomb interaction part such as Eq. (2.108). Suzuki-Trotter decomposition of the time-evolution operator is written as

$$e^{-i\hat{H}\delta t} = \prod_{j=1}^{N-1} e^{-i\hat{H}_{p,j,j+1}\delta t/2} \prod_{j=N-1}^1 e^{-i\hat{H}_{p,j,j+1}\delta t/2} + \mathcal{O}(\delta t^3) \quad (2.121)$$

This means that we must apply the three-site operators where the three sites are not neighboring in the initial MPS representation. In order to solve this problem, we change the structure of the MPS while applying the time-evolution gates such that three sites are neighboring. This approach is implemented using the swap gates. The action of the swap gates results in the swapping of the physical indices of two neighboring MPS matrices. Let \hat{S} be an operator that swaps the photon site p and electron site i . The swap gates are constructed from two Kronecker δ functions as

$$\begin{aligned} \hat{S} &= \sum_{\sigma_p, \sigma_i, \sigma'_p, \sigma'_i} S_{\sigma'_p, \sigma'_i}^{\sigma_i, \sigma_p} |\sigma_p, \sigma_i\rangle \langle \sigma'_p, \sigma'_i| \\ &= \sum_{\sigma_p, \sigma_i, \sigma'_p, \sigma'_i} \delta_{\sigma_p, \sigma'_i} \delta_{\sigma_i, \sigma'_p} |\sigma_p, \sigma_i\rangle \langle \sigma'_p, \sigma'_i|. \end{aligned} \quad (2.122)$$

The application of the swap gates onto the MPS results in a rank-2 tensor $\Theta_{(\alpha_p, \sigma_i), (\sigma_p, \alpha_i)}$ such as Eq. (2.113). However, the subtle difference is that the physical indices σ_p and σ_i are swapped. An SVD of $\Theta_{(\alpha_p, \sigma_i), (\sigma_p, \alpha_i)}$ is performed to restore the MPS structure, and then the final form of the MPS is the form of the swapped one, i.e. :

$$\begin{aligned} &\sum_{\sigma'_p, \sigma'_i} S_{\sigma'_p, \sigma'_i}^{\sigma_i, \sigma_p} (M^{[1]\sigma_1} \dots M^{[p]\sigma'_p} M^{[i]\sigma'_i} \dots M^{[N],\sigma_N}) \\ &= M^{[1]\sigma_1} \dots \sum_{\sigma'_p, \sigma'_i} \delta_{\sigma_p, \sigma'_i} \delta_{\sigma_i, \sigma'_p} (M^{[p]\sigma'_p} M^{[i]\sigma'_i}) \dots M^{[N],\sigma_N} \\ &= M^{[1]\sigma_1} \dots \Theta^{\sigma_i, \sigma_p} \dots M^{[N],\sigma_N} \\ &\stackrel{\text{SVD}}{=} M^{[1]\sigma_1} \dots \tilde{M}^{[i]\sigma_i} \tilde{M}^{[p]\sigma_p} \dots M^{[N],\sigma_N}. \end{aligned} \quad (2.123)$$

The action of the swap gate is shown in Fig. 2.9. Using the swap gates, we can apply the operator $e^{-i\hat{H}\delta t}$ onto the MPS as a series of neighboring three site gates. We comment that the swap gates introduce no additional error except for the SVD truncation error.

We summarize the time evolution method using the TEBD algorithm with the swap gates.

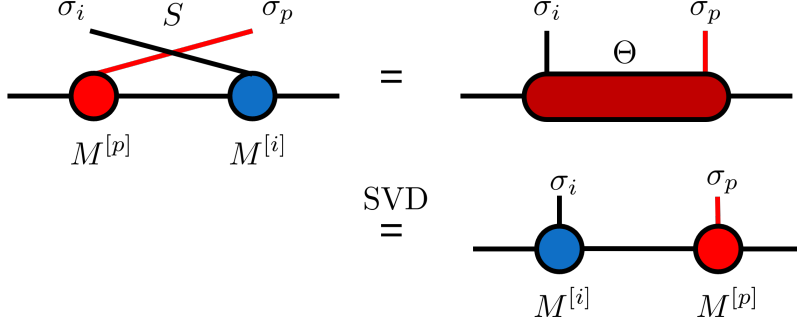


Figure 2.9: The action of the swap gate. The swap gate changes the position of two MPS.

- (i) Prepare the ground state MPS calculated by the DMRG algorithm. In this expression, the photon site is at the beginning of the chain, i.e. :

$$M^{[p]\sigma_p} M^{[1]\sigma_1} \dots M^{[N]\sigma_N}.$$

- (ii) Start from site $i = 1$. We apply a three-site gate to the MPS and update the MPS by SVD.

$$\begin{aligned} & M^{[1]\sigma_1} \dots U_{p,i,i+1}(M^{[p]\sigma_p} M^{[i]\sigma_i} M^{[i+1]\sigma_{i+1}}) \dots M^{[N]\sigma_N} \\ \rightarrow & M^{[1]\sigma_1} \dots \Theta^{\sigma_p, \sigma_i, \sigma_{i+1}} \dots M^{[N]\sigma_N} \\ \xrightarrow{\text{SVD}} & M^{[1]\sigma_1} \dots \tilde{M}^{[p]\sigma_p} \tilde{M}^{[i]\sigma_i} \tilde{M}^{[i+1]\sigma_{i+1}} \dots M^{[N]\sigma_N}. \end{aligned}$$

- (iii) Swap the photon site to the next,

$$\begin{aligned} & M^{[1]\sigma_1} \dots S_{p,i}(M^{[p]\sigma_p} M^{[i]\sigma_i}) M^{[i+1]\sigma_{i+1}} \dots M^{[N]\sigma_N} \\ \xrightarrow{\text{SVD}} & M^{[1]\sigma_1} \dots \tilde{M}^{[i]\sigma_i} \tilde{M}^{[p]\sigma_p} M^{[i+1]\sigma_{i+1}} \dots M^{[N]\sigma_N}. \end{aligned}$$

- (iv) Repeat the procedure above until we reach $i = N$. Then, we perform the procedure from the end of the chain $i = N$ to the beginning of the chain $i = 1$. This is one step of the time evolution with δt . At this point, we can calculate the expectation value of physical quantities $\langle O(t + \delta t) \rangle$ using the MPO such as Eq. (2.88). The procedure continues until the total time reaches the one we want.

A diagrammatic representation of the time evolution by δt is shown in Fig. 2.10.

2.4.4 Error sources

There are two sources of numerical errors in TEBD: (1) errors from the Suzuki-Trotter decomposition and (2) errors from SVD truncation. The first one is the time step error of order $\mathcal{O}(\delta t^3)$ per time step for the second-order TEBD. If we fix the total time interval as $T = N\delta t$, the total error is $\mathcal{O}(N\delta t^3) = \mathcal{O}(T\delta t^2)$. It can be reduced by choosing a smaller time step size δt or employing a higher-order decomposition. Both treatments increase the total number of SVD to calculate a state for a fixed time interval T . The second one is an artificial error arising from limiting the bond dimension to χ_{\max} . It can be reduced by using larger χ_{\max} , but it increases the computational cost of SVD at each time step.

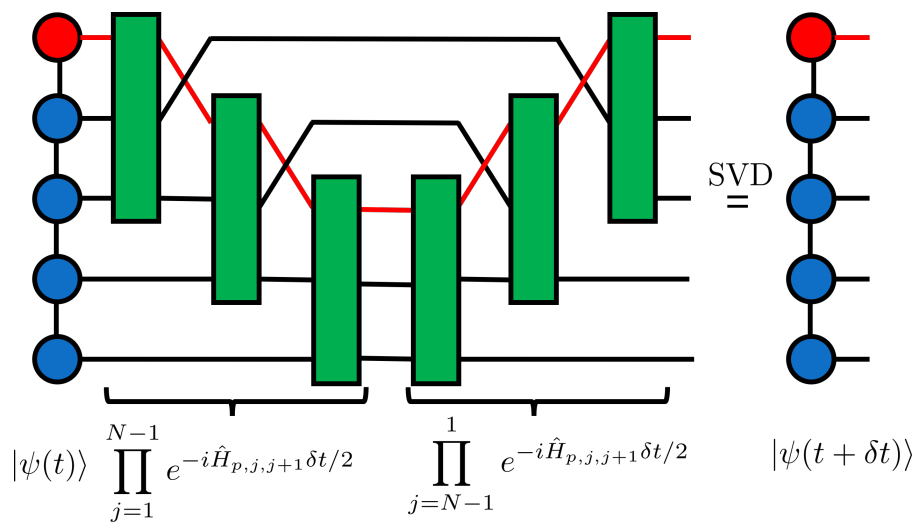


Figure 2.10: A diagrammatic representation of the time evolution by δt . The Suzuki Trotter gates and the swap gates are applied to $|\psi\rangle$. We use SVD after applying a gate.

Chapter 3

Ground-State Properties

In this chapter, we present numerical results of the ground state of the 1DEHM coupled with an optical cavity. In the first section, we briefly explain how we calculate the physical quantities. In the second section, we investigate how the Coulomb interaction affects the photon number. The perturbation analysis and squeezed transformation analysis are given to explain the Coulomb interaction dependence. In the third section, we focus on the squeezing effects. We calculate the Wigner functions and the probability distribution of photons to see how the squeezing appears.

3.1 Ground-state calculation

In numerical calculations, we first calculate the ground state $|\Psi_{\text{GS}}\rangle$ of the 1DEHM with an optical cavity

$$\begin{aligned}\hat{H} = & \Omega \hat{a}^\dagger \hat{a} - W \sum_{j,\sigma} (e^{i \frac{G}{\sqrt{N}} (\hat{a} + \hat{a}^\dagger)} \hat{c}_{j,\sigma}^\dagger \hat{c}_{j+1,\sigma} + \text{h.c.}) \\ & + U \sum_j \hat{n}_{j,\uparrow} \hat{n}_{j,\downarrow} + V \sum_j \hat{n}_j \hat{n}_{j+1}\end{aligned}\quad (3.1)$$

by the DMRG method. We calculate the physical quantities of photons because our subject of interest is the virtual photons in the ground state. The MPS form of the ground state allows us to compute the photon density matrix by tracing out the electron degree of freedom as

$$\rho_{\text{ph,GS}} = \text{Tr}_e[|\Psi_{\text{GS}}\rangle \langle \Psi_{\text{GS}}|]. \quad (3.2)$$

Then, the expectation value of \hat{O} is calculated as

$$\langle \hat{O} \rangle_{\text{GS}} = \text{Tr}_{\text{ph}}[\hat{O} \hat{\rho}_{\text{ph,GS}}]. \quad (3.3)$$

Numerical calculations are performed for the number of electrons $N = 80$ at half-filling. In the DMRG calculation, we use the maximum bond dimension $\chi_{\text{max}} = 1600$ and photon cutoff $N_{\text{max}} = 20$ based on the convergence checks in Appendix A. In the following, we use the hopping parameter as the energy unit, and set the cavity frequency to $\Omega/W = 10$.

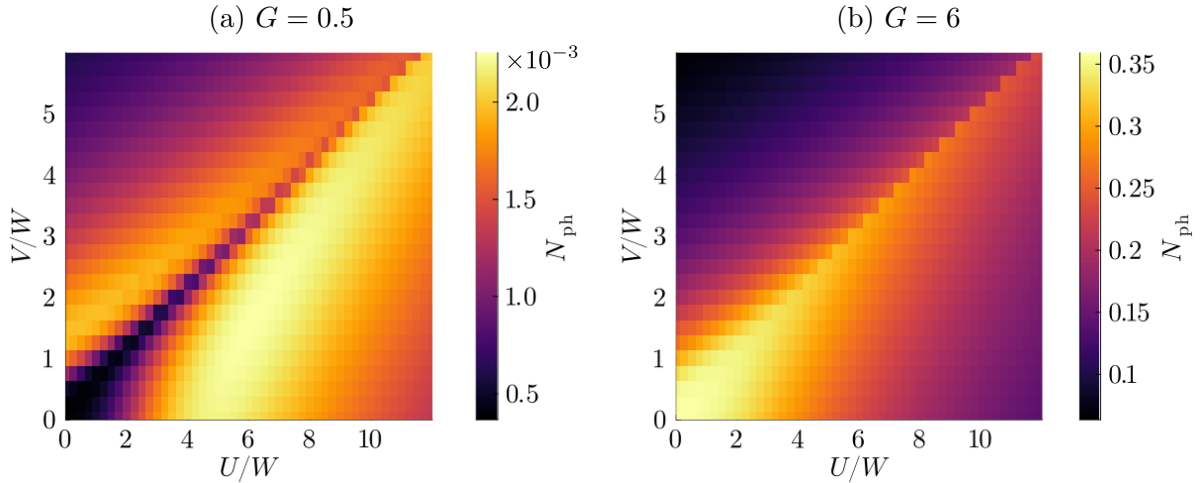


Figure 3.1: Dependence of the photon number on the on-site and nearest-neighbor Coulomb interaction U , V with different coupling constants (a) $G = 0.5$ and (b) $G = 6$. The cavity frequency is $\Omega/W = 10$. Note that the color bar scales in the figures are different.

3.2 Virtual photons

In the ground state, electrons and photons are hybridized, where the physical quantities of photons reflect the information of electrons. In this section, we focus on how the Coulomb interaction has effects on the photon number, defined as

$$N_{\text{ph}} := \langle \hat{a}^\dagger \hat{a} \rangle_{\text{GS}}. \quad (3.4)$$

Fig. 3.1 shows the photon number as a function of the on-site Coulomb interaction U and nearest-neighbor Coulomb interaction V with different coupling constants $G = 0.5$ and $G = 6$. The U and V dependence of the photon number varies significantly between the two different coupling constants. For $G = 0.5$, the photon number is suppressed along the diagonal line, $V = U/2$, and takes large values slightly away from this line. On the other hand, for $G = 6$, the photon number is enhanced along this line. The line separates the CDW phase from the SDW phase as seen in Sect. 1.3.1, indicating that the virtual photons reflect the structure of the quantum many-body system. In order to understand the behavior, we perform the perturbation and squeezed transformation analyses.

3.2.1 Perturbation analysis

In this section, we consider the large U , V , and Ω limit and perform the second-order perturbation theory. In the following, we use the Hamiltonian in the quadratic order of the cavity-matter coupling constant since expanding the Peierls phase up to the quadratic order is relevant in the thermodynamic limit as seen in Sect. 2.1.2. We regard the cavity-matter decoupled Hamiltonian as the non-perturbative Hamiltonian, whereas the cavity-matter coupling is treated as a perturbation. Thus, we divide the Hamiltonian into the

non-perturbative and the perturbative parts as

$$\hat{H} = \hat{H}_0 + \hat{V}, \quad (3.5)$$

$$\hat{H}_0 = \Omega \hat{a}^\dagger \hat{a} + \hat{T} + U \sum_j \hat{n}_{j,\uparrow} \hat{n}_{j,\downarrow} + V \sum_j \hat{n}_j \hat{n}_{j+1}, \quad (3.6)$$

$$\hat{V} = \frac{G}{\sqrt{N}} \hat{J}(\hat{a} + \hat{a}^\dagger) - \frac{G^2}{2N} \hat{T}(\hat{a} + \hat{a}^\dagger)^2, \quad (3.7)$$

where the kinetic energy term and current operator term are introduced as

$$\hat{T} = -W \sum_{j,\sigma} (\hat{c}_{j,\sigma}^\dagger \hat{c}_{j+1,\sigma} + \text{h.c.}), \quad (3.8)$$

$$\hat{J} = -Wi \sum_{j,\sigma} (\hat{c}_{j,\sigma}^\dagger \hat{c}_{j+1,\sigma} - \text{h.c.}). \quad (3.9)$$

The eigenenergies of the non-perturbative Hamiltonian are the sum of the eigenenergies of 1DEHM E_a and those of the cavity photons $l\Omega$ ($l = 0, 1, 2, \dots$). We denote the eigenenergies as $E_n^{(0)} = E_{a,l}^{(0)} = E_a + l\Omega$. The eigenstates are denoted as $|\Psi_n^{(0)}\rangle = |\Psi_{a,l}^{(0)}\rangle = |\phi_a\rangle |l\rangle$, where $|\phi_a\rangle$ are the eigenstates of 1DEHM and $|l\rangle$ are the Fock states of the cavity photons with photon number l . Then, one can obtain the ground state of the perturbed system in the second order as

$$\begin{aligned} |\Psi_0^{(2)}\rangle &= \left(1 - \frac{1}{2} \sum_{n \neq 0} \frac{|V_{n,0}|^2}{(E_0^{(0)} - E_n^{(0)})^2} \right) |\Psi_0^{(0)}\rangle + \sum_{n \neq 0} \frac{V_{n,0}}{E_0^{(0)} - E_n^{(0)}} |\Psi_n^{(0)}\rangle \\ &\quad + \sum_{n,m \neq 0} \frac{V_{n,m} V_{m,0}}{(E_0^{(0)} - E_n^{(0)})(E_0^{(0)} - E_m^{(0)})} |\Psi_n^{(0)}\rangle \\ &\quad - \sum_{n \neq 0} \frac{V_{n,0} V_{0,0}}{(E_0^{(0)} - E_n^{(0)})^2} |\Psi_n^{(0)}\rangle, \end{aligned} \quad (3.10)$$

where $V_{n,m} = \langle \Psi_n^{(0)} | \hat{V} | \Psi_m^{(0)} \rangle$. With this state, one can calculate the photon number in the second order as

$$\begin{aligned} N_{\text{ph}}^{(2)} &= \langle \Psi_0^{(2)} | \hat{a}^\dagger \hat{a} | \Psi_0^{(2)} \rangle \\ &= \sum_{n,m \neq 0} \frac{V_{0,m} V_{n,0}}{(E_0^{(0)} - E_n^{(0)})(E_0^{(0)} - E_m^{(0)})} \langle \Psi_m^{(0)} | \hat{a}^\dagger \hat{a} | \Psi_n^{(0)} \rangle \\ &= \sum_{a,l \neq 0} \frac{\left| \langle l | \langle \phi_a | \hat{V} | \phi_0 \rangle | 0 \rangle \right|^2}{(E_0 - E_a - l\Omega)^2} \langle l | \hat{a}^\dagger \hat{a} | l \rangle, \end{aligned} \quad (3.11)$$

where in the third line, we have used the fact that the operator $\hat{a}^\dagger \hat{a}$ is diagonal in the Fock basis. The first and second terms in \hat{V} create one photon and two photons, respectively,

so that we can write Eq. (3.11) as

$$\begin{aligned}
 N_{\text{ph}}^{(2)} &= \left(\frac{G}{\sqrt{N}}\right)^2 \sum_a \frac{\left|\langle 1| (\hat{a}^\dagger + \hat{a}) |0\rangle\right|^2 \left|\langle \phi_a | \hat{J} | \phi_0 \rangle\right|^2}{(1\Omega + E_a - E_0)^2} \langle 1| \hat{a}^\dagger \hat{a} |1\rangle \\
 &\quad + \left(\frac{G^2}{2N}\right)^2 \sum_a \frac{\left|\langle 2| (\hat{a}^\dagger + \hat{a})^2 |0\rangle\right|^2 \left|\langle \phi_a | \hat{T} | \phi_0 \rangle\right|^2}{(2\Omega + E_a - E_0)^2} \langle 2| \hat{a}^\dagger \hat{a} |2\rangle \\
 &= \frac{G^2}{N} \sum_a \frac{\left|\langle \phi_a | \hat{J} | \phi_0 \rangle\right|^2}{(1\Omega + E_a - E_0)^2} + \frac{G^4}{N^2} \sum_a \frac{\left|\langle \phi_a | \hat{T} | \phi_0 \rangle\right|^2}{(2\Omega + E_a - E_0)^2} \\
 &\approx \frac{G^2}{N} \sum_a \frac{\left|\langle \phi_a | \hat{J} | \phi_0 \rangle\right|^2}{(1\Omega + \Delta E)^2} + \frac{G^4}{N^2} \sum_a \frac{\left|\langle \phi_a | \hat{T} | \phi_0 \rangle\right|^2}{(2\Omega + \Delta E)^2} \\
 &= \frac{G^2}{N} \frac{\langle \Delta \hat{J}^2 \rangle_{\text{GS}}}{(1\Omega + \Delta E)^2} + \frac{G^4}{N^2} \frac{\langle \hat{T} \rangle_{\text{GS}}^2}{4\Omega^2} + \frac{G^4}{N^2} \frac{\langle \Delta \hat{T}^2 \rangle_{\text{GS}}}{(2\Omega + \Delta E)^2}. \tag{3.12}
 \end{aligned}$$

Here, we define the fluctuation operator as $\Delta \hat{O} = \hat{O} - \langle \hat{O} \rangle_{\text{GS}}$, in which $\langle \rangle_{\text{GS}}$ means the expectation value for the ground state of 1DEHM without the cavity. In the fourth line, we make an approximation that the excited energies induced by the current and hopping are represented by a single energy,

$$\Delta E = \begin{cases} U - V & (V \leq U/2) \\ 3V - U & (V \geq U/2), \end{cases}$$

which can be readily estimated in the large Coulomb interaction limit ($U, V \gg W$). In this limit, the SDW state comprises singly occupied states. Thus, the energy of the first-excited state, characterized by the presence of an adjacent doublon and holon, is approximately $U - V$. On the other hand, doublons and holons align alternately in the CDW state. Therefore, the first-excited state, where two adjacent sites become singly occupied, requires an excitation energy of approximately $3V - U$. Due to the approximation, we can evaluate the perturbation result Eq. (3.12) by the ground state of 1DEHM without a cavity, which can be calculated by the DMRG.

We make some comments on the perturbation result. First, the virtual photons appear in the thermodynamic limit because $(\langle \Delta \hat{J}^2 \rangle_{\text{GS}} / N)$ and $(\langle \hat{T} \rangle_{\text{GS}}^2 / N^2)$ have nonzero values in the limit of $N \rightarrow \infty$. In contrast, the third term proportional to $(\langle \Delta \hat{T}^2 \rangle_{\text{GS}} / N^2)$ vanishes in the thermodynamic limit. Second, the number of the virtual photons is proportional to G^2 for small G , although the coupling strength at one electron level $g = G/\sqrt{N}$ is not so large. Therefore, the appearance of the virtual photons is a collective coupling phenomenon. Third, the perturbation result includes a counter-rotating process because both the photons and electrons in the 1DEHM are excited in the intermediate state of the perturbation. In this process, current fluctuation is essential to excite the 1DEHM.

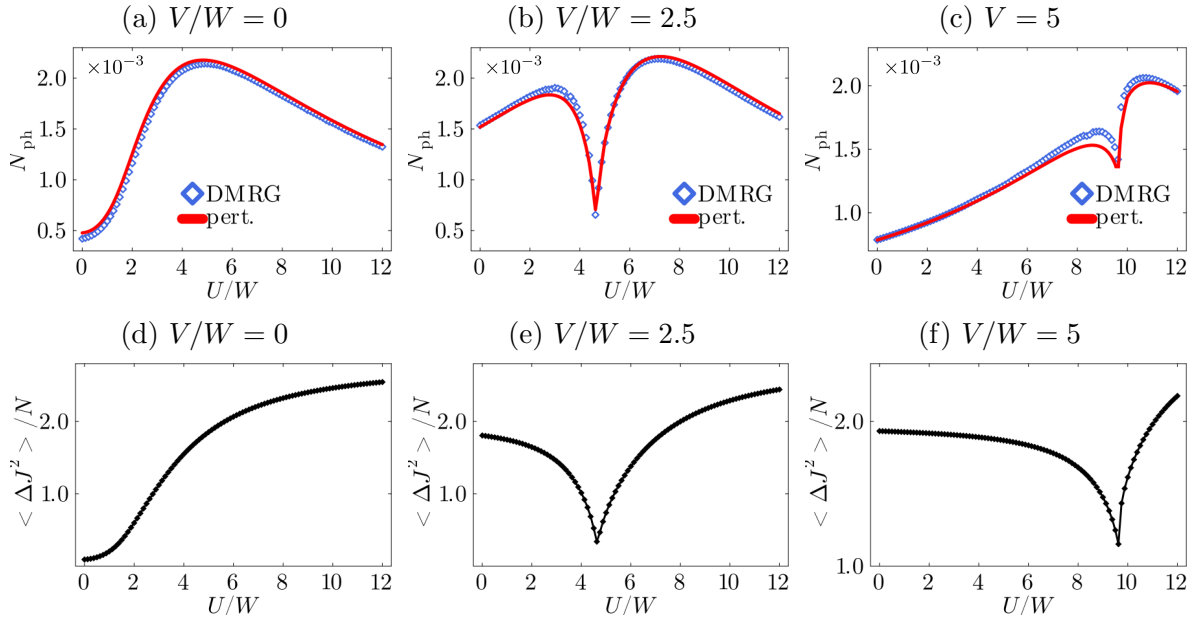


Figure 3.2: Comparison of the photon number calculated from the DMRG (blue marks) and the perturbation analysis (red line) as a function of the on-site Coulomb interaction U/W with different nearest-neighbor interactions (a) $V/W = 0$, (b) $V/W = 2.5$ and (c) $V/W = 5$. The calculation is performed for $G = 0.5$ and $\Omega/W = 10$. The DMRG results and the perturbation results agree well. We also show the current fluctuation per site in the ground state of 1DEHM at (d) $V/W = 0$, (e) $V/W = 2.5$ and (f) $V/W = 5$ calculated by the DMRG. The minimum point of the current fluctuation corresponds to the local minimum of the photon number.

We compare the expressions obtained in Eq. (3.12) to the DMRG result of the full Hamiltonian Eq. (3.1) as a function of the on-site Coulomb interaction U with different nearest-neighbor interactions V in Fig. 3.2 at $G = 0.5$. In spite of the rough approximation of ΔE , we find good agreement between the DMRG and the perturbation results. For the small value of G , the main contribution of the perturbation result comes from the first term in Eq. (3.12), which is proportional to the current fluctuation and is inversely proportional to $\Omega + \Delta E$. If we focus on $\Omega + \Delta E$ in the denominator of this term, ΔE becomes minimal at the point $V = U/2$, and the photon number increases. However, if we focus on the current fluctuation in the numerator, it takes a minimum value (shown in the bottom panel of Fig. 3.2) at the point $V \approx U/2$, and the photon number decreases. Due to these competitions, the photon number takes a small value on the line $V = U/2$ and reaches its maximum slightly away from this line.

3.2.2 Squeezed transformation analysis

Perturbative analysis works for a small coupling constant. However, as the coupling constant increases, it fails to reproduce the results obtained by DMRG calculations. Fig. 3.3a shows that the perturbation results overestimate the photon number for a large coupling

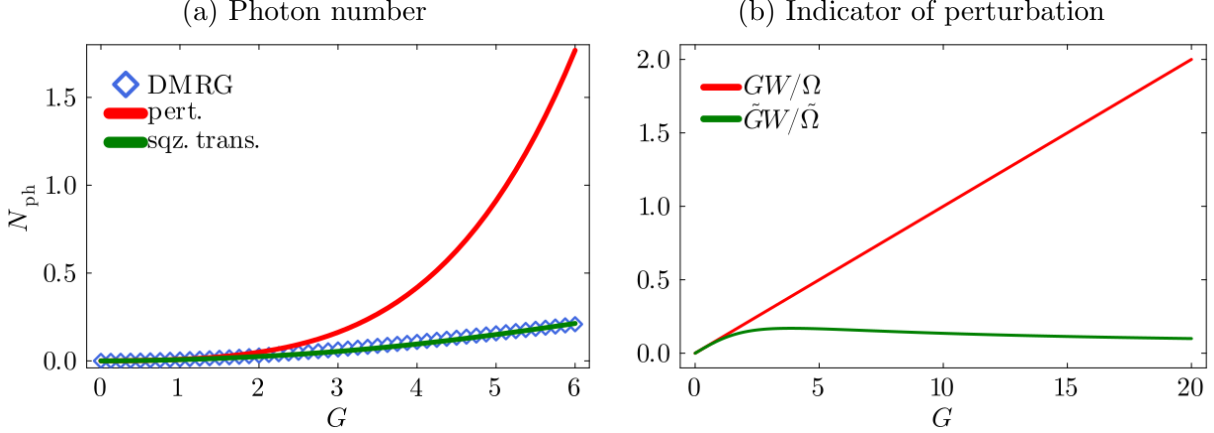


Figure 3.3: Comparison of the perturbation analysis and the squeezed transformation analysis. The calculation is performed at $U/W = 10$, $V/W = 3$ and $\Omega/W = 10$ (a) Coupling constant dependence of the photon number. The DMRG result (blue marks), the perturbation result (red line), and the squeezed transformation result (green line) are compared. (b) GW/Ω and $\tilde{GW}/\tilde{\Omega}$ as a function of the coupling constant.

constant. The key to analyzing the large coupling constant regime is squeezed transformation [61, 73, 83–85]. We decompose the kinetic energy term appearing in the quadratic expansion of the Peierls phase into the expectation value in terms of the ground state and fluctuation as $\hat{T} = \langle \hat{T} \rangle_{GS} + \Delta \hat{T}$. The part that includes the second-order terms of the photon operator can be diagonalized by a squeezed transformation, i.e. :

$$\Omega \hat{a}^\dagger \hat{a} - \frac{G^2}{2N} \langle \hat{T} \rangle_{GS} (\hat{a} + \hat{a}^\dagger)^2 = \tilde{\Omega} \hat{b}^\dagger \hat{b}, \quad (3.13)$$

where we define a squeezed state annihilation (creation) operator \hat{b} (\hat{b}^\dagger) using a squeezed operator $\hat{S}(\zeta)$ as

$$\begin{aligned} \begin{pmatrix} \hat{b} \\ \hat{b}^\dagger \end{pmatrix} &= \begin{pmatrix} \hat{S}(\zeta) \hat{a} \hat{S}^\dagger(\zeta) \\ \hat{S}(\zeta) \hat{a}^\dagger \hat{S}^\dagger(\zeta) \end{pmatrix} \\ &= \begin{pmatrix} \cosh(\zeta) & \sinh(\zeta) \\ \sinh(\zeta) & \cosh(\zeta) \end{pmatrix} \begin{pmatrix} \hat{a} \\ \hat{a}^\dagger \end{pmatrix}, \end{aligned} \quad (3.14)$$

$$\hat{S}(\zeta) = e^{\frac{\zeta}{2}(\hat{a}^2 - \hat{a}^{\dagger 2})}, \quad (3.15)$$

$$\zeta = \frac{1}{2} \ln \left(\frac{\tilde{\Omega}}{\Omega} \right), \quad (3.16)$$

$$\tilde{\Omega} = \Omega \sqrt{1 - 2 \frac{G^2 \langle \hat{T} \rangle_{GS}}{\Omega N}}. \quad (3.17)$$

\hat{b} satisfies the commutation relation $[\hat{b}, \hat{b}^\dagger] = 1$ since the squeezed operator is unitary. $\tilde{\Omega}$ is the renormalized cavity frequency by the squeezing. The Hamiltonian can be rewritten

with the squeezed state annihilation and creation operators and the fluctuation term as

$$\hat{H} = \hat{H}_0 + \hat{V}, \quad (3.18)$$

$$\hat{H}_0 = \tilde{\Omega} \hat{b}^\dagger \hat{b} + \hat{T} + U \sum_j \hat{n}_{j,\uparrow} \hat{n}_{j,\downarrow} + V \sum_j \hat{n}_j \hat{n}_{j+1}, \quad (3.19)$$

$$\hat{V} = \frac{\tilde{G}}{\sqrt{N}} \hat{J} (\hat{b} + \hat{b}^\dagger) - \frac{\tilde{G}^2}{2N} \Delta \hat{T} (\hat{b} + \hat{b}^\dagger)^2, \quad (3.20)$$

$$\tilde{G} = G e^{-\zeta} = G \sqrt{\frac{\Omega}{\tilde{\Omega}}}. \quad (3.21)$$

\tilde{G} is the renormalized cavity-matter coupling constant. This Hamiltonian has the same form as the one before the squeezed transformation, except for the changes of the parameters and operators, $\Omega \rightarrow \tilde{\Omega}$, $G \rightarrow \tilde{G}$, $\hat{T} \rightarrow \Delta \hat{T}$ and $\hat{a} \rightarrow \hat{b}$. However, the transformation has an advantage in performing the perturbation. Fig. 3.3b shows GW/Ω and $\tilde{G}W/\tilde{\Omega}$ as an indicator of the validity of the perturbation. Compared to GW/Ω , $\tilde{G}W/\tilde{\Omega}$ remains small over the entire region of the coupling constant and vanishes in the strong-coupling limit $G \rightarrow \infty$. In fact, renormalized coupling constant and renormalized cavity frequency scale as $\tilde{G} \propto \sqrt{G}$ and $\tilde{\Omega} \propto G\Omega$ in the strong-coupling limit. Therefore, the ratio between them scales as $\tilde{G}W/\tilde{\Omega} \propto W/\sqrt{G}\Omega$, and asymptotically decoupled in the strong-coupling limit [83–85].

The photon number is calculated with the squeezed transformation as

$$\begin{aligned} N_{\text{ph}} &= \langle \hat{a}^\dagger \hat{a} \rangle_{\text{GS}} \\ &= \left\langle \left(-\sinh(\zeta) \hat{b} + \cosh(\zeta) \hat{b}^\dagger \right) \left(\cosh(\zeta) \hat{b} - \sinh(\zeta) \hat{b}^\dagger \right) \right\rangle_{\text{GS}} \\ &= (\cosh^2(\zeta) + \sinh^2(\zeta)) \langle \hat{b}^\dagger \hat{b} \rangle_{\text{GS}} + \sinh^2(\zeta) - 2 \sinh(\zeta) \cosh(\zeta) \langle \hat{b}^\dagger \hat{b}^\dagger \rangle_{\text{GS}} \end{aligned} \quad (3.22)$$

The expectation value of the squeezed photon number can be calculated in the same way as in Eq. (3.12) :

$$\langle \hat{b}^\dagger \hat{b} \rangle_{\text{GS}} \approx \frac{\tilde{G}^2}{N} \frac{<\Delta \hat{J}^2>_{\text{GS}}}{(1\tilde{\Omega} + \Delta E)^2} + \frac{\tilde{G}^4}{N^2} \frac{<\Delta \hat{T}^2>_{\text{GS}}}{(2\tilde{\Omega} + \Delta E)^2}. \quad (3.23)$$

There does not appear to be a term corresponding to the second term in Eq. (3.12), since the contribution from the ground state kinetic energy is incorporated into the squeezed transformation. The expectation value of the double creation operator can be calculated

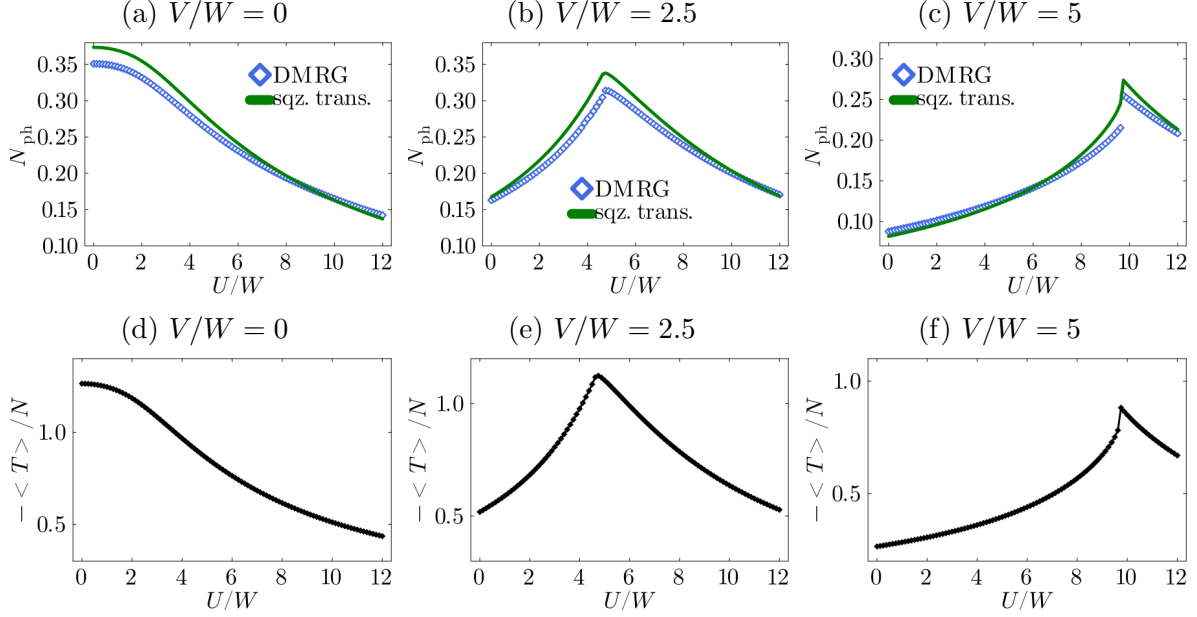


Figure 3.4: Comparison of the photon number calculated from the DMRG (blue marks) and the squeezed transformation analysis (green line) as a function of the on-site Coulomb interaction U/W with different nearest-neighbor interactions (a) $V/W = 0$, (b) $V/W = 2.5$ and (c) $V/W = 5$. The calculation is performed for $G = 6$ and $\Omega/W = 10$. The DMRG results and the squeezed transformation results agree well. We also show the kinetic energy per site in the ground state of 1DEHM at (d) $V/W = 0$, (e) $V/W = 2.5$ and (f) $V/W = 5$ calculated by the DMRG. The maximum point of the current fluctuation corresponds to the local maximum of the photon number.

as

$$\begin{aligned}
 \langle \hat{b}^\dagger \hat{b}^\dagger \rangle_{\text{GS}} &= \sum_{n \neq 0} \frac{V_{0,n}}{E_0^{(0)} - E_n^{(0)}} \langle \Psi_n^{(0)} | \hat{b}^\dagger \hat{b}^\dagger | \Psi_0^{(0)} \rangle \\
 &\quad + \sum_{n,m \neq 0} \frac{V_{0,m} V_{m,n}}{(E_0^{(0)} - E_m^{(0)})(E_0^{(0)} - E_n^{(0)})} \langle \Psi_n^{(0)} | \hat{b}^\dagger \hat{b}^\dagger | \Psi_0^{(0)} \rangle \\
 &= -\frac{\tilde{G}^2}{2N} \frac{\langle 0 | (\hat{b}^\dagger + \hat{b})^2 | 2 \rangle \langle \phi_0 | \Delta \hat{T} | \phi_0 \rangle}{-2\tilde{\Omega}} \langle 2 | \hat{b}^\dagger \hat{b}^\dagger | 0 \rangle \\
 &\quad + \frac{\tilde{G}^2}{N} \sum_a \frac{\langle 0 | (\hat{b}^\dagger + \hat{b}) | 1 \rangle \langle 1 | (\hat{b}^\dagger + \hat{b}) | 2 \rangle \left| \langle \phi_0 | \hat{J} | \phi_a \rangle \right|^2}{2\tilde{\Omega}(\tilde{\Omega} + E_a - E_0)} \langle 2 | \hat{b}^\dagger \hat{b}^\dagger | 0 \rangle \\
 &\approx \frac{\tilde{G}^2}{2N} \frac{\langle \Delta \hat{T} \rangle_{\text{GS}}}{\tilde{\Omega}} + \frac{\tilde{G}^2}{N} \frac{\langle \Delta \hat{J}^2 \rangle_{\text{GS}}}{\tilde{\Omega}(\tilde{\Omega} + \Delta E)}, \tag{3.24}
 \end{aligned}$$

where the first term in the above vanishes due to $\langle \Delta \hat{T} \rangle_{\text{GS}} = 0$.

We compare the expressions obtained in Eq. (3.22) to the DMRG result of the full Hamiltonian Eq. (3.1) as a function of on-site Coulomb interaction U with different

nearest-neighbor interaction V in Fig. 3.4 at $G = 6$. We observe that the squeezed transformation results agree well with the DMRG results. In the strong-coupling limit, the second term in Eq. (3.22) is $\mathcal{O}(G)$, while the others are $\mathcal{O}(G^0)$. Therefore, the main contribution in the squeezed transformation result comes from the $\sinh^2(\zeta)$ term for the large coupling constant. $\sinh^2(\zeta)$ can be considered as a contribution from the squeezed vacuum because that term exists regardless of the presence of the squeezed photons. In the strong-coupling limit, the squeezed vacuum contribution scales as $\sinh^2(\zeta) \propto \sqrt{-2G^2 \langle \hat{T} \rangle_{\text{GS}} / \Omega N}$, which depends on the square root of the absolute value of the kinetic energy. From this analysis, we can explain the large photon number along the line $V = U/2$ because the absolute value of the kinetic energy takes the maximum value at the point (shown in the bottom panel of Fig. 3.4).

3.3 Squeezing of photons

As shown in the previous section, the photon squeezing is important to obtain the virtual photons for a large coupling constant. In order to see the squeezing directly, we calculate the ratio between the variance of canonical momentum and coordinate operator, $\Delta P/\Delta X$, and the product $\Delta P\Delta X$. The canonical momentum, coordinate operator and its variance are defined as

$$\hat{P} : = \frac{i}{\sqrt{2}}(\hat{a} - \hat{a}^\dagger), \quad (3.25)$$

$$\hat{X} : = \frac{1}{\sqrt{2}}(\hat{a} + \hat{a}^\dagger), \quad (3.26)$$

$$\Delta O : = \sqrt{\langle \hat{O}^2 \rangle_{\text{GS}} - \langle \hat{O} \rangle_{\text{GS}}^2}. \quad (3.27)$$

$\Delta P/\Delta X$ represents the ratio between the fluctuations in the P direction and the X direction in the phase space of the photons, directly characterizing squeezing. On the other hand, $\Delta P\Delta X$ represents the product of these fluctuations, which is bounded by 1/2 due to the Heisenberg uncertainty relationship. When $\Delta P/\Delta X$ is large and $\Delta P\Delta X$ is close to 1/2, squeezing is achieved while minimizing the total fluctuations. Fig. 3.5 shows DMRG calculation results for $\Delta P/\Delta X$ and $\Delta P\Delta X$ as a function of the on-site Coulomb interaction U and nearest-neighbor Coulomb interaction V at $G = 6$. $\Delta P/\Delta X$ takes a large value along the diagonal line $V = U/2$, while $\Delta P\Delta X$ is close to 1/2 along the line.

In order to understand the behavior, we also perform the squeezed transformation

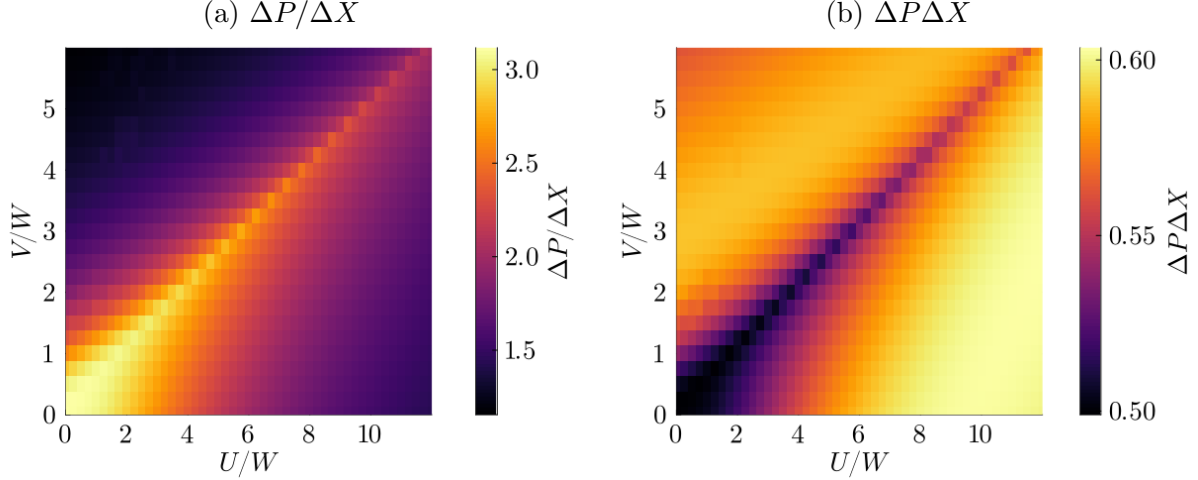


Figure 3.5: (a) $\Delta P/\Delta X$ and (b) $\Delta P\Delta X$ as a function of U, V . Cavity frequency and coupling constant are fixed to be $\Omega/W = 10$ and $G = 6$.

analysis to the canonical momentum and its coordinate as

$$\begin{aligned}
 \frac{\Delta P}{\Delta X} &= \sqrt{\frac{\langle \hat{P}^2 \rangle_{\text{GS}}}{\langle \hat{X}^2 \rangle_{\text{GS}}}} \\
 &= \sqrt{\frac{-\langle (\hat{a} - \hat{a}^\dagger)^2 \rangle_{\text{GS}}}{\langle (\hat{a} + \hat{a}^\dagger)^2 \rangle_{\text{GS}}}} \\
 &= \frac{\cosh(\zeta) + \sinh(\zeta)}{\cosh(\zeta) - \sinh(\zeta)} \sqrt{\frac{-\langle (\hat{b} - \hat{b}^\dagger)^2 \rangle_{\text{GS}}}{\langle (\hat{b} + \hat{b}^\dagger)^2 \rangle_{\text{GS}}}} \\
 &= e^{2\zeta} \sqrt{\frac{2\langle \hat{b}^\dagger \hat{b} \rangle_{\text{GS}} + 1 - 2\langle \hat{b}^\dagger \hat{b}^\dagger \rangle_{\text{GS}}}{2\langle \hat{b}^\dagger \hat{b} \rangle_{\text{GS}} + 1 + 2\langle \hat{b}^\dagger \hat{b}^\dagger \rangle_{\text{GS}}}}, \tag{3.28}
 \end{aligned}$$

$$\begin{aligned}
 \Delta P\Delta X &= \left(\frac{1}{\sqrt{2}}\right)^2 (\cosh(\zeta)^2 - \sinh^2(\zeta)) \sqrt{-\langle (\hat{b} - \hat{b}^\dagger)^2 \rangle_{\text{GS}} \langle (\hat{b} + \hat{b}^\dagger)^2 \rangle_{\text{GS}}} \\
 &= \frac{1}{2} \sqrt{(2\langle \hat{b}^\dagger \hat{b} \rangle_{\text{GS}} + 1)^2 - 4\langle \hat{b}^\dagger \hat{b}^\dagger \rangle_{\text{GS}}^2} \tag{3.29}
 \end{aligned}$$

where in the first line, we have used the fact that the $\langle \hat{P} \rangle_{\text{GS}} = \langle \hat{X} \rangle_{\text{GS}} = 0$ because the expectation value of the single creation and annihilation operator is zero in the second-order perturbation analysis. $e^{2\zeta} = \sqrt{1 - 2\frac{G^2 \langle \hat{T} \rangle_{\text{GS}}}{\Omega N}}$ is proportional to the square root of the absolute value of the kinetic energy in the strong-coupling limit, which is the same as in the case of the photon number. Therefore, $\Delta P/\Delta X$ takes a large value along the line $V = U/2$ due to a large absolute value of the kinetic energy. In contrast, $\langle \hat{b}^\dagger \hat{b} \rangle_{\text{GS}}$ and $\langle \hat{b}^\dagger \hat{b}^\dagger \rangle_{\text{GS}}$ take small values along the line due to the small current fluctuation. Therefore, $\Delta P\Delta X$ is close to 1/2 along the line.

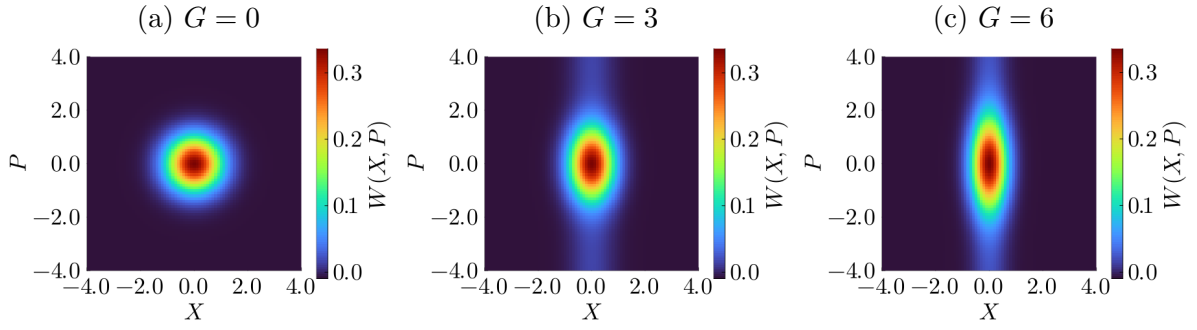


Figure 3.6: DMRG results of the Wigner function $W(X, P)$ at $G = 0$, (b) $G = 3$, and (c) $G = 6$. Cavity frequency and the Coulomb interaction are fixed at $\Omega/W = 10$, $U/W = 6$, and $V/W = 3$.

3.3.1 Wigner function

In order to visualize the squeezing, we also calculated the Wigner function, defined as

$$W(X, P) = \frac{1}{\pi} \int_{-\infty}^{\infty} dY \langle X + Y | \hat{\rho}_{\text{ph,GS}} | X - Y \rangle e^{2iPY}. \quad (3.30)$$

The Wigner function provides a way to represent quantum states in the phase space. Fig. 3.6 shows the Wigner function for different coupling constants at $\Omega/W = 10$, $U/W = 6$, and $V/W = 3$. For $G = 0$, the photon and the matter are decoupled so that the photon ground state is the vacuum state, whose Wigner function is the isotropic Gaussian, i.e.,

$$W(X, P) = \frac{1}{\pi} \exp(-X^2 - P^2). \quad (3.31)$$

However, for finite coupling constants, the fluctuation in the P direction is increased, while the one in the X direction is suppressed. The tendency becomes stronger as the coupling constant increases. The Wigner function of the squeezed vacuum state with a given squeezed parameter ζ is written as

$$W(X, P) = \frac{1}{\pi} \exp(-e^{2\zeta} X^2 - e^{-2\zeta} P^2). \quad (3.32)$$

Therefore, squeezing is enhanced for a large coupling constant, which corresponds to a large squeezed parameter.

3.3.2 Probability distribution

In the squeezed transformation analysis, we combine the squeezed transformation and perturbation. This means that the appearance of the virtual photon is determined by both the squeezing and counter-rotating process. In order to see that, we calculate the probability distribution, defined as

$$P(n_{\text{ph}}) := \langle |n_{\text{ph}}\rangle \langle n_{\text{ph}}| \rangle_{\text{GS}}, \quad (3.33)$$

$$\hat{a}^\dagger \hat{a} |n_{\text{ph}}\rangle = n_{\text{ph}} |n_{\text{ph}}\rangle. \quad (3.34)$$

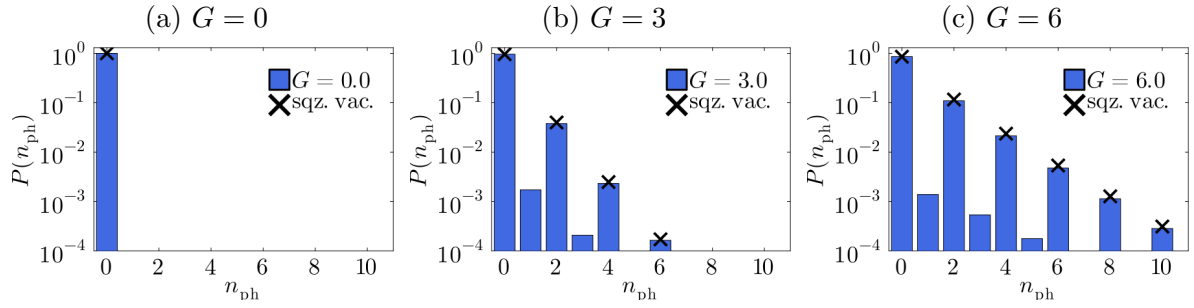


Figure 3.7: DMRG results of the probability distribution $P(n_{\text{ph}})$ in the logarithmic scale at $G = 0$, (b) $G = 3$, and (c) $G = 6$. The DMRG result is compared with the probability distribution of the squeezed vacuum state (black crosses). Cavity frequency and the Coulomb interaction are set as $U/W = V/W = 0$ and $\Omega/W = 10$.

The probability to find n_{ph} photons in the ground state is $P(n_{\text{ph}})$. Fig. 3.7 shows the probability distribution for different coupling constant at $U/W = V/W = 0$ and $\Omega/W = 10$. The vacuum state only includes the zero photon states for $G = 0$, whereas the finite photon states appear for a finite G . We observe that even number states contribute significantly, implying that the photon wavefunction approximately has a probability distribution that is compatible with a squeezed vacuum state $|\text{SV}\rangle$, i.e.,

$$|\text{SV}\rangle = \frac{1}{\sqrt{\cosh(\zeta)}} \sum_{n=0}^{\infty} (\tanh(\zeta))^n \frac{\sqrt{(2n)!}}{2^n n!} |2n\rangle. \quad (3.35)$$

$P(n_{\text{ph}})$ agrees with the squeezed vacuum state with the squeezed parameter $\zeta = 1/2 \ln \left(\tilde{\Omega}/\Omega \right)$, indicated by the black crosses in Fig. 3.7. Odd number states have rather small but finite contributions in the calculation. In the periodic boundary condition, the previous study [61] shows that the odd number states disappear due to the zero current fluctuation $\langle \Delta \hat{J}^2 \rangle_{\text{GS}}$. However, the DMRG calculation is performed for the open boundary condition, so that the slight current fluctuation remains. The odd number states appear from the fluctuation.

Fig. 3.8 shows the probability distribution for different Coulomb interactions U, V at $G = 6$. In contrast to the case of $U/W = V/W = 0$, finite U/W and V/W create the odd number states. The probability distribution decreases monotonically as the number of photons increases at $U/W = 10, V/W = 0$ and $U/W = 0, V/W = 5$, which means that the squeezing effect is suppressed due to the small absolute value of the kinetic energy in the SDW and CDW phases. However, when $V \approx U/2$ is satisfied, the kinetic energy increases and the squeezing effect becomes more pronounced. The probability for $n_{\text{ph}} = 2$ states becomes slightly larger than that for $n_{\text{ph}} = 1$ states.

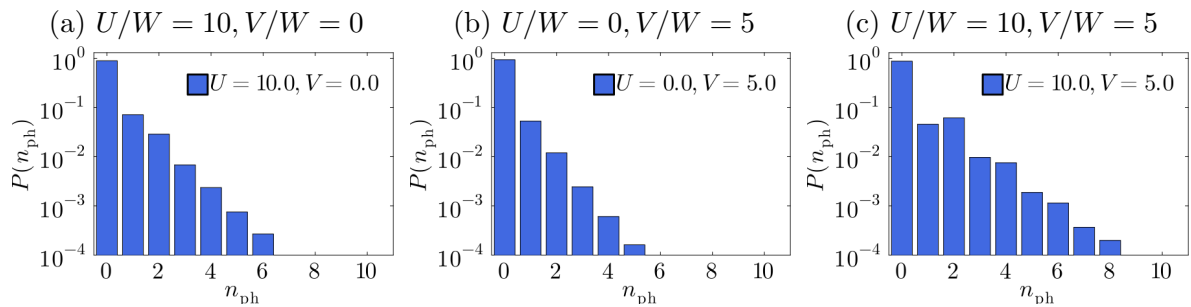


Figure 3.8: DMRG results of the probability distribution $P(n_{\text{ph}})$ in the logarithmic scale with different Coulomb interactions (a) $U/W = 10, V/W = 0$, (b) $U/W = 0, V/W = 5$, and (c) $U/W = 10, V/W = 5$. Cavity frequency and the coupling constant are set as $\Omega/W = 10$ and $G = 6$.

Chapter 4

Excited-State Properties

In this chapter, we present numerical results for the excited states in the 1DEHM coupled with an optical cavity. In the first section, we briefly explain how to calculate two different dynamical response functions: an optical conductivity and a photon spectral function. In the second section, we show the numerical results for the two response functions. The analysis of the numerical results is also included in the section.

4.1 Excited-state calculation

In the linear response theory, an induced current $j(t)$ due to the application of an external probe field $E(t)$ is given by

$$j(t) = \int_{-\infty}^t \sigma(t, t') E(t') dt', \quad (4.1)$$

$$j(\omega) = \sigma(\omega) E(\omega), \quad (4.2)$$

where the response function $\sigma(t, t') = \sigma(t - t')$ is the optical conductivity in the time domain, and $\sigma(\omega)$ is its Fourier transformation. In this study, we apply an external probe field as

$$A(t) = A_p \exp\left(-\frac{(t - t_p)^2}{2\sigma_p^2}\right) \cos(\omega_p(t - t_p)). \quad (4.3)$$

A Gaussian-like envelope around $t = t_p$ is used with the temporal width σ_p of the probe pulse, and ω_p is the central frequency [86–88]. The relation between the electric field E and vector potential A is $E(t) = -\partial A(t)/\partial t$ in the time domain, and $E(\omega) = i\omega A(\omega)$ in the frequency domain. This external field is incorporated via the Peierls substitution in the hopping term as

$$\begin{aligned} \hat{H}(t) &= \Omega \hat{a}^\dagger \hat{a} - W \sum_{j,\sigma} (e^{i \frac{G}{\sqrt{N}} (\hat{a} + \hat{a}^\dagger) + iA(t)} \hat{c}_{j,\sigma}^\dagger \hat{c}_{j+1,\sigma} + \text{h.c.}) \\ &\quad + U \sum_j \hat{n}_{j,\uparrow} \hat{n}_{j,\downarrow} + V \sum_j \hat{n}_j \hat{n}_{j+1}. \end{aligned} \quad (4.4)$$

With the knowledge of the wavefunction $|\Psi(t)\rangle$ under the action of $A(t)$, we can obtain the temporal evolution of the expectation value of the current operator $j(t) = J(t)/N = \langle\Psi(t)|\hat{J}(t)|\Psi(t)\rangle/N$. Note that the current operator becomes time-dependent in the presence of $A(t)$:

$$\hat{J}(t) = \frac{\delta\hat{H}(t)}{\delta A(t)} = -Wi \sum_j (e^{i\frac{G}{\sqrt{N}}(\hat{a}+\hat{a}^\dagger)+iA(t)} \hat{c}_{j,\sigma}^\dagger \hat{c}_{j+1,\sigma} - \text{h.c.}). \quad (4.5)$$

Here, we calculate the time-dependent wave function with the TEBD method starting from the ground state, which is calculated with the DMRG method. Based on Eq. (4.2), the optical conductivity can be calculated by

$$\sigma(\omega) = \frac{j(\omega)}{E(\omega)} = \frac{J(\omega)}{i(\omega + i\eta)NA(\omega)}, \quad (4.6)$$

where $J(\omega)$ and $A(\omega)$ are the Fourier transform of $J(t)$ and $A(t)$, respectively. Note that a damping factor $e^{-\eta t}$ is introduced in numerical calculations when the Fourier transformations are performed. $\sigma(\omega)$ reflects the property of the system in equilibrium, and does not depend on the details of the probe field. It is well known that $\sigma(\omega)$ can be calculated microscopically from the current-current correlations through the Kubo formula. The regular part (except for a possible singularity at $\omega = 0$) is given as

$$\begin{aligned} \sigma_{\text{reg}}(\omega) &= \frac{1}{\omega N} \int_0^\infty dt e^{i\omega t - \eta t} \langle \Psi_{\text{GS}} | [\hat{J}_H(t), \hat{J}_H(0)] | \Psi_{\text{GS}} \rangle \\ &= \frac{i}{\omega N} \sum_m \left(\frac{|\langle \Psi_m | \hat{J} | \Psi_{\text{GS}} \rangle|^2}{\omega + E_{\text{GS}} - E_m + i\eta} - \frac{|\langle \Psi_m | \hat{J} | \Psi_{\text{GS}} \rangle|^2}{\omega - E_{\text{GS}} + E_m + i\eta} \right), \end{aligned} \quad (4.7)$$

where $|\Psi_m\rangle$ ($|\Psi_{\text{GS}}\rangle$) and E_m (E_{GS}) are the excited states (ground state) and their energies. $\hat{J}_H(t) := e^{i\hat{H}t} \hat{J} e^{-i\hat{H}t}$ is the current operator ($\hat{J} := \hat{J}(t=0)$) in the Heisenberg picture. The real part of the optical conductivity represents the excited state energy induced by the current fluctuation, i.e.,

$$\text{Re}(\sigma_{\text{reg}}(\omega)) \xrightarrow{\eta \rightarrow 0} \frac{\pi}{\omega N} \sum_m |\langle \Psi_m | \hat{J} | \Psi_{\text{GS}} \rangle|^2 (\delta(\omega - E_m + E_{\text{GS}}) - \delta(\omega + E_m - E_{\text{GS}})). \quad (4.8)$$

The polaritons are the light-matter hybrid quasiparticles. The real part of the optical conductivity can detect its matter component, while the photon spectral function can detect its light component. We can define the photon spectral function $S(\omega)$ using the photon retarded Green's function $G^R(t)$, which is defined as

$$\begin{aligned} G^R(t) &= -i\theta(t) \langle \Psi_{\text{GS}} | [\hat{a}_H(t), \hat{a}_H^\dagger(0)] | \Psi_{\text{GS}} \rangle, \\ G^R(\omega) &= \int_{-\infty}^\infty e^{i\omega t - \eta t} G(t) \\ &= -i \int_0^\infty dt e^{i\omega t - \eta t} \langle \Psi_{\text{GS}} | [\hat{a}_H(t), \hat{a}_H^\dagger(0)] | \Psi_{\text{GS}} \rangle \end{aligned} \quad (4.9)$$

$$= \sum_m \left(\frac{|\langle \Psi_m | \hat{a}^\dagger | \Psi_{\text{GS}} \rangle|^2}{\omega + E_{\text{GS}} - E_m + i\eta} - \frac{|\langle \Psi_m | \hat{a} | \Psi_{\text{GS}} \rangle|^2}{\omega - E_{\text{GS}} + E_m + i\eta} \right). \quad (4.10)$$

Then, the photon spectral function is given by the imaginary part of the photon retarded Green's function as

$$\begin{aligned} S(\omega) &= -\text{Im}(G^R(\omega)) \\ &\xrightarrow{\eta \rightarrow 0} \pi \sum_m |\langle \Psi_m | \hat{a}^\dagger | \Psi_{\text{GS}} \rangle|^2 \delta(\omega - E_m + E_{\text{GS}}) \\ &\quad - \pi \sum_m |\langle \Psi_m | \hat{a} | \Psi_{\text{GS}} \rangle|^2 \delta(\omega + E_m - E_{\text{GS}}). \end{aligned} \quad (4.11)$$

The photon spectral function represents the excited state energy induced by the photon creation and annihilation. Here, we directly calculate the photon retarded Green's function from Eq. (4.9) using the TEBD method.

Numerical calculations are performed for the number of electrons $N = 40$ at half-filling. In the time evolution calculations, we set the time step to $\delta t = 0.01$, the total time to $T = 100$, and the bond dimensions to $\chi_{\max} = 400$, respectively. The parameter of the probe field in Eq. (4.3) is set to be $A_p = 0.01$, $t_p = 1.0$, $\sigma_p = 0.02$, and $\omega_p = 10.0$, respectively. Due to the high computational cost, we use the photon cutoff as $N_{\max} = 1$, which means that only one photon exchange processes are considered in the calculations. The convergence checks are performed in Appendix A.

4.2 Optical conductivity and photon spectral function

Fig. 4.1 shows the real part of the optical conductivity and the photon spectral function with different nearest-neighbor interactions $V/W = 0$, 3.5 and 7.5 at $G = 0.5$. The cavity frequency is chosen as the peak position of the optical conductivity without a cavity. For $V/W = 0$, we choose $\Omega/W = 10$ as the center position of the optical conductivity.

We can see the spectral splitting in the optical conductivity and the photon spectral function for $V/W = 3.5$ and 7.5 (Fig. 4.1 (c), (d), (e), and (f)). The splittings are considered as the vacuum Rabi splitting. In contrast, the photon spectral function does not show splitting for $V/W = 0$ regardless of the splitting of the optical conductivity (Fig. 4.1 (a) and (b)). The spectral splitting of the optical conductivity for $V/W = 0$ is consistent with the previous exact diagonalization study [89]. The photon spectral function becomes broadened, and its signal center is slightly shifted due to the coupling between photons and electrons in the 1DEHM.

4.2.1 Vacuum Rabi splitting

The sharp peak without a cavity in the case of $V/W = 3.5$ and 7.5 corresponds to the energy of the excitons in the SDW phase and the dissociation energy of doublons in the CDW phase, respectively, as seen in Sect. 1.3.1. The cavity photons couple with these excitations and form the polaritons. The polaritons have both the matter and light components, so we can observe their signal in both the optical conductivity and photon spectral function. In order to analytically understand the splitting behavior, we take some

approximations in the following. First, we only focus on the Hilbert space composed of the 1DEHM excited states with no photon $|\phi_a\rangle|0\rangle$ ($a \neq 0$) and the 1DEHM ground state with a single photon $|\phi_0\rangle|1\rangle$. Second, we consider the first-order expansion of the Peierls phase due to the small coupling constant $G = 0.5$. Third, we approximate the ground state as the product state of the 1DEHM ground state and no photon state $|\Psi_{\text{GS}}\rangle = |\phi_0\rangle|0\rangle$. Under these approximations, we can write the photon retarded Green's function as

$$\begin{aligned} G^R(\omega) &= \langle \Psi_{\text{GS}} | \hat{a} \hat{G}^R(\omega) \hat{a}^\dagger | \Psi_{\text{GS}} \rangle \\ &= \langle 1 | \langle \phi_0 | \hat{G}^R(\omega) | \phi_0 \rangle | 1 \rangle, \end{aligned} \quad (4.12)$$

where $\hat{G}^R(\omega)$ is the matrix form of the retarded Green's function defined as

$$\begin{aligned} \hat{G}^R(\omega) &= \frac{1}{\omega - \hat{H} + E_0 + i\eta}, \\ \hat{H} &= \Omega \hat{a}^\dagger \hat{a} + \hat{H}_{\text{1DEHM}} + \frac{G}{\sqrt{N}} \hat{J}(\hat{a}^\dagger + \hat{a}). \end{aligned} \quad (4.13)$$

Here, \hat{H}_{1DEHM} and E_0 is the Hamiltonian and the ground state energy of 1DEHM, respectively. In order to evaluate Eq. (4.12), we first consider the inverse of the matrix retarded Green's function in the bases of $|\phi_0\rangle|1\rangle$ and $|\phi_a\rangle|0\rangle$ ($a \neq 0$):

$$\hat{G}^R(\omega)^{-1} = \begin{pmatrix} \omega + i\eta - \Omega & \frac{G_1}{\sqrt{N}} & \frac{G_2}{\sqrt{N}} & \dots \\ \frac{G_1}{\sqrt{N}} & \omega + i\eta - \Delta E_{10} & 0 & \dots \\ \frac{G_2}{\sqrt{N}} & 0 & \omega + i\eta - \Delta E_{20} & \dots \\ \vdots & \vdots & \vdots & \ddots \end{pmatrix}, \quad (4.14)$$

where $G_a = G \langle 0 | \hat{a} | 1 \rangle \langle \phi_a | \hat{J} | \phi_0 \rangle$ is the coupling strength between $|\phi_0\rangle|1\rangle$ and $|\phi_a\rangle|0\rangle$ ($a \neq 0$), and $\Delta E_{a0} = E_a - E_0$ is the energy differences between the excited states and ground state in the 1DEHM. By finding the (1,1) component, we can obtain information about the photon retarded Green's function. Therefore, we use the cofactor expansion to find the (1,1) component of the inverse matrix as

$$G^R(\omega) = \frac{1}{\omega + i\eta - \Omega + \Delta^R(\omega)}, \quad (4.15)$$

$$\Delta^R(\omega) = -\frac{1}{N} \sum_a \frac{|G_a|^2}{\omega + i\eta - \Delta E_{a0}}. \quad (4.16)$$

If the excited energy of 1DEHM induced by the current can be considered as a single energy $\Delta E_{a0} \approx \Delta E$, $\Delta^R(\omega)$ becomes simplified as

$$\begin{aligned} \Delta^R(\omega) &= -\frac{1}{N} \sum_a \frac{G^2 |\langle \phi_a | \hat{J} | \phi_0 \rangle|^2}{\omega + i\eta - \Delta E} \\ &= -\frac{G_{\text{eff}}^2}{\omega + i\eta - \Delta E}, \end{aligned} \quad (4.17)$$

where $G_{\text{eff}} = G\sqrt{\langle \Delta J^2 \rangle_{\text{GS}} / N}$ is the effective coupling strength. We find the photon retarded Green's function has two poles as

$$\begin{aligned} G^R(\omega) &= \frac{1}{\omega + i\eta - \Omega - \frac{G_{\text{eff}}^2}{\omega + i\eta - \Delta E}} \\ &= \frac{\omega + i\eta - \Delta E}{(\omega + i\eta - E_+)(\omega + i\eta - E_-)}, \end{aligned} \quad (4.18)$$

$$E_{\pm} = \frac{\Omega + \Delta E}{2} \pm \sqrt{\delta^2 + G_{\text{eff}}^2}, \quad (4.19)$$

$$\delta = \frac{\Omega - \Delta E}{2}, \quad (4.20)$$

$$S(\omega) \xrightarrow{\eta \rightarrow 0} \pi \frac{\sqrt{\delta^2 + G_{\text{eff}}^2} + \delta}{2\sqrt{\delta^2 + G_{\text{eff}}^2}} \delta(\omega - E_+) + \pi \frac{\sqrt{\delta^2 + G_{\text{eff}}^2} - \delta}{2\sqrt{\delta^2 + G_{\text{eff}}^2}} \delta(\omega - E_-). \quad (4.21)$$

The position of the two poles E_{\pm} is nothing but the polariton energy as seen in the Hopfield model in Eq. (1.8). However, the coupling strength is determined by the current fluctuation of the electron system. Fig. 4.2 shows the cavity frequency dependence of the vacuum Rabi splitting. The analytical expression of the peak position E_{\pm} and the TEBD calculation qualitatively agree.

4.2.2 Spectral broadening

In order to analytically understand the spectral broadening for $V/W = 0$, we consider the situation that the excitation energy cannot be regarded as the single energy ΔE . When the width of the excitation energy is much larger than the region of the frequency space being considered, the ω dependence of the $\Delta^R(\omega)$ can be neglected as $\Delta^R(\omega) \sim \Delta_0 + i\Delta_1$. Δ_0 and Δ_1 is the real and imaginary parts of $\Delta^R(\omega)$. The photon spectral function becomes the Lorentzian, i.e.,

$$\begin{aligned} G^R(\omega) &= \frac{1}{\omega + i\eta - \Omega + \Delta_0 + i\Delta_0} \\ &= \frac{\omega - \Omega + \Delta_0 - i\Delta_1}{(\omega - \Omega + \Delta_0)^2 + \Delta_1^2}, \end{aligned} \quad (4.22)$$

$$S(\omega) = \frac{\Delta_1}{(\omega - \Omega + \Delta_0)^2 + \Delta_1^2} =: S(\omega, \Omega, \Delta_0, \Delta_1). \quad (4.23)$$

Fig. 4.3 shows the result of fitting the spectral data obtained by TEBD with a Lorentzian. We find that the Lorentzian explains the spectral broadening and the shift of the spectral center well.

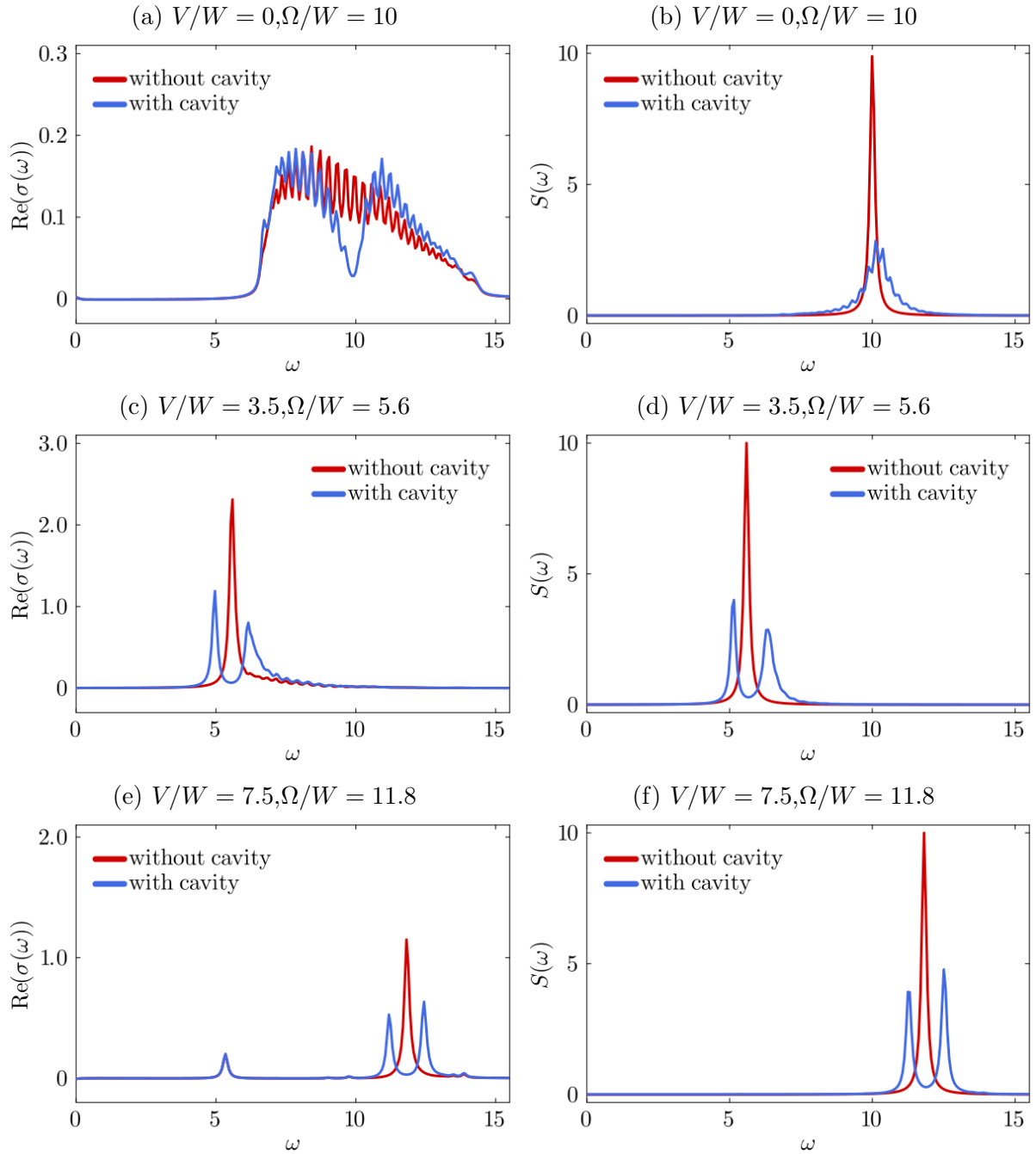


Figure 4.1: Real part of the optical conductivity $\text{Re}(\sigma(\omega))$ ((a), (c), (e)) and photon spectral function $S(\omega)$ ((b), (d), (f)) with different nearest-neighbor interactions $V/W = 0, 3.5$, and 7.5 (blue lines). The cavity frequency is $\Omega/W = 10, 5.6, 11.8$. We set the other parameters to $U/W = 10$ and $G = 0.5$. The results without a cavity are also shown by red lines.

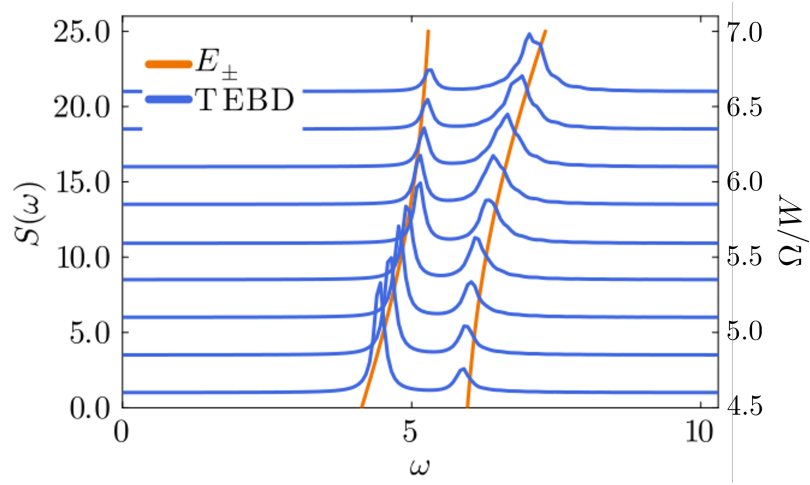


Figure 4.2: The photon spectral function for various Ω/W (blue lines) are compared with E_{\pm} (orange lines). The other parameters are set to $U/W = 10$, $V/W = 3.5$, $G = 0.5$. We set the energy difference in E_{\pm} to $\Delta E = 5.6$.

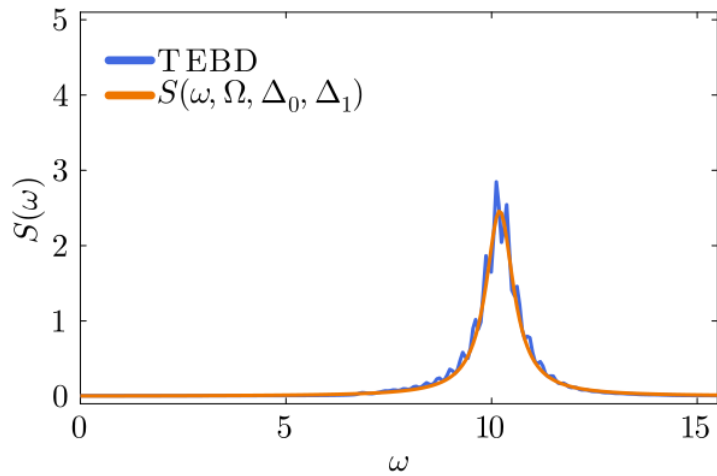


Figure 4.3: The photon spectral function for $V/W = 0$, $U/W = \Omega/W = 10$ and $G = 0.5$ (blue line) is compared with $S(\omega, \Omega, \Delta_0, \Delta_1)$ (orange line). Fitting parameters are $\Delta_0 = -0.196$ and $\Delta_1 = 0.406$.

Chapter 5

Conclusion and Outlook

5.1 Summary

In this thesis, we study the 1DEHM coupled with an optical cavity by numerical calculations. We focus on two aspects: the virtual photons in the ground state and vacuum Rabi splitting in the excited states.

We find that the photon number in the ground state changes depending on the Coulomb interaction in the 1DEHM. The Coulomb interaction dependence is qualitatively different between the small and large coupling constants. From the perturbation and squeezed transformation analyses, we clarify that the photon number is crucially determined by both the counter-rotating and squeezing processes, which have to do with the current fluctuation and absolute value of the kinetic energy of the electron system, respectively. In relation to the photon number, we also investigate the virtual photon squeezing by calculating the variance of the canonical momentum and coordinate operator. We find that the squeezing is enhanced, and the product of both variances is suppressed along the line $V = U/2$ due to the large absolute value of the kinetic energy and small current fluctuation in the electron system.

We also study the vacuum Rabi splitting by calculating the optical conductivity and the photon spectral function. We find that both quantities show vacuum Rabi splitting when the width of the charge excitation energy is narrow. However, when the electron charge excitation energy has a wide width, the photon spectral function shows spectral broadening. We clarify that both the Rabi splitting and the spectral broadening can be explained by the analysis of the photon retarded Green's function.

5.2 Future directions

As for the future directions of this study, we have the following ideas.

5.2.1 Magnetic coupling

In this study, the electric properties of the 1DEHM, such as the current fluctuation, the kinetic energy, and the charge excitation energy, are reflected in the virtual photons and

the Rabi splitting. However, the magnetic properties of the 1DEHM are not reflected in these quantities. Applying the classical magnetic field may change the photon number and Rabi splitting behavior reflecting the magnetic structure, as seen in the Landau polariton system [12, 23, 35]. There is also the theoretical study of Rashba and Zeeman couplings at the quantum level [90–92]. Therefore, including the Rashba and Zeeman coupling into the 1DEHM coupled with an optical cavity is an important future direction.

5.2.2 Exciton polariton condensate

In Chap. 4, we have shown the results on the vacuum Rabi splitting for $V/W = 3.5$. This indicates the formation of exciton-polaritons. In semiconductors, exciton-polaritons have been studied intensively because the exciton-polaritons can show Bose-Einstein condensation (BEC). Exciton-polariton condensation is easier to be achieved than exciton condensation due to the light effective mass and strong nonlinearity [37, 93]. Therefore, exciton-polariton condensation has a high critical temperature and low threshold of the pump field. The binding between holes and electrons forms semiconductor excitons. However, excitons in Mott insulators are the bound state of doublons and holons. Therefore, the exciton-polaritons in the Mott insulator may be new quasiparticles, which have the possibility of realizing BEC.

5.2.3 Superradiant phase transition

In this study, we mainly focus on the physical quantities of the cavity photons. The reason is that we only consider a single cavity mode and collective coupling strength. Due to the no-go theorem of superradiant phase transition (SRPT) [63–67], there is no macroscopic photon condensation, i.e., $|\langle \hat{a}^\dagger \hat{a} \rangle|/N \rightarrow 0$. The contribution from the cavity photon to materials is relatively small, as seen in the discussion in Sect. 2.1.2. However, the statement of the no-go theorem can only be applied to equilibrium, and the possibility of photon condensation through the same mechanism as SRPT in non-equilibrium is not prohibited. Indeed, recent ultracold atom experiments show the SRPT [94, 95] based on the combination of the classical pump field and quantized cavity field [96, 97]. Thus, investigating the SRPT in quantum materials [98] is an important topic from the perspective of cavity quantum materials. Establishing the phase diagram of the 1DEHM with SRPT could be an interesting future direction.

Appendix A

Numerical Convergence

Here, we report convergence checks for the DMRG results.

In the DMRG calculation, we set two parameters to the limit of the accuracy of our numerical approximation, which are the maximum bond dimension χ_{\max} and the photon cutoff N_{\max} . The maximum bond dimension χ_{\max} defines the maximum dimension of the matrices in the MPS representation of the ground state. The photon cutoff sets the dimension of the local Hilbert space that describes the bosonic degree of freedom, which we consider to be finite. The plots in Fig. A.1 have been obtained by simulating the system of size $N = 80$ for $U/W = V/W = 0$, $\Omega/W = 10$ and $G = 6$, which is the largest coupling constants considered in this thesis. At $G = 6$, the photon number and the degree of squeezing reach their maximum at $U/W = V/W = 0$, so the convergence is verified at this value. We show the convergence behavior for three significant quantities discussed in the main text, N_{ph} , ΔP , and ΔX . Unless otherwise stated, the DMRG parameters for the results shown in the main text are $\chi_{\max} = 1600$ and $N_{\max} = 20$.

In the TEBD calculation, we also check the convergence in terms of the maximum bond dimension and the photon cutoff. During the time evolution, we keep the maximum bond dimension at χ_{\max} . We set a relatively small coupling constant $G = 0.5$ in the TEBD calculations, so that the necessary photon cutoff can be kept small. The plots in Fig. A.2 have been obtained by simulating the system of size $N = 40$ for $U/W = V/W = 0$, $\Omega/W = 10$ and $G = 0.5$. Due to the high numerical cost of the TEBD calculation, we performed the calculations with the maximum bond dimension up to 500 and the photon cutoff up to 2. We show the convergence behavior for the real part of the optical conductivity $\text{Re}(\sigma(\omega))$ and the photon spectral function $S(\omega)$. Unless otherwise stated, the TEBD parameters for the results shown in the main text are $\chi_{\max} = 400$ and $N_{\max} = 1$.

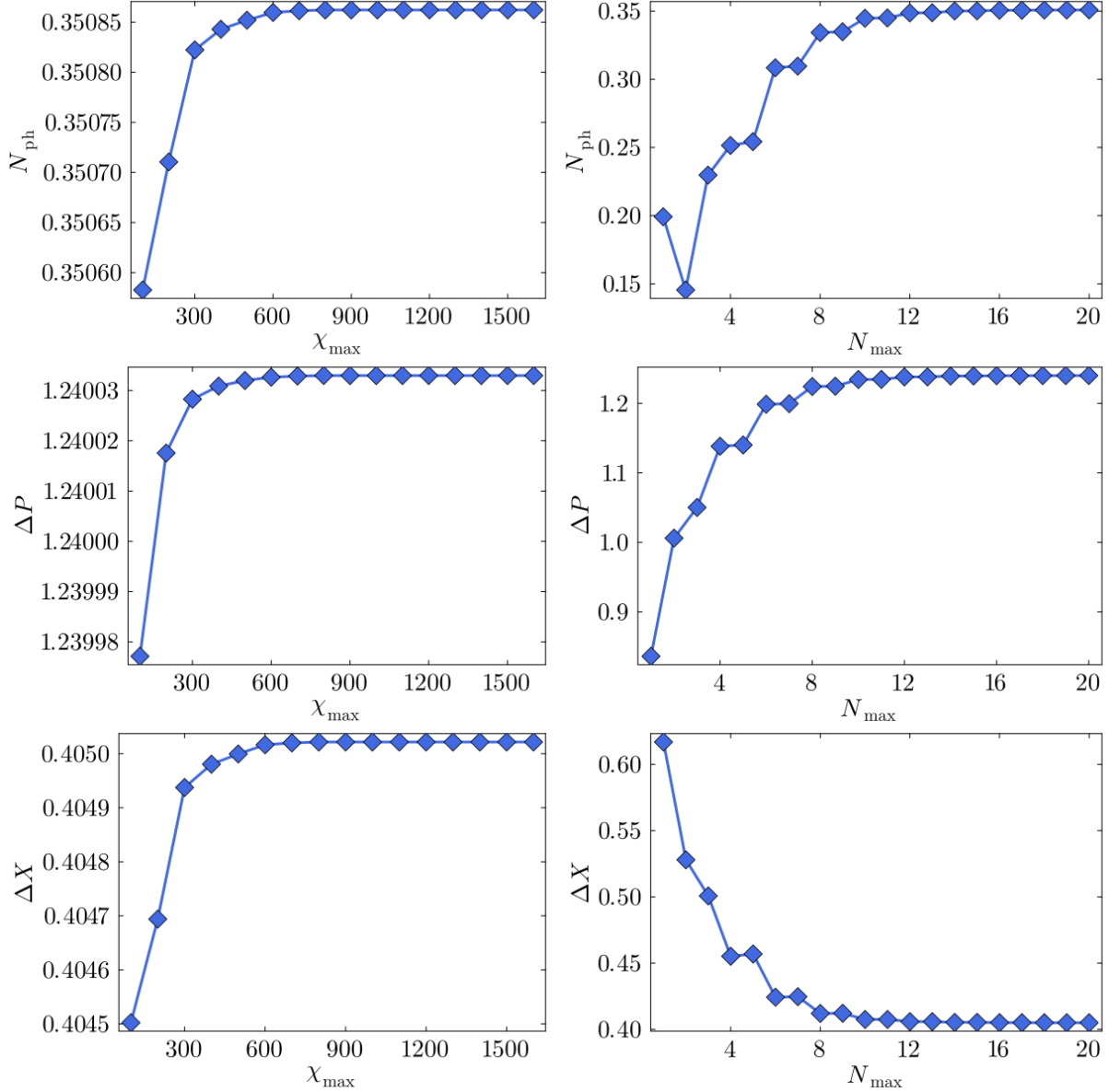


Figure A.1: Convergence analysis for the relevant quantities N_{ph} , ΔP , and ΔX . All the curves have been obtained by setting $N = 80$, $U/W = V/W = 0$, $\Omega/W = 10$, $G = 6$.

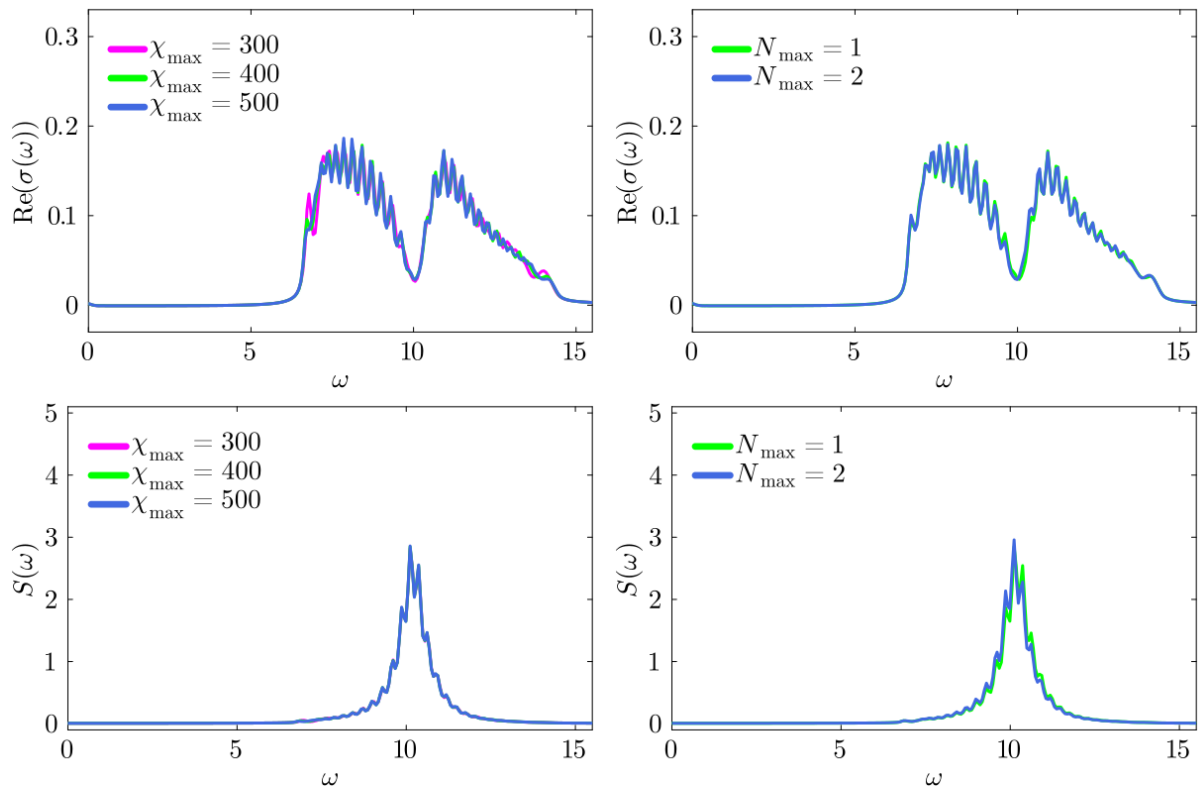


Figure A.2: Convergence analysis for the relevant quantities $\text{Re}(\sigma(\omega))$, $S(\omega)$. All the curves have been obtained by setting $N = 40$, $U/W = V/W = 0$, $\Omega/W = 10$, $G = 0.5$.

Bibliography

- [1] E. M. Purcell, Phys. Rev. **69**, 681 (1946).
- [2] S. Haroche and D. Kleppner, Physics Today **42**, 24 (1989).
- [3] P. Forn-Díaz, L. Lamata, E. Rico, J. Kono, and E. Solano, Rev. Mod. Phys. **91**, 025005 (2019).
- [4] A. Frisk Kockum, A. Miranowicz, S. De Liberato, S. Savasta, and F. Nori, Nat Rev Phys **1**, 19 (2019).
- [5] E. Mavrona, S. Rajabali, F. Appugliese, J. Andberger, M. Beck, G. Scalari, and J. Faist, ACS Photonics **8**, 2692 (2021).
- [6] G. Scalari, C. Maissen, D. Turčinková, D. Hagenmüller, S. De Liberato, C. Ciuti, C. Reichl, D. Schuh, W. Wegscheider, M. Beck, and J. Faist, Science **335**, 1323 (2012).
- [7] J. J. Baumberg, J. Aizpurua, M. H. Mikkelsen, and D. R. Smith, Nat. Mater. **18**, 668 (2019).
- [8] P. Sivarajah, A. Steinbacher, B. Dastrup, J. Lu, M. Xiang, W. Ren, S. Kamba, S. Cao, and K. A. Nelson, Journal of Applied Physics **125**, 213103 (2019).
- [9] Q. Zhang, M. Lou, X. Li, J. L. Reno, W. Pan, J. D. Watson, M. J. Manfra, and J. Kono, Nature Phys **12**, 1005 (2016).
- [10] F. Yoshihara, T. Fuse, S. Ashhab, K. Kakuyanagi, S. Saito, and K. Semba, Nature Phys **13**, 44 (2017).
- [11] A. A. Anappara, S. De Liberato, A. Tredicucci, C. Ciuti, G. Biasiol, L. Sorba, and F. Beltram, Phys. Rev. B **79**, 201303 (2009).
- [12] A. Bayer, M. Pozimski, S. Schambeck, D. Schuh, R. Huber, D. Bougeard, and C. Lange, Nano Lett. **17**, 6340 (2017).
- [13] F. Barachati, J. Simon, Y. A. Getmanenko, S. Barlow, S. R. Marder, and S. Kéna-Cohen, ACS Photonics **5**, 119 (2018).
- [14] D. Zhang, X.-Q. Luo, Y.-P. Wang, T.-F. Li, and J. Q. You, Nat Commun **8**, 1368 (2017).

- [15] I. I. Rabi, *Phys. Rev.* **51**, 652 (1937).
- [16] R. H. Dicke, *Phys. Rev.* **93**, 99 (1954).
- [17] J. J. Hopfield, *Phys. Rev.* **112**, 1555 (1958).
- [18] S. Ghosh and T. C. H. Liew, *npj Quantum Inf* **6**, 1 (2020).
- [19] F. I. Moxley, E. O. Ilo-Okeke, S. Mudaliar, and T. Byrnes, *emergent mater.* **4**, 971 (2021).
- [20] C. R. Gubbin, S. De Liberato, and T. G. Folland, *Journal of Applied Physics* **131**, 030901 (2022).
- [21] F. Bloch and A. Siegert, *Phys. Rev.* **57**, 522 (1940).
- [22] P. Forn-Díaz, J. Lisenfeld, D. Marcos, J. J. García-Ripoll, E. Solano, C. J. P. M. Harmans, and J. E. Mooij, *Phys. Rev. Lett.* **105**, 237001 (2010).
- [23] X. Li, M. Bamba, Q. Zhang, S. Fallahi, G. C. Gardner, W. Gao, M. Lou, K. Yoshioka, M. J. Manfra, and J. Kono, *Nature Photon* **12**, 324 (2018).
- [24] C. Ciuti, G. Bastard, and I. Carusotto, *Phys. Rev. B* **72**, 115303 (2005).
- [25] S. Ashhab and F. Nori, *Phys. Rev. A* **81**, 042311 (2010).
- [26] R. Stassi, A. Ridolfo, O. Di Stefano, M. J. Hartmann, and S. Savasta, *Phys. Rev. Lett.* **110**, 243601 (2013).
- [27] T. Oka and S. Kitamura, *Annual Review of Condensed Matter Physics* **10**, 387 (2019).
- [28] N. Tsuji (2024) pp. 967–980.
- [29] A. S. Disa, T. F. Nova, and A. Cavalleri, *Nat. Phys.* **17**, 1087 (2021).
- [30] A. de la Torre, D. M. Kennes, M. Claassen, S. Gerber, J. W. McIver, and M. A. Sentef, *Rev. Mod. Phys.* **93**, 041002 (2021).
- [31] F. Schlawin, D. M. Kennes, and M. A. Sentef, *Applied Physics Reviews* **9**, 011312 (2022).
- [32] F. J. Garcia-Vidal, C. Ciuti, and T. W. Ebbesen, *Science* **373**, eabd0336 (2021).
- [33] J. Bloch, A. Cavalleri, V. Galitski, M. Hafezi, and A. Rubio, *Nature* **606**, 41 (2022).
- [34] E. Orgiu, J. George, J. A. Hutchison, E. Devaux, J. F. Dayen, B. Doudin, F. Stellacci, C. Genet, J. Schachenmayer, C. Genes, G. Pupillo, P. Samorì, and T. W. Ebbesen, *Nature Mater* **14**, 1123 (2015).
- [35] G. L. Paravicini-Bagliani, F. Appugliese, E. Richter, F. Valmorra, J. Keller, M. Beck, N. Bartolo, C. Rössler, T. Ihn, K. Ensslin, C. Ciuti, G. Scalari, and J. Faist, *Nature Phys* **15**, 186 (2019).

Bibliography

- [36] F. Appugliese, J. Enkner, G. L. Paravicini-Bagliani, M. Beck, C. Reichl, W. Wegscheider, G. Scalari, C. Ciuti, and J. Faist, *Science* **375**, 1030 (2022).
- [37] H. Deng, H. Haug, and Y. Yamamoto, *Rev. Mod. Phys.* **82**, 1489 (2010).
- [38] G. Jarc, S. Y. Mathengattil, A. Montanaro, F. Giusti, E. M. Rigoni, R. Sergo, F. Fasioli, S. Winnerl, S. Dal Zilio, D. Mihailovic, P. Prelovšek, M. Eckstein, and D. Fausti, *Nature* **622**, 487 (2023).
- [39] A. Thomas, E. Devaux, K. Nagarajan, T. Chervy, M. Seidel, D. Hagenmüller, S. Schütz, J. Schachenmayer, C. Genet, G. Pupillo, and T. W. Ebbesen, *Exploring Superconductivity under Strong Coupling with the Vacuum Electromagnetic Field* (2019).
- [40] F. Schlawin, A. Cavalleri, and D. Jaksch, *Phys. Rev. Lett.* **122**, 133602 (2019).
- [41] Y. Ashida, A. İmamoğlu, J. Faist, D. Jaksch, A. Cavalleri, and E. Demler, *Phys. Rev. X* **10**, 041027 (2020).
- [42] K. Masuki and Y. Ashida, *Phys. Rev. B* **109**, 195173 (2024).
- [43] C. Ciuti, *Phys. Rev. B* **104**, 155307 (2021).
- [44] X. Wang, E. Ronca, and M. A. Sentef, *Phys. Rev. B* **99**, 235156 (2019).
- [45] M. A. Sentef, J. Li, F. Künzel, and M. Eckstein, *Phys. Rev. Res.* **2**, 033033 (2020).
- [46] S. Ejima and S. Nishimoto, *Phys. Rev. Lett.* **99**, 216403 (2007).
- [47] M. Nakamura, *Phys. Rev. B* **61**, 16377 (2000).
- [48] K. Sugimoto and S. Ejima, *Phys. Rev. B* **108**, 195128 (2023).
- [49] E. Jeckelmann, *Phys. Rev. B* **67**, 075106 (2003).
- [50] F. H. L. Essler, F. Gebhard, and E. Jeckelmann, *Phys. Rev. B* **64**, 125119 (2001).
- [51] T. Yamaguchi, K. Iwano, T. Miyamoto, N. Takamura, N. Kida, Y. Takahashi, T. Hasegawa, and H. Okamoto, *Phys. Rev. B* **103**, 045124 (2021).
- [52] S. R. White, *Phys. Rev. Lett.* **69**, 2863 (1992).
- [53] S. R. White, *Phys. Rev. B* **48**, 10345 (1993).
- [54] E. Jeckelmann, *Phys. Rev. B* **66**, 045114 (2002).
- [55] G. Vidal, *Phys. Rev. Lett.* **93**, 040502 (2004).
- [56] T. Hasegawa, S. Kagoshima, T. Mochida, S. Sugiura, and Y. Iwasa, *Solid State Communications* **103**, 489 (1997).

- [57] T. Hasegawa, T. Mochida, R. Kondo, S. Kagoshima, Y. Iwasa, T. Akutagawa, T. Nakamura, and G. Saito, [Phys. Rev. B **62**, 10059 \(2000\)](#).
- [58] M. Ono, H. Kishida, and H. Okamoto, [Phys. Rev. Lett. **95**, 087401 \(2005\)](#).
- [59] S. Iwai, M. Ono, A. Maeda, H. Matsuzaki, H. Kishida, H. Okamoto, and Y. Tokura, [Phys. Rev. Lett. **91**, 057401 \(2003\)](#).
- [60] O. Dmytruk and M. Schiró, [Phys. Rev. B **103**, 075131 \(2021\)](#), publisher: American Physical Society.
- [61] C. J. Eckhardt, G. Passetti, M. Othman, C. Karrasch, F. Cavaliere, M. A. Sentef, and D. M. Kennes, [Commun Phys **5**, 1 \(2022\)](#).
- [62] K. Hepp and E. H. Lieb, [Phys. Rev. A **8**, 2517 \(1973\)](#).
- [63] K. Rzazewski, K. Wodkiewicz, and W. Zakowicz, [Phys. Rev. Lett. **35**, 432 \(1975\)](#).
- [64] K. Gawedzki and K. Rzazewski, [Phys. Rev. A **23**, 2134 \(1981\)](#).
- [65] M. Bamba and T. Ogawa, [Phys. Rev. A **90**, 063825 \(2014\)](#).
- [66] G. M. Andolina, F. M. D. Pellegrino, V. Giovannetti, A. H. MacDonald, and M. Polini, [Phys. Rev. B **100**, 121109 \(2019\)](#).
- [67] G. M. Andolina, F. M. D. Pellegrino, A. Mercurio, O. Di Stefano, M. Polini, and S. Savasta, [Eur. Phys. J. Plus **137**, 1348 \(2022\)](#).
- [68] J. Eisert, M. Cramer, and M. B. Plenio, [Rev. Mod. Phys. **82**, 277 \(2010\)](#).
- [69] M. Fishman, S. White, and E. M. Stoudenmire, [SciPost Physics Codebases , 004 \(2022\)](#).
- [70] U. Schollwöck, [Annals of Physics January 2011 Special Issue, **326**, 96 \(2011\)](#).
- [71] Z. Bacciconi, G. M. Andolina, T. Chanda, G. Chiriacò, M. Schirò, and M. Dalmonte, [SciPost Physics **15**, 113 \(2023\)](#).
- [72] G. Chiriacò, M. Dalmonte, and T. Chanda, [Phys. Rev. B **106**, 155113 \(2022\)](#).
- [73] G. Passetti, C. J. Eckhardt, M. A. Sentef, and D. M. Kennes, [Phys. Rev. Lett. **131**, 023601 \(2023\)](#).
- [74] K. E. Cahill and R. J. Glauber, [Phys. Rev. **177**, 1857 \(1969\)](#).
- [75] M. Suzuki, [Commun.Math. Phys. **51**, 183 \(1976\)](#).
- [76] E. M. Stoudenmire and S. R. White, [New J. Phys. **12**, 055026 \(2010\)](#).
- [77] M. L. Wall, A. Safavi-Naini, and A. M. Rey, [Phys. Rev. A **94**, 053637 \(2016\)](#).

Bibliography

- [78] M. L. Wall, A. Safavi-Naini, and A. M. Rey, *Phys. Rev. A* **95**, 013602 (2017).
- [79] C.-M. Halati, A. Sheikhan, and C. Kollath, *Phys. Rev. Res.* **2**, 043255 (2020).
- [80] C.-M. Halati, A. Sheikhan, H. Ritsch, and C. Kollath, *Phys. Rev. Lett.* **125**, 093604 (2020).
- [81] A. V. Bezvershenko, C.-M. Halati, A. Sheikhan, C. Kollath, and A. Rosch, *Phys. Rev. Lett.* **127**, 173606 (2021).
- [82] C.-M. Halati, A. Sheikhan, and C. Kollath, *Phys. Rev. Res.* **4**, L012015 (2022).
- [83] Y. Ashida, A. İmamoğlu, and E. Demler, *Phys. Rev. Lett.* **126**, 153603 (2021).
- [84] K. Masuki and Y. Ashida, *Phys. Rev. B* **107**, 195104 (2023).
- [85] J. Mochida and Y. Ashida, *Phys. Rev. B* **110**, 035158 (2024).
- [86] H. Lu, S. Sota, H. Matsueda, J. Bonča, and T. Tohyama, *Phys. Rev. Lett.* **109**, 197401 (2012).
- [87] J. Rincón, K. A. Al-Hassanieh, A. E. Feiguin, and E. Dagotto, *Phys. Rev. B* **90**, 155112 (2014).
- [88] C. Shao, T. Tohyama, H.-G. Luo, and H. Lu, *Phys. Rev. B* **93**, 195144 (2016).
- [89] M. Kiffner, J. Coulthard, F. Schlawin, A. Ardavan, and D. Jaksch, *New J. Phys.* **21**, 073066 (2019).
- [90] G. M. Andolina, F. M. D. Pellegrino, V. Giovannetti, A. H. MacDonald, and M. Polini, *Phys. Rev. B* **102**, 125137 (2020).
- [91] J. Román-Roche, F. Luis, and D. Zueco, *Phys. Rev. Lett.* **127**, 167201 (2021).
- [92] G. Manzanares, T. Champel, D. M. Basko, and P. Nataf, *Phys. Rev. B* **105**, 245304 (2022).
- [93] T. Byrnes, N. Y. Kim, and Y. Yamamoto, *Nature Phys.* **10**, 803 (2014).
- [94] K. Baumann, C. Guerlin, F. Brennecke, and T. Esslinger, *Nature* **464**, 1301 (2010).
- [95] F. Mivehvar, F. Piazza, T. Donner, and H. Ritsch, *Advances in Physics* **70**, 1 (2021).
- [96] F. Dimer, B. Estienne, A. S. Parkins, and H. J. Carmichael, *Phys. Rev. A* **75**, 013804 (2007).
- [97] P. Domokos and H. Ritsch, *Phys. Rev. Lett.* **89**, 253003 (2002).
- [98] G. Mazza and A. Georges, *Phys. Rev. Lett.* **122**, 017401 (2019).